ENGINYERIA ELECTRÒNICA ELÈCTRICA I AUTOMÀTICA

UNIVERSITAT ROVIRA I VIRGILI

Graduate Students Meeting on Electronics Engineering

Tarragona, Spain. June 27-28, 2013

BOOK OF ABSTRACTS

ENGINYERIA ELECTRÒNICA ELÈCTRICA I AUTOMÀTICA
UNIVERSITAT ROVIRA I VIRGILI
Graduate Students Meeting on Electronics Engineering
Tarragona, Spain. June 27-28, 2013

Programme

PROGRAMME

Thursday June 27th

9:30 Opening Session

9:45 Invited Conference

Modeling Amorphous Metal Oxide Semiconductor Thin Film Transistors
Dra. Magali Estrada del Cueto. *Sección de Electrónica del Estado Sólido, Departamento de Ingeniería Eléctrica, CINVESTAV-IPN.*

10:45 Coffee Break

11:15 Invited Conference

Nanomaterials for Medical Diagnosis
Dr. Emilio Palomares. *ICIQ - Institut Català d'Investigació Química. And ICREA - Institució Catalana de Recerca i Estudis Avançats.*

12:15 Students Oral Session 1

- ***Fabrication and Electrical Characterization of Nanostructured Organic Solar Cells with Large-Area Interdigitated Array***

V.S. Balderrama, P. Granero, G Macias, P. Formentin, J. Pallarés, J. Ferré-Borrull, and L.F. Marsal

- ***Differential functionalization of the internal and external surfaces of hollow SiO2 micropillars.***

M. Alba, E. Romano, P. Formentín, J. Ferré-Borrull, J. Pallarès, L.F. Marsal

- ***Compact Physical Models for Gate Charge and Gate Capacitances of AlGaN/GaN HEMTs.***

F.M. Yigletu1, S. Khandelwal, T.A. Fjeldly and B.Iñiguez

13:15 Lunch

14:00 Poster Session

15:00 Invited Conference

Signals in Bioinformatics
Dr. Alexandre Perera Lluna. *Centro de Investigación en Ingeniería Biomédica UPC, Barcelona.*

16:00 Invited Conference

Surface-Enhanced RAMAN Scattering (SERS) Spectroscopy: A Paradigmatic Example of Nanoscience
Dr. Luca Guerrini. *CTQC - Centre Tecnològic de la Química de Catalunya and URV - Universitat Rovira i Virgili*

17:00 Coffee Break

17:30 Students Oral Session 2

- ***Aerosol Assisted Chemical Vapor Deposition of WO3 Nanoneedles using Cold Wall Reactor based on Sensor Self-heating.***

F.E. Annanouch, R. Binions, E. Llobet

- ***Functionnalization and decoration of MWCNT for resistive gas sensing application.***

P. Clément, E. Llobet, H. Debéda

- ***Modeling the Junctionless DG MOSFETs.***

Thomas Holtij, Michael Graef, Franziska Hain, Alexander Kloes, Benjamín Iñíguez

PROGRAMME

Friday June 28th

9:30 Invited Conference

An overview of Smart Grids: Technologies, Applications and Research Challenges.
Dr. Mohamed Essaaidi. *Mohamed 5 Souissi University, Rabat, Morocco.*

10:30 Coffee Break

11:30 Invited Conference

New generation of sliding mode algorithms: application to control, observation and identification problems in fuel cells.
Dr. Cristian Kunusch. *Institut de Robòtica i Informàtica Industrial (CSIC-UPC), Barcelona.*

12:30 Students Oral Session 3

- ***Synthesis of a Sliding Loss-Free Resistor based on a Semi-bridgeless Boost Rectifier for Power Factor Correction Applications.***

A. Marcos Pastor, A. Cid Pastor, E. Vidal Idiarte, L. Martínez Salamero.

- ***A Transformer-Less Dual Stage Grid Connected Photovoltaic Micro-Inverter.***

O. Lopez-Santos, L. Martinez-Salamero, G. Garcia, H. Valderrama-Blavi

- ***Using the Characteristic Hessian in Extremum Seeking Control for PV Generator.***

H. Zazo, R. Leyva.

13:15 Closing Session

13:30 Lunch

ENGINYERIA ELECTRÒNICA ELÈCTRICA I AUTOMÀTICA

UNIVERSITAT ROVIRA I VIRGILI

Graduate Students Meeting on Electronics Engineering

Tarragona, Spain. June 27-28, 2013

Invited Sessions

MODELING AMORPHOUS METAL OXIDE SEMICONDUCTOR THIN FILM TRANSISTORS

M. Estrada[1], A. Cerdeira[1], A. Castro-Carranza[2], M. Cheralathan[2], P. Barquinha[3], E. Fortunato[3], S. Mijalkovic[4], B. Iñiguez[2]

[1]Sección de Electrónica del Estado Solido . Departamento de Ingeniería Eléctrica, CINVESTAV, Av. IPN No. 2508, 07360, D.F., México
[2]Departament dÉnginyeria Electronica Electrica i Automatica, Universitat Rovira i Virgili,
Avda. Paisos Catalans 26, 43007, Tarragona, España
[3]CENIMAT-I3N, FCT-Universidade Nova de Lisboa, Caparica, Portugal
[4]Silvaco Europe Ltd, St ives, Cambridshire, UK

Amorphous Oxide Semiconductor Thin-Film Transistors, AOS-TFTs, are receiving much attention because of their characteristics, which are suitable to serve as drivers in Active Matrix Organic Light Emitting Diodes AM-OLEDs. Among advantages of AOS-TFTs are: high mobility, high on/off ratio, low processing temperatures and possibility of fabrication on large areas.

Among metal oxides, TFTs made with amorphous In-Ga-Zn-O (a-GIZO) and Hf-In-Zn-O (HIZO) have provided good characteristics, although problems related to the stability with bias, temperature and illumination still need to be understood and optimized. These instabilities include the parallel displacement of the transfer curves observed in all TFTs, (V_T shift), as well as a hump or deformation which can appear in the subthreshold region of the transfer curves, after illumination and DC stress.

For the application of these devices, optimization of the fabrication process, as well as development of compact models to be introduced in circuit simulators are required.

In this work we present a physically based compact model for AOS TFTs, which has been validated for GIZO and HIZO devices. The model can represent also the gate bias-stress effect observed in some of these devices. It is based on the Unified Model and Extraction Method (UMEM), which has been adapted to different types of TFTs. It has been implemented in Verilog-A code and included as MOTFT model in Electronic Design Automation tools (EDA).

Nanomaterials for Medical Diagnosis

Emilio Palomares
ICIQ - Institut Català d'Investigació Química
ICREA - Institució Catalana de Recerca i Estudis Avançats.

Abstract:

We present here in two colour encoded silica nanospheres (2nanoSi) for the fluorescence ratiometric determination of trypsin.

2nanoSi proved to be a fast, easy-to-use, non-invasive and very sensitive system, allowing trypsin detection below 25 ppb. Moreover, the 2nanoSi assay allows the determination of a wide concentration range of trypsin enzyme (25-350 mg/L). As trypsin is directly related to the development of cystic fibrosis (CF), the nanospheres have been used to determine different human phenotypes according to the fluorescence ratiometric determination of different trypsin concentrations in human patients, i.e. normal (160-340 mg/L), CF homozygotic (0-90 mg/L), and CF heterozygotic (91-349 mg/L), respectively.

Biography:

He studied Biology (Biochemical speciality) in the *Universitat de València* (1997). After graduating he joined the group of Prof. Hermenegildo García at the *Universitat Politécnica de València* where he got his Doctoral Thesis (2001).

In 2001 he made a postdoctoral stay with a Marie Curie Fellowship at the Centre for Electronic Materials and Devices of the Imperial College in London (UK). There he began his work with molecular and biomolecular devices to obtain renewable energies, under the direction of Prof. James R. Durrant.

In 2004 Emilio got a *Ramón y Cajal* Fellowship in the *Universitat de València* joining the *Institut de Ciència Molecular* of this University.

In April 2006 he took a position in ICIQ, where he currently leads a research group which is focusing research in investigation on optoelectronic properties of molecular and biomolecular devices (photovoltaic devices and optical sensors). In November 2007 he was appointed ICREA (Catalan Institution of Research and Advanced Studies) Professor.

Emilio Palomares has several awards including the Young Chemist Research Award of the Real Sociedad Española de Química and has published until 2007 more than 65 peer-rewied papers.

He currently cooperates with several national and international photovoltaic companies and he is the Project Coordinator of several European Projects (FP6 and FP7), including the project *Control of the Electronic Properties in Hybrid-Quantum Dot/Polymer-Materials for Energy Production(POLYDOT*), for a period of 5 years and founded by the *European Research Council Starting Grant*.

An overview of Smart Grid: Technologies, Applications and Research Challenges

Mohamed Essaaidi
Mohamed 5 Souissi University, Rabat, Morocco

Abstract:
The smart grid is a major power grid transformation based on a constantly evolving infrastructure of information technology and power-industry practices for improved management of electricity generation, transmission, and distribution. There are many benEfits and advantages associated with smart grid compared to the conventional electric grid, namely, better reliability, efficiency, and security.
In this talk, different issues related with smart grid such as the underlying technologies, standards, architectures and applications will be discussed in detail. Special emphasis will be put on emerging trends in Smart Grid and on different research challenges and business opportunities offered by this emerging technology.

Biography:

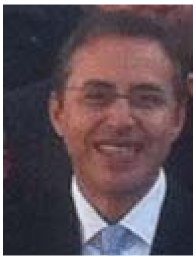

Prof. Dr. and IEEE Senior Member, is the current Director of National College of IT (ENSIAS) of Mohammed 5th Souissi University, Rabat, Morocco and he was a Professor of Electrical & Computer Engineering at Abdelmalek Essaadi University, Morocco from 1993 till 2011. He is the founder and Chairman of the IEEE Morocco Section, founder of IEEE Computer & Communication Societies Joint Morocco Chapter, Founder and Chair of IEEE Antennas and Propagation Society and Microwave Theory and Techniques Society Morocco Joint Chapter and founder of IEEE Education Society Morocco Chapter.. He has authored and co-authored 5 books and more than 146 papers in international refereed journals and conferences. He has been the Editor-in-Chief of International Journal on Information and Communication Technologies, Serial Publications, India since 2007. He is also an active member of the editorial boards of several IEEE and other international journals. He was also a member of the IEEE WiMmax 802.16 Sponsor Ballot Pool of IEEE Standard.

New Generation of Sliding Mode Algorithms: Application to Control, Observation and Identification Problems in Fuel Cells

Cristian Kunush
Institut de Robòtica i Informàtica Industrial (CSIC-UPC), Barcelona

Abstract:

In this talk, general notions of second order sliding modes and its direct use in control, observation and identification problems will be introduced. Also adaptive extremum seeking algorithms based on sliding mode observer will be presented. The applications and presented results will be focused on PEM fuel cell based systems.

Biography:

Dr. Kunusch (05/05/1979) was graduated in 2003 in Electronic Engineering from National University of La Plata (UNLP), Argentina. Since 2003 he has been a member of the Laboratory of Industrial Electronics, Control and Instrumentation (LEICI), at Electrical Engineering Department, UNLP. In 2003 he was appointed as Graduate Teaching Assistant of Automatic Control, Electrical Engineering Department, UNLP. In 2006 he was appointed as Lecturer of Dynamic Systems Identification, Universidad Autónoma de Entre Ríos, Argentina. From 2003 on, he focused his research on variable structure control and its application to fuel cells based systems. During 2003-2010 he obtained consecutive research fellowships to get his MSc and PhD degrees. During 2006-2008 he made five research stays at the Institut de Robòtica i Informàtica Industrial (CSIC-UPC) in Barcelona, funded by international projects supported by the Spanish Agency of International Cooperation (AECID), UNLP and UPC. From the core of his PhD activities, he published 6 papers as first author in SCI Journals and one book (published in 2012 by Springer UK). He currently holds a position of Assistance Researcher at the Institut de Robòtica I Informàtica Industrial (CSIC-UPC), runs a Marie Curie Career Integration Grant and is part of the research staff of a project focused on multi-scale modeling of PEM fuel cells, both funded by the Seventh Framework Programme of the European Community.

Signals in Bioinformatics

Alexandre Perera i Lluna
Centro de Investigación en Ingeniería Biomédica UPC, Barcelona

Abstract:

This talk is structured in two parts. First, a brief introduction of the involved biology is presented, jointly with comments on gene transcription, genetic variability and the hunt for the unexplained heritability of complex diseases. In a second part, we will explain some of the contributions we have proposed in the processing of DNA sequences, which were inspired from the signal processing techniques common in other fields. We will show how event detection algorithms and information theory have proved to be extremely interesting theories when applied to DNA sequence processing.

Biography:

Alexandre Perera i Lluna es licenciado en física (1996), ingeniero eléctrico (2001) y doctor en física (2003) por la Universidad de Barcelona. Durante los años 2003-2005 realizó una estancia en la Texas A&M University como Investigador Postdoctoral, y actualmente es investigador "Ramón y Cajal" en el Centro de Investigación en Ingeniería Biomédica (CREB) en la Universidad Politécnica de Cataluña (Barcelona).
Su principal área de investigación se centra en algortimos de reconocimiento de patrones aplicados a varias áreas incluyendo señales de sensores químicos y bioinformática.

Surface-Enhanced Raman Scattering (SERS) Spectroscopy: A Paradigmatic Example Of Nanoscience

Luca Guerrini
Centre Tecnològic de la Química de Catalunya – CTQC
Universitat Rovira i Virgili - URV

Abstract:

Surface-enhanced Raman scattering (SERS) consists in the dramatic amplification of the Raman signals originated from molecules located in close proximity of nanostructured metal surfaces. SERS was discovered in 1974 and correctly interpreted in 1977, and since then the field has grown enormously in breadth, depth, and understanding. In particular, SERS benefited from the relatively recent improvements in Raman spectrometers and the spectacular advances in nanofabrication to become nowadays one of the hottest topics in nanoscience. One of the major characteristics of SERS is its interdisciplinary nature. SERS exists at the boundaries shared among physics, chemistry, colloid science, plasmonics, technology, engineering, and biology. Here, we simply outline the main theoretical concepts behind SERS, and present a brief overlook of the advanced aspects of such fascinating technique both in terms of the design of novel plasmonic nanostructures for SERS and the potential sensing applications to real problems (in particular those carried out by our group, “Zeptonic”).

Biography:

Luca Guerrini achieved his Master’s degree cum laude in Industrial Chemistry from University of Bologna, Italy.

In 2009, he received his PhD from Universidad Autónoma de Madrid, Spain, for his work on the engineering of SERS-based nanosensors for trace detection of persistent organic pollutants.

He moved in 2010 to the Department of Pure & Applied Chemistry, University of Strathclyde, Glasgow (UK) as an invited postdoctoral researcher under the supervision of Prof. Duncan Graham. In the two years in Glasgow, his research mainly focused in the design of DNA-functionalized metal nanoparticle conjugates for SERS bio-applications.

In late 2012, he joined the Prof. Alvarez-Puebla’s group where he is currently employed as a postdoctoral fellow. He was recently awarded with a Marie Curie Intra-European Fellowship.

ENGINYERIA ELECTRÒNICA ELÈCTRICA I AUTOMÀTICA
UNIVERSITAT ROVIRA I VIRGILI
Graduate Students Meeting on Electronics Engineering
Tarragona, Spain. June 27-28, 2013

Regular Sessions

Differential functionalization of the internal and external surfaces of hollow SiO_2 micropillars

M. Alba, E. Romano, P. Formentín, J. Ferré-Borrull, J. Pallarès, L.F. Marsal

Departament d'Enginyeria Electrònica, Elèctrica i Automàtica, Universitat Rovira i Virgili
Avda Països Catalans 26, 43007 Tarragona (Spain); E-mail: lluis.marsal@urv.cat; Tel: (34) 977 55 96 25

Abstract

The internal and external surfaces of hollow silicon dioxide micropillars were differently functionalized. Two independent grafting procedures, involving silanizations and protein immobilization, were used to modify the chemistry of the internal and external surfaces. Infrared spectroscopy confirmed the occurrence of each chemical step. By labeling with two different dyes, we proved the viability of the observation by confocal microscopy. Thus, the successful dual-side functionalization with no cross-over between the two sides was demonstrated. This strategy opens a new route to monitor the interaction between biological species externally attached and active bio-agents host in the internal core.

1. Introduction

Arrays of micropillars are a suitable interface to study the micro-sized world. These arrays can mimic the 3D-architectured surroundings that cells experiment in their natural environment, constituted by a variety of nm-to-micron-sized features. The interaction between the array of micropillars and the cell morphology eventually determines the cell response [1]. The spatial organization of micropillars has attracted great attention, to the detriment of surface functionalization, even though this can be crucial for the cell reaction. For instance, functionalization could decrease the stiffness and improve cell adhesion [2].

Hollow silicon dioxide (SiO_2) micropillars can be obtained from macroporous silicon produced by electrochemical etching. Their intrinsic core/shell structure comprises a double-side surface which, differentially functionalized, can be suitable for the interaction between biological species and active agents. Thus, bio-species can be grasped on the external side, whilst the internal surface may carry some bio-agents.

Here, we present dual-side functionalized micropillars as a novel device suitable for bioapplications. The internal and external surfaces were differentially modifier following two independent functionalization pathways. The solid SiO_2 wall functions as a barrier avoiding cross-contamination and provides an appropriate surface for chemical modification. Infrared spectroscopy (FT-IR) was used to confirm the occurrence of each chemical step. Confocal microscopy gave further evidence of the derivatization and was demonstrated to be a suitable technique to observe the differential functionalization.

2. Experimental

Macroporous silicon was fabricated by electrochemical etching [3]. The starting material was a p-type silicon wafer of resistivity 40-60 Ω·cm. In order to obtain periodically arranged pores, we applied the lithographic and indentation processes detailed elsewhere [4] with a 4 µm lattice constant. Regular macropores were grown perpendicular to the surface by etching in a solution 1:10 (v:v) of hydrofluoric acid (40%) in N,N dimethylformamide under galvanostatic conditions (5 mA/cm^2). Given our experimental conditions, the pore growth rate was 0.8 $\mu m \cdot min^{-1}$. Then, an approximately 250 nm thick SiO_2 wall was grown by thermal oxidation under air at 1000 ºC for 1.5 h. The backside oxide layer was removed by buffered hydrofluoric acid (BHF) etching.

After that, the internal surface functionalization was carried out. The sample was immersed in a 5 mM solution of (3-mercaptopropyl) trimethoxysilane (MPTMS, Gelest) in anhydrous toluene for 3 h at 75 ºC. Then, the MPTMS was fluorescent-labelled using a 100 µg/mL tetramethyl rhodamine-5-maleimide solution. Following the first silanization, the micropillars were released by etching the backside of the Si wafer in 25 % TMAH at 85 ºC. As outcome, the oxidized pore tips appear protruding out of the wafer backside. Once the external micropillar was uncovered, the sample was placed in a one-side Teflon cell and the external surface exposed to a 5 mM solution of (3-aminopropyl) triethoxysilane (APTES, Gelest) in anhydrous toluene. Gluteraldehyde (GTA) reaction was performed in a 10 % (v/v) solution in anhydrous ethanol (Electron Microscope Sciences). Finally, the samples were incubated in fluorescein isothiocyanate-labelled bovine serum albumin (FITC-BSA, Sigma-Aldrich) 100 $\mu g \cdot mL^{-1}$.

3. Results and discussion

The regular arrangement given by the lithographic pattern is preserved throughout the pore formation and the micropillar releasing. The released SiO_2 micropillars maintain the shape of the initial pore formed on the Si substrate, i.e. rounded-squared section and almost hemispherical tips (image not shown).

Silanizations and GTA grafting were studied by infrared spectroscopy on mild oxidated nanoporous silicon samples. The –SH terminal group from the MPTMS is easily recognizable by the sulphur-hydrogen stretching at 2580 cm^{-1} (see Fig. 1, top). In the case of the APTES silanization, NH_2 characteristic stretching vibrations were apparent in the spectrum at 3310 and 3375 cm^{-1}, assigned to asymmetric and antisymmetric stretching, respectively (Fig. 1, bottom). Further functionalization with GTA was identified by the extinction of νNH_2 bands and the appearance of a quite strong peak at 1725 cm^{-1}, assigned to the stretching mode of the carbonyl (Fig. 1, bottom).

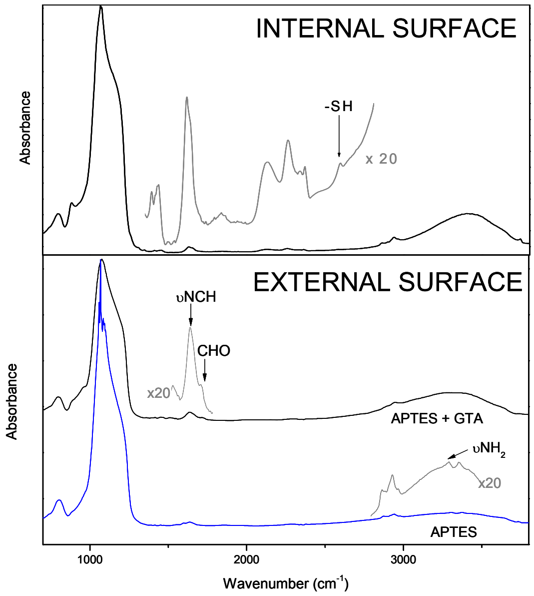

Fig 1. FT-IR spectra of a porous Si sample at selected steps. (A) MPTMS functionalization; and (B) APTES and GTA functionalization, corresponding the internal and external surface of a SiO_2 micropillar, respectively.

The subsequent attachment of a fluorescent dye makes it possible the investigation by confocal microscopy. Fig. 2A evidenced the rhodamine attachment as well as the viability of observing the internal wall, when exciting with a 543 nm laser and using a 590 ± 30 nm. Similarly, a sample was observed after the incubation in FITC-BSA with a 488 nm laser and a bandpass filter of 515 ± 15 nm. Fig. 2B shows green emission deriving from the FITC-labeled protein immobilized on the external surface. The colored rings appear in a distribution equivalent to that of the micropillars. After performing the differential double-side functionalization, the micropillars were scratched and observed through both green and red channels under the simultaneous excitation of 488 and 543 lasers (Fig. 2C). The fluorescent image revealed a range of orange-ish to green-ish areas which correspondingly match the rhodamine inside and the FITC-BSA outside the micropillar.

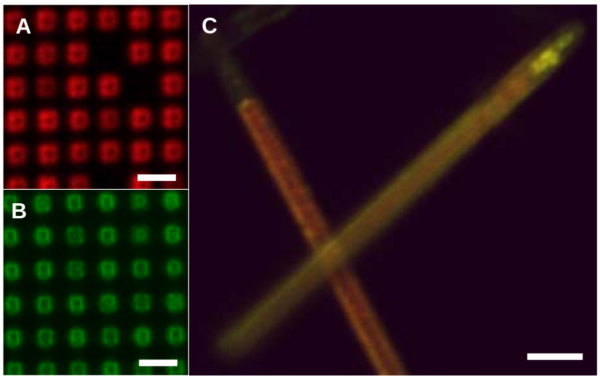

Fig. 2. Confocal microscopy images of hollow SiO_2 micropillars. (A) Rhodamine emission from the internal surface; (B) FITC-BSA deriving from the external surface; (C) dual-side functionalized micropillars. Scale bar 5 μm.

4. Conclusions

The differential functionalization of the internal and external surface of hollow dioxide micropillars has been demonstrated. The method makes it possible the incorporation of two different chemical functionalities, labelled with different fluorescent dyes. The confocal microscopy proved the dual-side functionalization and the feasibility of the observation by confocal microscopy. We believe SiO_2 hollow micropillar arrays are a tool of great versatility and potential in biologic applications.

Acknowledgements

This work was supported by the Spanish Ministry of Science and Innovation (MICINN) under grant no. TEC2012-34397 and AGAUR 2009 SGR 549.

References

[1] W.-T. Su, Y.-F. Liao, C.-Y. Lin, and L.-T. Li, *Journal of Biomedical Materials Research Part A,* vol. 93A, pp. 1463-1469, 2010.

[2] L. E. Dickinson, D. R. Rand, J. Tsao, W. Eberle, and S. Gerecht, *Journal of Biomedical Materials Research Part A,* vol. 100A, pp. 1457-1466, 2012.

[3] A. F. Vyatkin, in *Micro- and Nanoelectronics 2003*. vol. 5401, K. A. Valiev and A. A. Orlikovsky, Eds., ed, 2004, pp. 187-191.

[4] T. Trifonov, A. Rodriguez, F. Servera, L. F. Marsal, J. Pallares, and R. Alcubilla, *Status Solidi a-Applications and Materials Science,* vol. 202, pp. 1634-1638, Jun 2005.

Fabrication and Electrical Characterization of Nanostructured Organic Solar Cells with Large-Area Interdigitated Array

V.S. Balderrama, P. Granero, G Macias, P. Formentin, J. Pallarés, J. Ferré-Borrull, and L.F. Marsal*

Departament d'Enginyeria Electrònica, Elèctrica i Automàtica, Universitat Rovira i Virgili, Avda. Països Catalans 26, 43007 Tarragona, Spain.
*Corresponding author: e-mail: lluis.marsal@urv.cat, Phone. +34 977 559 625, Fax: +34 977 559 605

Abstract

The method by soft nanoimprinting nanoporous anodic alumina (NAA) templates is used to manufacture the nanostructured organic solar cells (NS–OSC). The device was manufactured with the architecture ITO-120 nm / PEDOT:PSS- 40 nm / P3HT-Nanopillars / $PC_{70}BM$-35 nm / Ca-25 nm / Ag-100 nm. The structure was compared with a planar bilayer organic solar cell (BL-OSC) made under the same materials and conditions. Electrical characterization was done and power conversion efficiency was 2-fold more than that BL–OSC. The relative increase of fill factor in NS–OSC was 52% more than that BL–OSC and was related with the decrease of the resistance series into of the network pathways of the polymer material formed.

1. Introduction

Recently, the advances of the NS–OSC fabricated from conducting polymers have attracted much interest [1-3]. However, the development of nanostructure morphology for photovoltaic applications is one of many points to obtain a good performance. In this work, we manufacture NS–OSC with large area interdigitated array in combination with the use of NAA templates. NS–OSC devices were electrically characterized and compared with BL–OSC.

2. Experimental Results

Fig. 1 shows the typical photovoltage nanostructure that was made in this work. To get P3HT-nanopillar, first it is necessary to fabricate the NAA template and it was made in two steps anodization as it is reported in ref. [4]. The first anodization was made in aqueous solution of oxalic acid ($H_2Cr_2O_7$) (0.3 M) by 21 hours at 5 ^{o}C and applying the voltage directly of 40 V. The second step of the anodization process was conducted under the same anodization conditions that the first step but for 80 s. The NAAT were modified by dimethylpolysiloxane (DPMS) to reduce the surface energy of the templates. To obtain the P3HT nanopillars, first the solution was prepared in chlorobenzene (C_6H_5Cl) and after it, it was spin coated onto the previous prepared structure of glass/ITO/PEDOT:PSS under N_2 atmosphere. Afterwards, the nanoimprinting was done with the NAA template at 2 MPa at a temperature of 120 ºC on the structure previous made. $PC_{70}BM$ solution was prepared in anisole ($CH_3OC_6H_5$) and deposited on glass/ITO/PEDOT:PSS/P3HT nanopillars by spin coating. Metals were evaporated through a shadow mask leading to devices with an active area of 0.09 cm^2. Ca and Ag were deposited at a rate of 0.15 Å s^{-1} and 0.5–0.8 Å s^{-1}, respectively. At the same time, planar bilayer organic solar cells were manufactured to compare against the NS–OSC made with nanopillars. The current density–voltage (*J–V*) characteristics of the devices were measured with a Keithley 2400 source measurement unit in combination with a solar simulator (Abet Technologies model 11000 class type A). The appropriate filters were utilized to faithfully simulate the AM 1.5G spectrum.

Fig. 2 is shown a) tilt and b) top view images by environmental scanning electron microscopy (ESEM) of NAA template. Diameter and height of pore were 60 nm and 80 nm respectively. P3HT nanopillars were obtained after the soft nanoimprinted by NAA templates and is shown in Fig. 3a and 3b the tilt and top view images by ESEM, respectively. A suitable average of height pillar (H_{pillar}), pillar diameter (ϕ_{pillar}), interpillar distance (S_{pillar}) and residual layer (*R-L*) were 80 nm, 60 nm, 100 nm and 40 nm, respectively. The relative increase in the donor-acceptor interface area was calculated as in [3] and this leads a increase of 2.5 times. The BL–OSC manufactured contain 40 nm of $PC_{70}BM$ on 130 nm P3HT. All devices were measured at 1 sun. The *J–V* curves under light of NP–OSC and BL–OSC devices are shown in Figure 4. The parameters of the organic solar cells were listed in Table

1. NS–OSC made with P3HT nanopillars show an improved in all the performance parameters for power conversion efficiency (*PCE*), open circuit voltage (V_{OC}), short circuit current (J_{SC}) and fill factor (FF) of 100%, 28%, 6% and 52%, respectively. The explanation of these improvements is because the well-controlled interdigitated heterojunction morphology allows a more efficient exciton dissociation and charge transport in the device. The increase of FF could be explained due to nanoimprint induced molecular ordering of the P3HT as is reported in [3, 5] and the decrease of series resistance. However, more studies of analysis is required to understand the favorable changes in performance parameters of the cells.

3. Conclusions

Organic solar cells with an interpenetrating donor-acceptor network based on P3HT and $PC_{70}BM$ have been realized. The NS-OSC were compared with BL-OSC. We succeeded in obtaining a 2.5 fold enhancement of the interfacial area between donor and acceptor material in nanoimprinted devices as compared to planar OSC. The PCE in NS-OSC was a 100% higher than that BL-OSC.

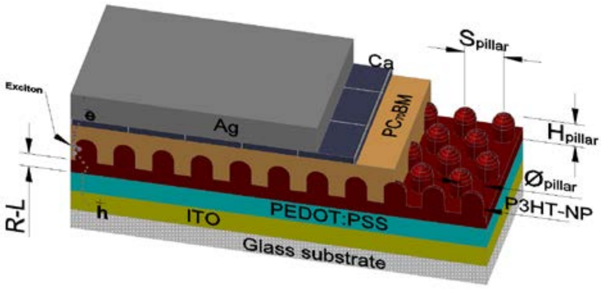

Fig.1. The image shows the typical structure of NS–OSC with all the layers (Glass / ITO / PEDOT:PSS / P3HT nanopillars / $PC_{70}BM$ / Ca / Ag and its geometric characteristics that define a P3HT nanopillar. ϕ_{pillar} is pillar diameter, S_{pillar} is interpillar distance, H_{pillar} is height and *R-L* is residual layer.

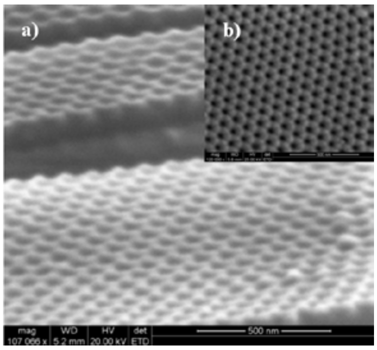

Fig.2. ESEM images are shown in a) tilt and b) top views of NAA template used to fabricate the P3HT–NP.

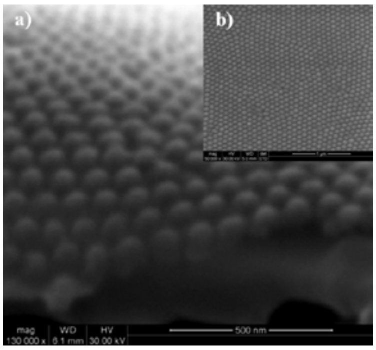

Fig.3. a) Tilt and b) top view of P3HT–NP images obtained by ESEM.

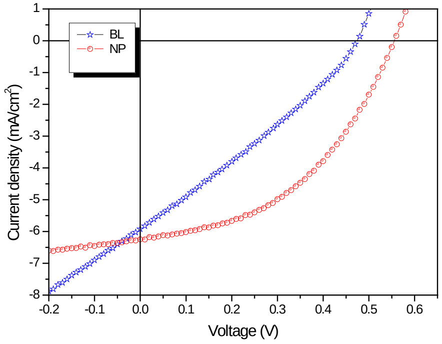

Fig.4. *J–V* curves of NP–OSC and BL–OSC under illumination at 1 sun (AM 1.5G spectrum).

Ref	P3HT / $PC_{70}BM$	V_{OC} [mV]	J_{SC} [mA/cm^2]	FF [%]	PCE [%]	R_S [Ω-cm^2]	R_{SH} [Ω-cm^2]
A	BL	439	5.92	29.5	0.76	13.05	3.0×10^5
B	NP	560	6.24	44.7	1.56	7.34	1.1×10^6

Table1. Performance parameters of NP-OSC and BL–OSC.

Acknowledgements

This work was supported by the Spanish Ministry of Economy and competitiveness (MINECO) under grant number, TEC2012-34397 and by Catalan authority under project 2009 SGR 549.

References

[1]P. Granero, “Two-dimensional finite-element modelling of periodical interdigitated full organic solar cells", *J. Appl. Phys. 113*, pp. 043107, 2013.

[2]Y. Yang, “Nanoimprinted polymer solar cell”, *ACS Nano 6 No. 4*, pp. 2877, 2012.

[3] W. Wiedemann, “Nanostructured interfaces in polymer solar cells”, *Appl. Phys. Lett. 96*, pp. 263109, 2010.

[4]A. Santos, “Fabrication and characterization of high-density arrays of P3HT nanopillars on ITO/glass substrates”, *Solar Energy Materials & Solar Cells 94*, pp. 1247-1253, 2010.

[5]X. He., “Formation of well-ordered heterojunctions in polymer:PCBM photovoltaic devices", *Adv. Funct. Mater. 21*, pp. 139, 2011.

Two-dimensional Physics-based Modeling of Band-to-Band Tunneling in Tunnel-FETs

Michael Graef[1,2,✠], Thomas Holtij[1,2], Franziska Hain[1,2], Alexander Kloes[1], and Benjamín Iñíguez[2]

[1]Competence Center for Nanotechnology and Photonics, Technische Hochschule Mittelhessen, Giessen, Germany
[2]DEEEA, Universitat Rovira i Virgili, Tarragona, Spain
✠michael.graef@ei.thm.de

***Abstract*—In the last few years the Tunnel-FET has become one of the promising devices to be the successor of the MOSFET due to its CMOS compatibility and steep subthreshold slopes (S) below 60 $\frac{mV}{dec}$. In this paper a 2D physics-based analytical model for Tunnel-FETs is introduced. It predicts a 2D band-to-band tunneling probability calculation through Wentzel-Kramers-Brillouin approximation (WKB) based on a 2D solution of electrostatics with respect to the device structure and carrier distributions in the device. These results are embedded in a model for the device current.**

***Index Terms*—analytical modeling, band-to-band tunneling, Double-Gate (DG) Tunnel-FET.**

I. INTRODUCTION

In the last few years the downscaling of metal-oxide-semiconductor field-effect transistors (MOSFETs) have caused problems due to the increasing short-channel effects (SCEs) in the sub 22 nm technology. This technology has its physical limits due to the drift-diffusion current transport mechanism of a minimal subthreshold-slope of 60 $\frac{mV}{dec}$. The Tunnel-Field-Effect-Transistor (TFET) is a promising device to fall below this physical limit because of its band-to-band tunneling carrier transport mechanism at the channel junctions [1].

Physics-based analytical models are needed to simulate complex circuits and hence to predict the electric behavior special to TFETs. In the following sections the device physics is explained. The current transfer characteristics of the model in comparison to TCAD [2] simulation data is shown.

II. TUNNEL-FET OVERVIEW

The model predicts the behaviour of a Double-Gate n-Tunnel-FET with the device geometry shown in Fig. 1. The source area consists of a highly p-doped Si area, the drain area is highly n-doped Si and for the channel region intrinsic Si.

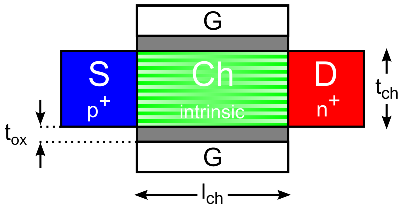

Fig. 1. Geometry of a DG TFET showing its doping profile, structural parameters and channel slices for current calculation.

III. MODELING APPROACH

The model consists of a 2D potential solution and a closed form approach for the 2D electrical field. With these results an expression for the 2D tunneling probability was developed using the WKB approach followed by the calculation of the device current with the Fermi distributions for source and drain relation. So far the model does not include trap-assisted tunneling (TAT), bandgap narrowing and junction resistances yet.

A. Tunneling Probability

For the calculation of the tunneling probability we use a two-dimensional approach of the WKB approximation [3]. Therefore, we divide the channel area in horizontal slices (see Fig. 1). For every slice the tunneling probability is calculated to every point in the channel region where tunneling can happen (Fig. 2).

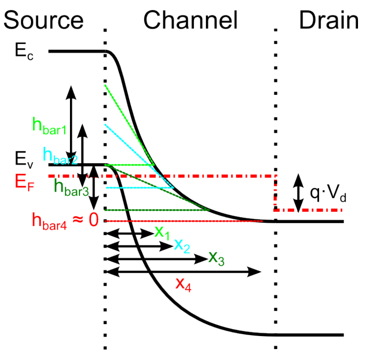

Fig. 2. Schematic band structure for a DG n-Tunnel-FET with 2D approach for the tunneling probability. The triangles are used for the WKB method.

Therefore, we use the tangent of the band structure at one point in the channel region to define a triangle including that point, the distance from the channel junction (x_n) and the barrier height ($h_{bar,n}$) which is needed for the WKB approximation, which assumes a triangular shape of the barrier. Then we can calculate the tunneling probability from the junction to the considered point in the channel.

$$T_{tun}(x,y) = \exp\left(-\frac{4}{3} \cdot \frac{\sqrt{2 \cdot m \cdot m_0} \cdot (|E(x,y)| \cdot x)^{\frac{3}{2}}}{q \cdot \hbar \cdot |E(x,y)|}\right), \quad (1)$$

with the electrical field $E(x)$ and the carrier effective mass m. The expression $|E(x,y)| \cdot x$ equals the barrier height h_{bar}.

B. Tunneling Current

With the given probabilities for electrons at the valence band in the source area f_{ms}, the probability of holes at the conduction band in the channel area f_{md} and the tunneling probability T_{tun} the band-to-band tunneling current can be calculated for all tunneling paths [4]

$$J_t = \frac{\mu_n \cdot N_c \cdot q^2}{k \cdot T} \int_{0}^{t_{ch}} \int_{x_{int}}^{l_{ch}} T_{tun} \cdot (f_{ms} - f_{md}) \cdot |E|^2 dx \cdot dy \quad (2)$$

with the charge carrier mobility μ_n, the effective density of states in the conduction band N_c and the electrical field E.

IV. RESULTS

To validate the model a comparison of the current transfer characteristics for different device geometry variations has been performed. The model results are compared against TCAD simulation data. Table I shows the parameter setting for the TCAD simulator. We used a nonlocal band-to-band tunneling model for the simulation.

TABLE I
PARAMETER SETTINGS OF THE SIMULATED TCAD SENTAURUS DEVICE.

l_{ch}	28	[nm]	channel length
t_{ch}	10 / 12 / 15	[nm]	channel thickness
t_{ox}	1 / 1.2 / 1.5	[nm]	oxide thickness
N_s	10^{20}	[cm^{-3}]	source doping
N_d	10^{20}	[cm^{-3}]	drain doping

A. Current

With the given parameter set the variation of the channel thickness t_{ch} results in the following transfer characteristics (Fig. 3), which are fitted for a channel of 12 nm.

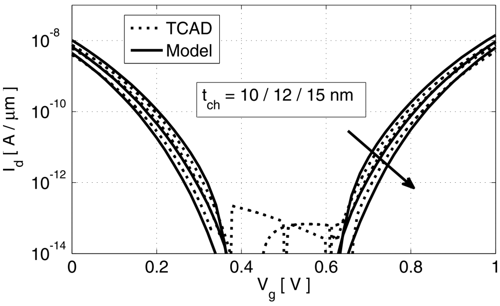

Fig. 3. Current transfer characteristics of an n-type DG-Tunnel-FET with V_d = 1 V, l_{ch} = 28 nm and t_{ox} = 1 nm for various t_{ch} = 10 / 12 / 15 nm.

Then this thickness has been varied while keeping all other model parameters constant. The results stay in good agreement with the TCAD simulation data and the model predicts the physical effects that take place in the Tunnel-FET. For a decreasing channel thickness the subthreshold slope decreases and the current increases due to the improved electrostatic control on the channel region from the gate electrodes. It follows a comparison of the current transfer characteristics for different gate oxide thicknesses t_{ox} (see Fig. 4).

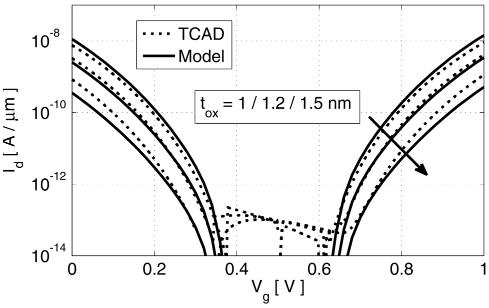

Fig. 4. Current transfer characteristics of an n-type DG-Tunnel-FET with V_d = 1 V, l_{ch} = 28 nm and t_{ch} = 10 nm for various t_{ox} = 1 / 1.2 / 1.5 nm.

For smaller oxide thicknesses the gate influence raises so the subthreshold slope and the max. current improve. The inaccuracy of the transfer characteristic for t_{ox} = 1.5 nm arises, because the model causes higher inaccuracies for an increasing oxide thickness.

V. CONCLUSION

We developed a two-dimensional analytical model for a double-gate n-Tunnel-FET including 2D solutions for the tunneling probability and the current. The model follows the physical behavior of the device and correctly predicts the simulation of a variability of oxide thickness and channel thickness. The results show that a decreasing oxide or channel thickness results in steeper slopes and higher currents due to the improved electrostatic control on the channel region by the gate electrodes.

ACKNOWLEDGMENT

This project was supported by the German Federal Ministry of Education and Research under contract No.1779X09, by German Research Foundation (DFG) under Grant KL 1042/3-1, by the European Commission under FP7 Projects ICTSTREP 257111 ("SQWIRE"), and IAPP-218255 ("COMON"), by the Spanish Ministerio de Ciencia y Tecnología under Projects TEC2011-28357-C02-01, by the PGIR/15 Grant from URV and also by the ICREA Academia Prize.

REFERENCES

[1] W. Choi, B. Park, J. Lee, and T. Liu, "Tunneling field-effect transistors (tfets) with subthreshold swing (ss) less than 60 mv/dec," *Electron Device Letters, IEEE*, vol. 28, no. 8, pp. 743–745, 2007.
[2] Synopsys, *TCAD Sentaurus*, c-2009.06 ed., Synopsys, Inc., 2009.
[3] A. Gehring, "Simulation of tunneling in semiconductor devices," Ph.D. dissertation, TU Wien, 2003.
[4] E. Gnani, S. Reggiani, A. Gnudi, and G. Baccarani, "Drain-conductance optimization in nanowire tfets," in *Solid-State Device Research Conference (ESSDERC), 2012 Proceedings of the European*. IEEE, 2012, pp. 105–108.

2-D and 3-D Finite-Element Modeling of Interdigitated Heterojunction Organic Solar Cells

P. Granero, V. S. Balderrama, J. Ferré-Borrull, J. Pallarès, and L. F. Marsal*

Nano-electronic and Photonic Systems (NePhoS), Department of Electronic, Electrical and Automatic Control
Engineering, Universitat Rovira i Virgili, Av. Països Catalans 26 43007, Tarragona, Spain
* Voice: +34 977559625, Fax: +34 977559605, E-mail address: lluis.marsal@urv.cat

1. Abstract

By means of finite-element numerical modeling, we analyze the influence of the nanostructured dissociation interface geometry on the behavior of interdigitated heterojunction organic solar cells. A systematic analysis of light absorption, exciton diffusion and carrier transport, all in the same numerical framework, is carried out to obtain their dependence on the interface geometrical parameters: pillar diameter and height, and nanostructure period. Results show that the optimal device should be a trade-off of two opposite conditions: a high proportion of electron donor to increase light absorption, and a small pillar diameter and interpillar distance to ensure an extended dissociation interface.

2. Introduction

In recent years, the interdigitated heterojunction approach has arisen as a promising solution to increase the efficiency of organic solar cells (OSC). This approach provides a proper exciton dissociation interface without sacrificing direct paths for carriers' collection [1], advantages that can lead to an increase in the efficiency of these cells [2]. However, an optimization is crucial to obtain the best results.

By means of finite-element numerical modelling [3], we investigate light absorption, exciton diffusion and free charge transport in interdigitated heterojunction full OSC for the case of poly(3-hexylthiophene) (P3HT) / 1-(3-methoxycarbonyl)-propyl-1-phenyl-(6,6)C_{61} (PCBM) devices. The Donor-Acceptor interface geometry of these cells has been varied to maximize the efficiency. This work will help to improve the cells obtained in our facilities, which are achieved via nanoporous anodic alumina templates (NAAT) [4] (Fig.1).

3. Optical and Electrical Modeling

In this study we present two models: a 2D (Fig. 2a) and a 3D one (Fig. 2b). The 2D one is a simplification of the real 3D device where the nanostructured interface is composed of alternating blocks of each organic material. In the 3D model a more complex geometry represents the P3HT nanopillars. Our model consists of a structure of indium tin oxide (ITO), Poly (3,4-ethylenedioxythiophene) poly(styrenesulfonate) (PEDOT:PSS), P3HT, PCBM and aluminium (Al). The parameters under study are α (nanopillar diameter), β (structure period (2D) or interpillar distance (3D)), γ (ratio of the nanopillar diameter to the interpillar distance ($\gamma = \alpha/\beta$)), and T (nanopillar height including the supporting base).

The finite-element approach allows computing the absorbed light as a function of the position and, with this, the exciton generation rate at every point. To obtain the current density–voltage (J–V) characteristics we have applied the exciton diffusion equation and the free charge drift-diffusion model. Results are compared with a reference planar bilayer cell.

4. Results and Discussion

Fig. 3 shows the total absorbed light power (Q_{TOTAL}) in the P3HT layer of the 2D model as a function of the nanopillars height (T) for several structure periods (β) for $\gamma = \alpha/\beta = 0.5$. In all cases the curves show a similar behaviour with two local maxima for T around 80 nm and 230 nm, and a local minimum for T close to 130 nm. The higher absorption is achieved for $\beta = 25$ and 4000 nm while the lower one is for $\beta = 250$ nm.

Fig. 4 shows the J–V curves for the 2D model for $T = 80$ nm for several β and for different $\gamma = \alpha/\beta$. We can see that the short circuit current density (J_{SC}) values are distributed over a wide range having also different trends depending on β. For $\beta = 25$ nm when γ increases J_{SC} increases in a similar proportion. On the other hand, for bigger β the increase of J_{SC} with γ is less noticeable. We obtain the same conclusions if we compare the cells efficiencies (Table 1).

A higher γ implies a higher ratio of P3HT, and therefore more absorbed light. However, due to the short exciton diffusion length of P3HT, not in all cases a supplementary amount of absorbed light will provide a proportional increase in the efficiency of the cell. Fig. 5 shows how the number of excitons able to reach the dissociation interface is reduced as the geometric features get bigger. Hence, an optimal device should be a trade-off of two opposite conditions: a high proportion of electron donor to increase light absorption, and a small pillar diameter and interpillar distance to ensure an extended dissociation interface.

Acknowledgements
This work was supported by the Spanish Ministry of Economy and Competitiveness (MINECO) under grant number TEC2012-34397 and by the Catalan Authority under project 2009SGR549.

References

[1] H. Hoppe, and N. S. Sariciftci, “Organic solar cells: An overview”, J. Mater. Res., vol. 19, pp. 1924–1945, July 2004.
[2] J. S. Kim, Y. Park, D. Y. Lee, J. H. Lee, J. H. Park, J. K. Kim, and K. Cho, “Poly(3-hexylthiophene) nanorods with aligned chain orientation for organic photovoltaics”, Adv. Funct. Mater., vol. 20, pp. 540–545, February 2010.
[3] COMSOL (COMSOL Inc.), MA, USA. Available: http://www.comsol.com
[4] A. Santos, P. Formentín, J. Pallarés, J. Ferré-Borrull, and L. F. Marsal, “Fabrication and characterization of high-density arrays of P3HT nanopillars on ITO/glass substrates”, Sol. Energy Mater. Sol. Cells, vol. 94, pp. 1247–1253, July 2010.

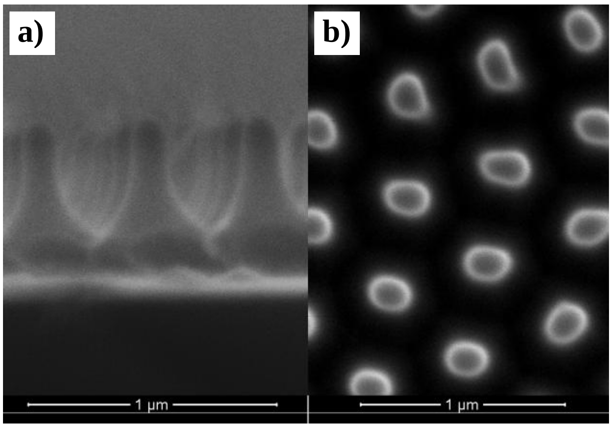

Fig.1. Environmental scanning electron microscopy images of P3HT nanopillars with the structure glass/ITO/PEDOT:PSS/P3HT made with NAAT, a) cross section and b) top view.

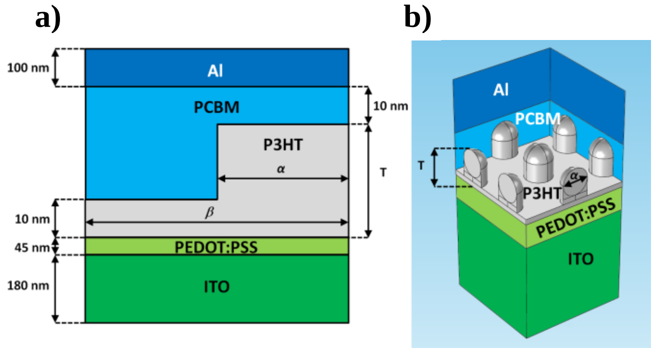

Fig.2. Schematic unit cell (periodic conditions) of the structure ITO/PEDOT:PSS/P3HT/PCBM/Al for a) the 2D and b) the 3D models.

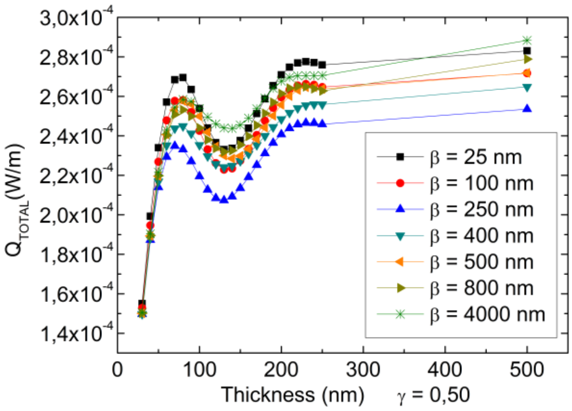

Fig.3. Total absorbed light power (Q_{TOTAL}) in the P3HT layer of the 2D model as a function of the nanopillars height (T) for several structure periods (β) for $\gamma = \alpha/\beta = 0.5$.

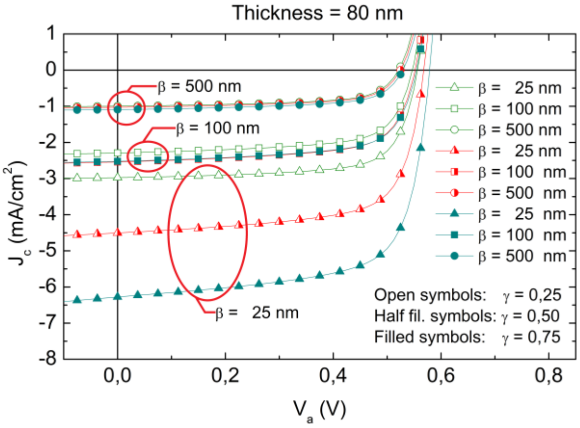

Fig.4. J–V curves for the 2D model for T = 80 nm for several β and for different $\gamma = \alpha/\beta$.

	TABLE 1: CELLS EFFICIENCY (%)		
	***T* = 80 nm, *γ* = 0.25**	***T* = 80 nm, *γ* = 0.50**	***T* = 80 nm, *γ* = 0.75**
***β* = 25 nm**	1,18	1,76	2,49
***β* = 100 nm**	0,85	0,95	0,95
***β* = 500 nm**	0,34	0,35	0,38
BEST PLANAR BILAYER REFERENCE CELL (*T* = 60 nm):			0,69

Table1. Cells efficiencies obtained from Fig. 5 J-V curves.

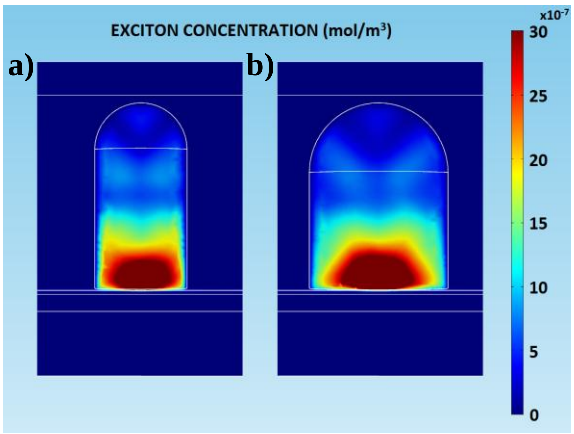

Fig.5. Exciton concentration map of a cell for the 3D model for β = 500 nm, T = 510 nm, and a) γ = 0.50 and b) γ = 0.75.

Modeling the Junctionless DG MOSFETs

Thomas Holtij [1,2,✠], Michael Graef [1,2], Franziska Hain [1,2], Alexander Kloes [1], Benjamín Iñíguez [2]

[1] Competence Center for Nanotechnology and Photonics, Technische Hochschule Mittelhessen, Giessen, Germany
[2] DEEEA, University Rovira i Virgili, Tarragona, Spain
✠thomas.holtij@ei.thm.de

***Abstract*—A 2D physics-based model for short-channel junctionless double gate (DG) MOSFETs is presented. From a closed-form solution for the 2D potential we derive explicit equations for the calculation of threshold voltage V_T and subthreshold slope S. A unified charge model valid for all operating regimes is developed by using Lambert's W-function. The model for the potential is derived with the help of Poisson's equation and the conformal mapping technique by Schwarz-Christoffel. A comparison of our model is done versus 2D TCAD Sentaurus simulation data.**

***Index Terms*—Junctionless double gate MOSFET, 2D analytical modeling, threshold voltage, subthreshold slope, unified charge model, conformal mapping**

I. INTRODUCTION

The junctionless transistor (JLT) is heavily doped, has no junctions, no doping concentration gradients, and provides full CMOS process compatibility. It has improved electrostatic characteristics such as low leakage currents, high I_{on}/I_{off} ratios and a low drain-induced barrier lowering (DIBL). These benefits are due to the absence of the pn-junctions in JLTs. The JLT is turned on when operating at flatband condition and turned off by complete depletion of its channel region, whereby the device's cross section must be small enough in order to deplete the channel. The main conduction mechanism relies on a bulk current (volume conduction) and not on a current flow in a conducting channel at the silicon to oxide interface (surface conduction) as it is the case in conventional MOSFETs [1], [2].

We target a junctionless DG MOSFET structure (Fig. 1). The proposed device uses additional S/D implants to avoid high parasitic access resistances and to increase the conductivity of these regions. In general, the 2D model is developed using Poisson's equation and the conformal mapping technique by Schwarz-Christoffel. Electrical parameters such as V_T and S are calculated and a unified charge model is derived using Lambert's W-function. A simple current equation makes the model complete.

II. MODELING THE JLT

The main goal of the work is to develop closed-form expressions which describe the properties of JLTs. Poisson's equation of an n-type JLT inside the channel region reads as

$$\Delta\phi(x,y) = -\frac{\rho}{\epsilon} = -\frac{q\,N_D}{\epsilon_{Si}}. \tag{1}$$

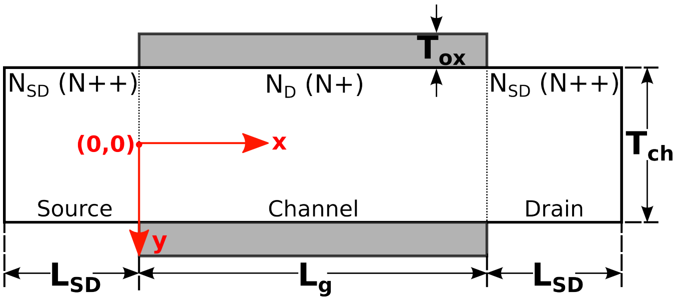

Fig. 1. Longitudinal cross section of the proposed DG JLT showing its physical device dimensions, doping profile, and coordinate system. N_D is the channel, and N_{SD} the source/drain doping concentration.

q is the elementary charge, N_D the doping concentration inside the channel region, and ϵ_{Si} the permittivity of the silicon. In order to calculate the potential two-dimensionally, the solution of Poisson's equation is decomposed into separate parts: a 1D solution $\phi_p(y)$ and a 2D solution $\varphi(x,y)$.

$$\Delta\phi(x,y) = \Delta\phi_p(y) + \Delta\varphi(x,y) \tag{2}$$

We neglect quantum mechanical effects (QMEs), because the channel thickness is set to $10\,\mathrm{nm}$ [3] and the source/drain regions are cut out to simplify matters. To avoid discontinuities of the electric field at the $\mathrm{Si}-\mathrm{SiO_2}$ interface, a scaled oxide thickness is used ($\tilde{T}_{ox} = \epsilon_{Si}\,T_{ox}/\epsilon_{ox}$) with $\epsilon_{ox} = 7\,\epsilon_0$ [4]. The potential is calculated with the conformal mapping technique by Schwarz-Christoffel. This means to map the geometry of the JLT from one plane to another one with less complexity. By applying Poisson's integral in the transformed plane [5], closed-form expressions for the potential were found [6].

The closed-form solution of the 2D potential enables us to derive an expression for the threshold voltage V_T and subthreshold slope S of JLTs. Using an expression for the integral mobile charge at the potential barrier inside the channel region below threshold voltage and separate expressions for the mobile charges in depletion and accumulation region, a unified charge model is developed, which takes into account 2D effect. The charges at source and drain end of the channel are calculated and inserted into the final current equation.

$$I_d = \mu\,W_{ch}\left[\frac{V_{th}}{L_g}\;(Q_s - Q_d) + \frac{(Q_s^2 - Q_d^2)}{4\,L_g\,C'_{ox}}\right] \tag{3}$$

III. MODEL VERIFICATION

The model is compared versus 2D TCAD Sentaurus simulations. The simulations settings are: a standard drift-diffusion transport model, a constant mobility $\mu = 300\,\mathrm{cm}^2/\mathrm{Vs}$ and a temperature of $T = 300\,\mathrm{K}$. We used a device width of $W_{ch} = 1\,\mu\mathrm{m}$.

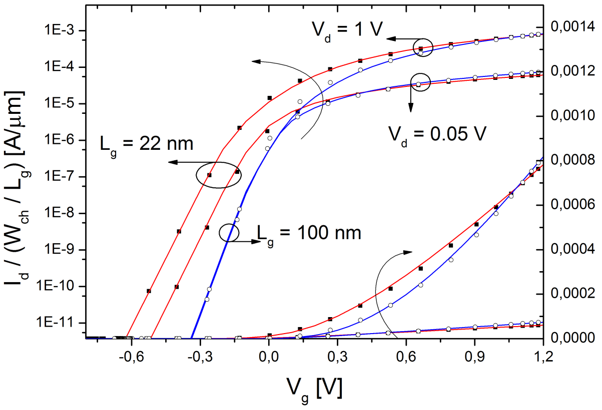

Fig. 2. Transfer characteristics of DG JLT with I_d normalized by (W_{ch}/L_g). Parameters: $V_d = 0.05\,\mathrm{V}, 1\,\mathrm{V}$, $N_D = 1{\cdot}10^{19}\,\mathrm{cm}^{-3}$, $L_g = 22\,\mathrm{nm}, 100\,\mathrm{nm}$, $L_{sd} = 10\,\mathrm{nm}$, $T_{ch} = 10\,\mathrm{nm}$, $T_{ox} = 2\,\mathrm{nm}$. Symbols TCAD; lines model.

At first sight, one can observe that the model agrees well with the simulation data (Fig. 2). It becomes clear that the channel length has a noticeable influence on the device performance. At short channel sizes the current is very high, but at the cost of the performance below threshold voltage. The electrical parameters are summarized in Table I (for $V_d = 0.05\,\mathrm{V}/1\,\mathrm{V}$) and λ as the slope degradation factor. The DIBL in this case is defined in terms of a threshold voltage shift $(V_T|_{V_d=0.05\,\mathrm{V}} - V_T|_{V_d=1\,\mathrm{V}})$

TABLE I
EXTRACTED ELECTRICAL PARAMETERS OF FIG. 2.

L_g [nm]	V_T [V]	S [mV/dec]	DIBL [mV]	λ [−]
22	-0.1 / 0.02	85 / 86	120	1.43 / 1.46
100	0.07 / 0.07	59 / 59	0	1 / 1

The channel doping concentration N_D was altered in Fig. 3, whereby the source/drain doping concentrations N_{SD} were kept constant. The following Table II contains the extracted electrical parameters, where $V_d = 1\,\mathrm{V}$. We can identify a strong dependency of V_T on the N_D, especially when $N_D > 10^{19}\,\mathrm{cm}^{-3}$ (V_T roll-off). This effect implies that JLTs are rather not immune to variability due to the possible random dopant fluctuation (RDF) effect, which is one of their major issues up-to-date. S was found to remain unchanged even for very high doping concentrations.

TABLE II
EXTRACTED ELECTRICAL PARAMETERS OF FIG. 3.

N_D [cm^{-3}]	$1 \cdot 10^{18}$	$5 \cdot 10^{18}$	$1 \cdot 10^{19}$	$2 \cdot 10^{19}$
V_T [V]	0.28	0.09	0.02	-0.59
S [mV/dec]	86	86	86	86

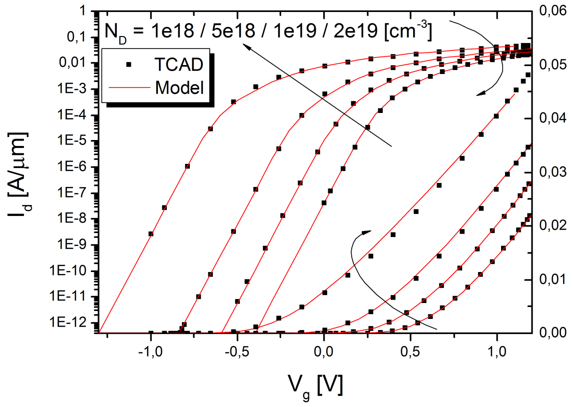

Fig. 3. Transfer characteristics of junctionless DG transistor. Parameters: $V_d = 1\,\mathrm{V}$, $N_D = 1{\cdot}10^{18}/\,5{\cdot}10^{18}/\,1{\cdot}10^{19}/\,2{\cdot}10^{19}$ [cm^{-3}], $L_g = 22\,\mathrm{nm}$, $L_{sd} = 10\,\mathrm{nm}$, $T_{ch} = 10\,\mathrm{nm}$, $T_{ox} = 2\,\mathrm{nm}$. Symbols TCAD; lines model.

IV. CONCLUSION

The 2D physically-based model was successfully compared with 2D TCAD simulation data. The charge model takes carefully into account the transition from the depletion to the accumulation regime by using appropriate effective gate capacitances. Important effects, such as the strong dependency of V_T on N_D, or the constant S for altering N_D, were worked.

ACKNOWLEDGEMENT

This project was supported by German Federal Ministry of Education and Research under contract No.1779X09, by German Research Foundation (DFG) under Grant KL 1042/3-1, by the European Commission under FP7 Projects ICTSTREP 257111 ("SQWIRE"), and IAPP-218255 ("COMON"), by the Spanish Ministerio de Ciencia y Tecnología under Projects TEC2011-28357-C02-01, by the PGIR/15 Grant from URV and also by the ICREA Academia Prize.

REFERENCES

[1] C.-W. Lee, A. Afzalian, N. D. Akhavan, R. Yan, I. Ferain, and J.-P. Colinge, "Junctionless multigate field-effect transistor," *Applied Physics Letters*, vol. 94, no. 5, pp. 97–103, 2009.
[2] J.-P. Colinge, A. Kranti, R. Yan, C. Lee, I. Ferain, R. Yu, N. D. Akhavan, and P. Razavi, "Junctionless Nanowire Transistor (JNT): Properties and design guidelines," *Solid-State Electronics*, vol. 65-66, pp. 33–37, 2011.
[3] Y. Omura, S. Horiguchi, M. Tabe, and K. Kishi, "Quantum-mechanical effects on the threshold voltage of ultrathin-SOI nMOSFETs," *IEEE Electron Device Letters*, vol. 14, no. 12, pp. 569–571, 1993.
[4] A. Kloes and A. Kostka, "A new analytical method of solving 2D Poisson's equation in MOS devices applied to threshold voltage and subthreshold modeling," *Solid-State Electronics*, vol. 39, no. 12, pp. 1761 – 1775, 1996.
[5] Weber, *Electromagnetic Fields*. Wiley, 3 ed., 1950.
[6] M. Schwarz, M. Weidemann, A. Kloes, and B. Iniguez, "Analytical compact modeling framework for the 2D electrostatics in lightly doped double-gate MOSFETs," *Solid-State Electronics*, vol. 69, no. 0, pp. 72 – 84, 2012.

Fabrication and characterization of self-ordered nanoporous anodic alumina bilayers with potential biosensing applications

G. Macias, L. P. Hernández-Eguía, J. Ferré-Borrull, J. Pallarès, P. Formentín and L.F. Marsal

Departament d'Enginyeria Electrònica, Elèctrica I Automàtica, ETSE, Universitat Rovira I Virgili. Avda. Països Catalans 26, 43007 Tarragona, Spain.
E-mail: lluis.marsal@urv.cat

Abstract

In this work we present a novel nanoporous anodic alumina structure consisting in self-ordered double layers with different porosities i.e. a top layer with large pores and a bottom layer with small pores. The resulting reflectance spectrum consists of a complex series of Fabry-Pérot interferences which, analyzed by the fast Fourier transform method, show potential applications for biosensing applications.

1.Introduction

Nanoporous anodic alumina (NAA) with pore diameters between 15 and 300 nm have shown promising results in areas such as optoelectronics [1] and materials science [2]. However, recently there has been an increasing interest in their possible application in biosciences, especially in label-free detection of biomolecules. To date, the studied approaches rely on self-ordered anodic alumina monolayers. These studies show promising results, but further investigation has been focused on surface modification and protein immobilization instead of structure modification. Here, we present our results in self-ordered nanoporous anodic alumina bilayers, focusing on fabrication, characterization and data processing for a further application as a biosensing platform.

2. Experimental

Conventional two-step anodization [3] was performed on high-purity aluminium sheets (99.99% Ø20 mm 250 µm thick) purchased from Goodfellow Cambridge Ltd. Prior to anodization, a 4-min electropolishing pretreatment was performed in a mixture of ethanol (EtOH) and perchloric ($HClO_4$) acid 4:1 v/v at 20 V. Afterwards, the polished surface was anodized in oxalic acid ($H_2C_2O_4$ 0.3 M) at 40V and 4-6 ºC for 20 h in order to achieve self-ordering of pores. The grown aluminium oxide was then selectively dissolved in a mixture of phosphoric (H_3PO_4 6%wt.) and chromic acid (H_2CrO_7 1.8 %wt.) at 70 ºC for at least 3 h. A second anodization was performed under the same conditions but adjusted to obtain 1, 2, 3 and 4 µm respectively. Subsequently, pores were enlarged through wet chemical etching with phosphoric acid (5 %wt.) for 15 min. Finally, a third anodization took place under the same conditions in order to obtain a less porous 4-µm-thick second alumina layer. Fig.1 shows a top view of the samples and a scheme of the overall structure.

Reflectance spectra were recorded for all samples in the 350-600 nm range using a PE Lambda 950 UV-Vis-NIR spectrometer at normal incidence. In order to establish the effective optical thickness (EOT) of each layer, fast Fourier transform (FFT) analysis was performed following a procedure described elsewhere [4].

3.Results & Discussion

Fig. 2 shows the resulting reflectance spectra of the NAAB. The complex series of oscillations are due to the combination of the various reflections at the interfaces depicted in fig.1 a). To successfully interpret these spectra, a FFT analysis was performed. Fig. 4 shows the resulting frequency plots the several NAAB. The two FFT peaks present in the frequency domain correspond to the EOT of layers 2 and 3 as depicted in Fig.1 a). However, according to literature regarding porous silicon bilayers, a third peak corresponding to layer 1 should be visible in the FFT [4]. This is explained by the little difference in the refractive index between top layer of the NAAB ($n_1 \approx 1,3$) and the refractive index of the surrounding media ($n_{air} \approx 1,0$). This small refractive index contrast leads to very small amplitude of the FFT peak for layer 1. In addition, the overall reflectance shape is represented in the FFT as a band at 0 nm and masks the peak for layer 1.

4.Conclusions

We have presented an easy approach for the fabrication of alumina bilayers with potential application in optical detection of biomolecules. FFT allows us to have a more robust and automated way of measuring the EOT. In addition, the FFT plot gives information in both axis. The peak position is related with the EOT of each of the layers, while peak intensity is related with the refractive index contrast between two consecutive layers. Bilayers show promising results as they provide more information than monolayers thanks to their multiple FFT peaks which will be useful to follow functionalization and biomolecule immobilization. Finally, pore diameters can be tuned to promote or inhibit the entrance of certain macromolecules such as proteins and thanks to its funnel architecture give information of protein size.

Name	Layer 1 (µm)	Porosity 1 (%)	Layer 2 (µm)	Porosity 2 (%)
S1	1	50	4	10
S2	2			
S3	3			
S4	4			

Table 1. Geometric characteristics of the NAAB.

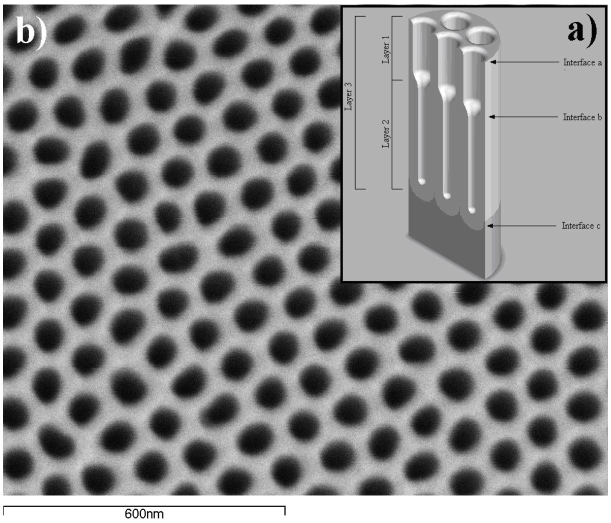

Fig.1. a)schematic view of the NAAB structure with two defined NAA layers with different porosities and displaying three interfaces. b)top view of a NAAB sample showing highly ordered pores in a honeycomb-like manner.

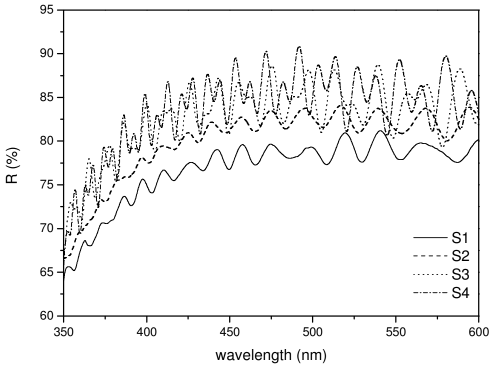

Fig.2. Reflectance spectra of NAA bilayers in the 350-600 nm range. The oscillations present in the spectra are due to the combination of the intereference fringes of both layers.

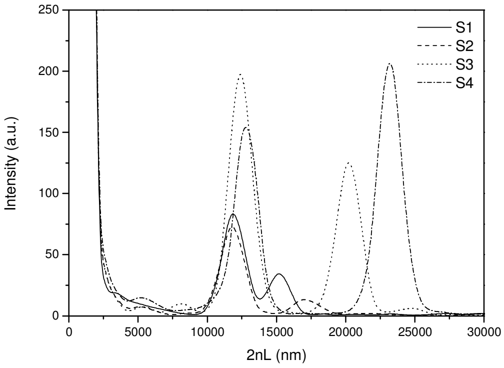

Fig.3. FFT plot of the reflectance spectra from Fig.2 of the NAA bilayers listed in Table 1. The peaks' position correspond to the EOT (i.e. 2nL=EOT) of the layer.

Acknowledgments

This work was supported by the Spanish Ministry of Economy and Competitiveness (MINECO) under grant no. TEC2012-34397, and Government of Catalonia AGAUR 2009 SGR 549.

References

[1] X.H. Wang, T. Akahane, H. Orikasa, T. Kyotani, Applied Physics Letters, **91** (2007) 011908.

[2] T. Yanagishita, K. Nishio, H. Masuda, Advanced Materials, **17** (2005) 2241-2243.

[3] H. Masuda, K. Fukuda, Science, **268** (1995) 1446-1448.

[4] S. Pace, B. Seantier, E. Belamie, N. Lautredou, M.J. Sailor, P.E. Milhiet, F. Cunin. Langmuir **28** (2012) 6960-6969.

[5] A. Santos, M. alba, P. Formentin, J. Ferré-Borrull, J. Pallarès, L.F. Marsal, Advanced Materials **24** (2012) 1050-1054.

[6] A. Santos, G. Macias, J. Ferré-Borrull, J. Pallarès, L.F.Marsal, ACS Applied Materials & Interfaces **7** (2012) 3584-3588

The effect of solvent on the performance and morphology of PTB1:PC$_{61}$BM solar cells

P.L. Han, V.S. Balderrama, P. Formentin, J. Pallarés and L.F. Marsal*

Departament d'Enginyeria Electrònica, Elèctrica i Automàtica, Universitat Rovira i Virgili, Av. Paisos Catalans 26,
Tarragona, Spain
Phone: (+34) 977 55 96 25 *E-mail address: lluis.marsal@urv.cat

Abstract

The morphology of the photoactive layer is very important for the photovoltaic performance of solar cells. Bi-continuous interpenetrating network morphology of donor and acceptor is crucial for exciton separation and transport of electrons and holes to their respective electrode in the polymer solar cells. Here, we present a simple solution processed approach to control the morphology of the active layer in the fabrication of the PTB1:PC$_{61}$BM blend solar cells by using the mixture of dichlorobenzene (DCB) and chloroform (CF) as solvent. The results show that the mixture solvent can effectively improve the micro-phase separation of the active layer and increase the short current circuit of solar cells.

Introduction

Organic photovoltaic (OPV) solar cells based on photonics technology have been widely investigated as they show the promise of solar energy conversion efficiencies at low cost and ease of fabrication [1, 2]. In the past decades, much research has focused on optimization of device performance to improve the efficiency of the device. In the optimization of OPV structure, morphology controlled can affect significantly the performance of cells by using the different solvent [3, 4]. A good interpenetrating network morphology can increase the micro-phase separation and improve the transport of the charge carriers across the interface between the active layer and electrode. In current research, a low band gap polymer PTB1 has attracted much attention because power conversion efficiency (PCE) around 9% has been achieved [5, 6]. Herein, correlation between the controlling morphology of the active layer of PTB1:PC$_{61}$BM blends by using the different solvent and device performance were investigated.

Experiment section

Photovoltaic (PV) devices were fabricated on pre-cleaned patterned ITO glass substrates. The ITO-coated glass substrate was cleaned stepwise in acetone, methanol, isopropanol, distilled water for 20min each. And then it was dried in an oven for 10 h at 60 ℃. A 30 nm hole extraction layer PEDOT: PSS was applied onto the substrates by spin coating. After being baked at 120 ℃ for 20 min, the PTB1: PC$_{61}$BM film with 1:1 weigh ratio and PTB1 concentration of 15 mg/ml dissolved in DCB or the mixture of DCB and CF was cast on the PEDOT: PSS layer at 1000 rpm for 30 s without further treatment inside a glove box. Subsequently, 100 nm Ag layer on top of 25 nm Ca layer were thermally deposited on the organic activity film under high vacuum (1x 10^{-6} Pa). The current-voltage curves were measured using a Keithley 2400 source measure unit under AM1.5G illumination at 100 mW/cm^2. Atomic force microscopy (AFM) topographic and phase image of the row sample in the tapping mode on a molecular imaging model Pico SPM II.

Results and discussion

The PTB1 shows good solubility in chloroform (CF). Meanwhile, high boiling point solvents can delay the solvent evaporation speed and improve crystallinity of active layer that are commonly used for the fabrication of OPVs, such as chlorobenzene (CB) and 1,2-dichlorobenzene (DCB). A mixed solvent approach was used here. Result of the current density-voltage characterization is shown in Fig. 1. When only DCB is used as the solvent, low short circuit current (Jsc) and good fill factor (FF) were obtained. If mixture of DCB:CF (2:1 volume ratio) used in the process as solvent, Jsc is significantly improved from 10.6 mA/cm^2 to 12.15 mA/cm^2 with respect DCB process. The average PCE is increase from 4.32% to 4.58%. The performance of cells processed with different solvent is related to the morphology of the active layer. AFM measurements (Fig. 2) provide information about the morphology. The topography and phase images of blend layer from DCB dispersions display large dimensions from tens of nm to 100 nm of domains and the poor interpenetrating network are shown in Fig.2a, a'. While solvent is mixture of DCB and CF, a significant reduction of the small dimension of the micro-phase separated domains is obtained (Fig.2b, b'). The interpenetrating network phase of PTB1:PCBM blend layer is improved obviously, which is beneficial to the exciton charge separation and charge transport in the interfaces of donor and acceptor. The favorable small feature of the PTB1:PCBM blend active layer induces the generation of charge carriers and increases the effectiveness of active layers, leads to a high short circuit current and high efficiency of 12.15 mA/cm^2 and 4.58%, respectively.

Conclusions

In conclusion, we have demonstrated that the use of solvent mixture of dichlorobenzene and chloroform can efficiently enhance the interaction between PTB1 and $PC_{61}BM$. The AFM results show good network morphology of PTB1:$PC_{61}BM$ blend film after solvent mixture trained. The favorable interpenetrating network may effectively increase the exciton charge separation and transport efficiency and result in the high Jsc.

Acknowledgements

This work was supported by the Spanish Ministry of Economy and Competitiveness (MINECO) under grant number TEC2012-34397, CONSOLIDER HOPE project CSD2007-00007, by Catalan authority under project 2009 SGR 549.

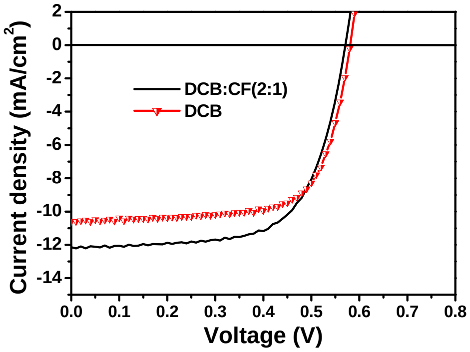

Fig.1. Current density–voltage measurements under AM1.5G illumination (100 mW/cm^2) of PTB1:$PC_{61}BM$ devices made from two different solvents

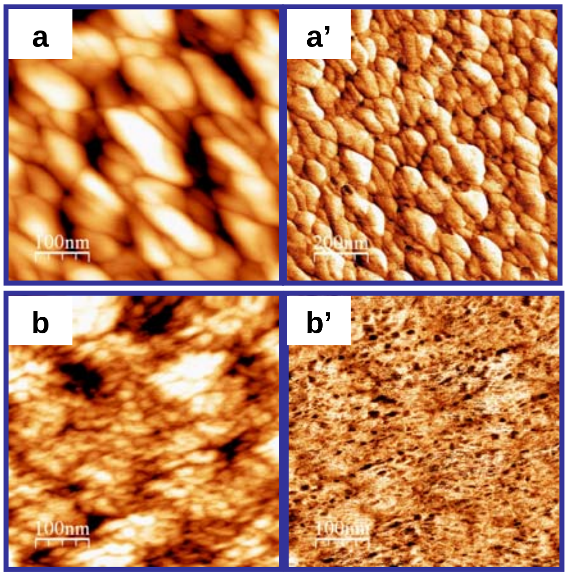

Fig.2. (a, a') Surface topography and phase image of PTB1:$PC_{61}BM$ film processed from DCB; (b, b') Surface topography and phase image of PTB1:$PC_{61}BM$ film processed from DCB:CF solvent mixture (2:1 volume ratio).

References

[1] B. Kippelen, B. J. Luc, "Organic photovoltaics", *Energy Environ. Sci*, 2, 251-261, 2009.

[2] W.Gaynor, L. J. Yong, "Fully solution-processed inverted polymer solar cells with laminated nanowire electrodes", *ACS Nano*, 4, 30-34, 2010.

[3] S. E. Shaheen, C. J. Brabec, N. S. Sariciftci, F. Padinger, T. Fromherz, "2.5% efficient organic plastic solar cells", *Appl. Phys. Lett*, 78, 841– 843, 2001.

[4] S. H. Park, A. Roy, S. Beaupré, S. Cho, N. Coates, J.S. Moon, D. Moses, M. Leclerc, K. Lee , A. J. Heeger, "Bulk heterojunction solar cells with internal quantum efficiency approaching 100%", *Nature Photon*, 3, 297-302, 2009.

[5] Y. Liang, Y. Wu, D. Feng, "Development of New Semiconducting Polymers for High Performance Solar Cells", *J. Am. Chem. Soc*, 131, 56-57, 2009.

[6] Z.C. He, C.M. Zhong, S.J. Su, M. Xu, H.B. Wu, Y. Cao, "Enhanced power-conversion efficiency in polymer solar cells using an inverted device structure", *Nature Photon*, 6, 591-595, 2012.

Fabrication of biodegradable polymer micro- and nanostructures by template synthesis

A. Słota, P. Formentín, V. Balderrama, M. Baranowska, L.F. Marsal

Departament d'Enginyeria Electrònica, Elèctrica i Automàtica, Universitat Rovira i Virgili
Avda. Països Catalans 26, 43007 Tarragona, Spain
lluis.marsal@urv.cat

Abstract

In the present work we report on the fabrication of biocompatible polymer micro- and nanostructures by replica molding technique. Poly(D,L-lactide) films with various morphologies were obtained by using porous silicon and alumina hard templates with different pore sizes and geometries.

1. Introduction

Synthetic polymers capable of undergoing hydrolytic or enzymatic degradation in a controlled manner have become of a great interest in biomedicine and during the recent years they have been extensively investigated for use as biodegradable therapeutic devices, drug carriers and tissue engineering scaffolds [1, 2]. Several processing technologies have been developed to fabricate polymeric biomaterials with microscale and nanoscale features. Among them, template synthesis appears as one of the most promising methods due to its simplicity, versatility and relatively low cost [3]. The process involves the infiltration of a polymeric fluid (melt or solution) into a mold with a desired pattern, solidification of the polymer and finally the removal of the template. This technique allows to create large-area polymer surfaces with well-defined nanofeatures such as pillars, grooves, wells and more.

We used template synthesis to obtain biodegradable poly(D,L-lactide) (PDLLA) replicas from anodic aluminium oxide and macroporous silicon molds. The intention of our work was to generate polymer biomaterials which can be used in future research as cell culture substrates to analyze the influence of different topographies on cell growth and prolifereation [4].

2. Experimental

The alumina templates with ordered pores structure were obtained by two-step anodization process in 1 wt% phosphoric acid solution at 195V and 0ºC followed by pore-widening treatment in 5 wt% H_3PO_4. Macroporous silicon samples were prepared by anodizing Si substrates in hydrofluoric acid-dimethylformamide electrolyte (HF:DMF 1:10 v/v) at 5mA· cm^{-2} for 10 minutes. Laser lithography and electrochemical etching were used to produce silicon templates with regular pyramid-like pattern.

The fabrication of poly(D,L-lactide) 3D structures was carried out by spin-coating the polymer solution onto the glass substrate and pressing the heated polymer against the porous template, followed by mechanical detachment of the PDLLA film from the mold. In order to minimize the adhesion between the polymer pillars formed within the pores and the pore walls, the alumina and silicon templates were functionalized with monoglycidyl ether terminated poly(dimethylsiloxane) (PDMS, M_n=5000) [5, 6]. Prior to silanization, the alumina samples were immersed in boiling 30% solution of hydrogen peroxide for 30 minutes and the silicon samples were pre-treated with 0.1M solution of potassium hydroxide (3 minutes) and 0.1M solution of nitric acid (10 minutes) in order to create hydroxyl groups on the surface. Subsequently both alumina and silicon samples were placed in 1 vol% solution of 3-(aminopropyl triethoxysilane) (APTES) in toulene and mixed for 2h at room temperature. The APTES-modified templates were then reacted with monoglycidyl ether terminated PDMS at 80ºC for 4h to form antiadhesion coating on their surfaces.

PDLLA solution in chloroform (40mg/ml) was spin-coated on the glass substrate at 1000rpm for 30 seconds. The substrate was placed on the template, pressed and heated at 120ºC in the oven for several minutes. The sample was slowly cooled to room temperature and the polymer film was torn off with tweezers.

To characterize the structure of the silicon and alumina templates and the resulting PDLLA pillars the environmental scanning electron microscope (ESEM) was used.

3. Results and discussion

Figure 1 shows the ESEM images of fabricated poly(D,L-lactide) structures and the corresponding alumina and silicon templates. In all cases it was possible to obtain an accurate transfer of the mold

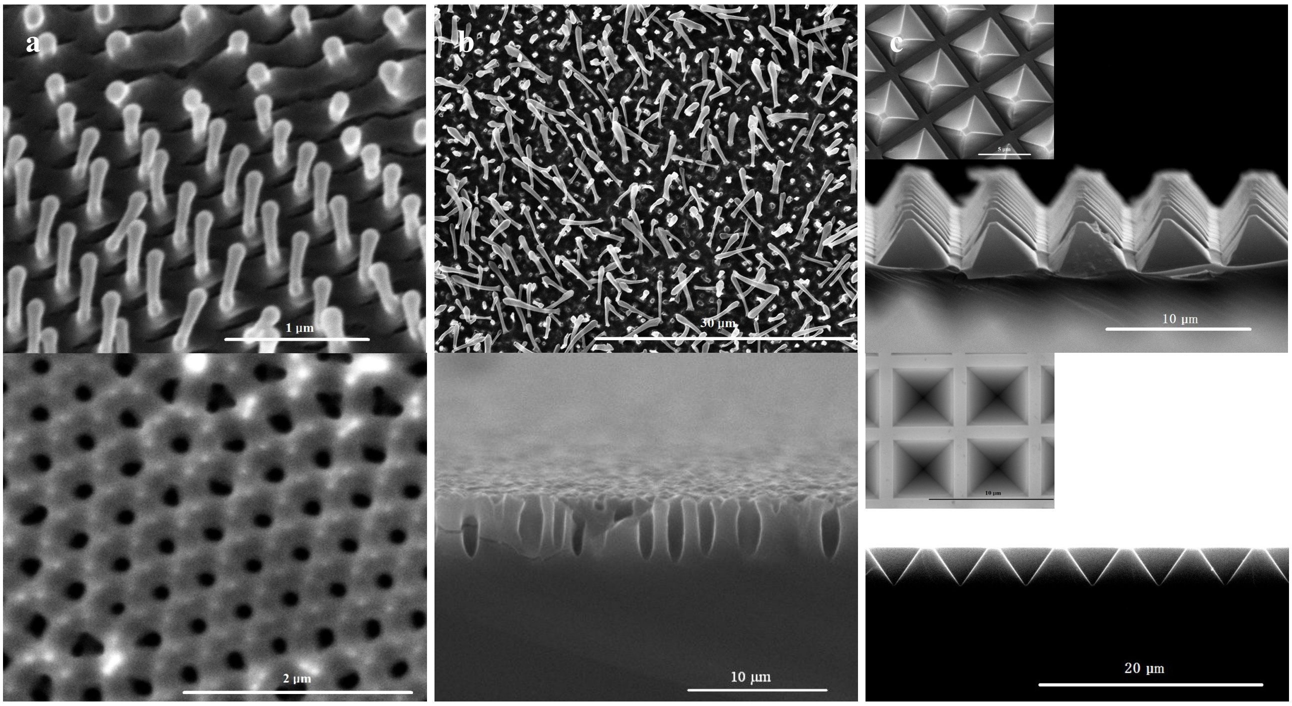

Fig. 1. ESEM images of fabricated PDLLA structures and the corresponding alumina and silicon templates.

pattern onto polymer film. As the result of the infiltration of a polymeric solution into anodic aluminium oxide ordered arrays of free-standing nanopillars were formed (Fig.1a). The height of the nanopillars was approximately 500nm, which corresponds to the thickness of the porous layer of alumina template. The diameter of the nanopillars was found to be slightly decreased comparing to the size of alumina pores (90-110nm for nanopillars and ca. 120nm for AAO nanopores). When macroporous silicon was used as a template, disordered PDLLA pillars with the height of 4-6 µm and the average diameter of ca. 400 nm were obtained (Fig. 1b). Because of the high aspect ratio (~10) the micropillars have a tendency to bend and adhere to each other. Regular pattern of three-dimensional pyramid-shaped features was replicated from silicon mold prepared by lithography technique (Fig. 1c). The lateral pyramid size was about 5 µm and the height was 4 µm which is in good agreement with the dimensions of silicon microstructures.

4. Conclusions

Poly(D,L-lactide) nanopillars, micropillars and micropyramids were successfully replicated from porous alumina and silicon templates. The structural dimensions of the fabricated features were similar to the ones of the templates. Surface functionalization of alumina and silicon molds with PDMS allowed to detach them from PDLLA film in a non-destructive manner, so the templates could be reused several times. Further work will be carried out to improve the fabrication process in order to create materials with enhanced structural parameters. Application of the obtained PDLLA structures as cell culture substrates will be investigated in the future.

5. Acknowledgements

This work was supported by the Spanish Ministry of Economy and Competitiveness (MINECO) under grant number TEC2012-34397 and by Catalan Government under project AGAUR 2009 SGR 549.

References

[1] Q. Liu, L. Jiang, R. Shi, L. Zhang, “Synthesis, preparation, in vitro degradation and application of novel degradable bioelastomers – A review”, Prog. Polym. Sci. 2012, 37, 715– 765.

[2] L. S. Nair, C. T. Laurencin, “Biodegradable polymers as biomaterials”, Prog. Polym. Sci. 2007, 32, 762–798.

[3] J. Martín, J. Maiz, J. Sacristan, C. Mijangos, “Tailored polymer-based nanorods and nanotubes by "template synthesis": From preparation to applications”, Polymer 2012, 53, 1149-1166.

[4] M. Nikkhah, F. Edalat, S. Manoucheri, A. Khademhosseini, “Engineering microscale topographies to control the cell-substrate interface”, Biomaterials 2012, 33, 5230-5246.

[5] M. J. Lee, N. Y. Lee, J. R. Lim, J. B. Kim, M. Kim, H. K. Baik, Y. S. Kim, “Antiadhesion surface treatments of molds for high-resolution unconventional lithography”, Adv. Mater. 2006, 18, 3115–3119.

[6] M. K. Choi, H. Yoon, K. Lee, K. Shin, “Simple fabrication of asymmetric high-aspect-ratio polymer nanopillars by reusable AAO templates”, Langmuir 2011, 27, 2132–2137.

Compact Physical Models for Gate Charge and Gate Capacitances of AlGaN/GaN HEMTs

F.M. Yigletu[1*], S. Khandelwal[2], T.A. Fjeldly[2] and B.Iñiguez[1]

[1]Dept. of Electrical Electronics and Automation Engineering, Universitat Rovira i Virgili, Spain

[2]Dept. of Electronics and Telecommunication, Norwegian University of Science and Technology, NTNU, Norway
*email: fetenemulugeta.yigletu@urv.cat, tel. (+34) 977-256190

I. INTRODUCTION

AlGaN/GaN HEMTs are essential devices for high power and high frequency circuits. Therefore, accurate modeling of these devices is critical for the design of such circuits. In this work we present physical analytical models for the gate charge and gate-source and gate-drain capacitances of AlGaN/GaN HEMTs. A continuous total gate charge model is developed first, from which the capacitances are derived. The gate charge model is developed using a simple charge control model [1]. The model shows good agreement with experimental data.

II. ANALYTICAL MODEL

In the triangular quantum well created at the interface of AlGaN/GaN the second energy level is much higher than the first one and is well above the Fermi level for the whole operating range of the gate voltage. The details of this assumption and the current model developed based on this are presented in an earlier work [1]. The simple charge control model developed based on this assumption is given as [1]

$$V_{g0} - V = \frac{qdn_s}{\varepsilon} + \gamma_0 n_s^{2/3} + V_{th} \ln\left(n_s \big/ DV_{th} \right). \quad (1)$$

The gate charge is obtained by integrating the charge density along the channel which is given as

$$Q_G = W \int_0^L q n_s(x)\, dx \quad (2)$$

where L is the channel length and W is the channel width, n_s is charge carrier density and q is the electron charge. From a similar expression of the drain-source current, dx can be substituted which will change the integration variable from x to V. Therefore, the charge per unit area can be written as

$$Q_G = WLq \frac{\int_{V_s}^{V_d} n_s^2 dV}{\int_{V_s}^{V_d} n_s dV} \quad (3)$$

where d is the barrier layer thickness, D is the density of states, ε is the dielectric permittivity and γ_0 is extracted from measurements [1]. The derivative of the voltage w.r.t n_s can be obtained from (1) and is given as

$$dV = -\left(\frac{qd}{\varepsilon} + \frac{2}{3}\gamma_0 n_s^{-1/3} + V_{th} n_s^{-1} \right) dn_s. \quad (4)$$

After integrating (2) using (4), the gate charge becomes

$$Q_G = WLq \frac{\frac{qd}{3\varepsilon}\left(n_D^3 - n_S^3\right) + \frac{1}{4}\gamma_0\left(n_D^{8/3} - n_S^{8/3}\right) + \frac{1}{2}V_{th}\left(n_D^2 - n_S^2\right)}{\frac{qd}{2\varepsilon}\left(n_D^2 - n_S^2\right) + \frac{2}{5}\gamma_0\left(n_D^{5/3} - n_S^{5/3}\right) + V_{th}\left(n_D - n_S\right)} \quad (5)$$

where n_S and n_D are the charge carrier densities calculated at the source and drain respectively [1]. If we let

$$f(n_S) = \frac{qd}{3\varepsilon}\left(n_D^3 - n_S^3\right) + \frac{1}{4}\gamma_0\left(n_D^{8/3} - n_S^{8/3}\right) + \frac{1}{2}V_{th}\left(n_D^2 - n_S^2\right) \quad (6)$$

$$g(n_S) = \frac{qd}{2\varepsilon}\left(n_D^2 - n_S^2\right) + \frac{2}{5}\gamma_0\left(n_D^{5/3} - n_S^{5/3}\right) + V_{th}\left(n_D - n_S\right) \quad (7)$$

then the gate-source and the gate-drain capacitances can now be calculated as the partial derivative of the gate charge in terms of the corresponding source and drain terminal voltages respectively. Therefore, the capacitances are given as

$$C_{Gx} = WLq \frac{\frac{\partial f(n_s)}{\partial V_x} g(n_s) - f(n_s) \frac{\partial g(n_s)}{\partial V_x}}{\left(g(n_s)\right)^2} \quad (8)$$

where $V_x = V_s$ at the source terminal and $V_x = V_d$ at the drain terminal. However, $f(n_S)$ and $g(n_S)$ can also be defined as

$$f(n_S) = f_{main}(n_D) - f_{main}(n_S) \quad (9)$$

$$g(n_S) = g_{main}(n_D) - g_{main}(n_S) \quad (10)$$

where

$$f_{main}(n_x) = \frac{qd}{3\varepsilon} n_x^3 + \frac{1}{4}\gamma_0 n_x^{8/3} + \frac{1}{2}V_{th} n_x^2 \quad (11)$$

$$g_{main}(n_x) = \frac{qd}{2\varepsilon} n_x^2 + \frac{2}{5}\gamma_0 n_x^{5/3} + \frac{1}{2}V_{th} n_x. \quad (12)$$

From (9) to (12) we see that

$$\frac{\partial f(n_s)}{\partial V_x} = \frac{df_{main}(n_x)}{dV_x}, \frac{\partial g(n_s)}{\partial V_x} = \frac{dg_{main}(n_x)}{dV_x} \quad (13)$$

Therefore, the capacitances can now be expressed as

$$C_{Gx}=WLq\frac{\frac{df_{main}(n_S)}{dV_X}g(n_S)-f(n_S)\frac{dg_{main}(n_S)}{dV_X}}{\left(g(n_S)\right)^2}. \qquad (14)$$

III. RESULTS AND CONCLUSION

The simulated C_{gs} and C_{gd} were compared with measurements. Fig.1 shows the good agreement obtained between measured and simulated C_{gs} . In Fig.2 the measured and simulated C_{gd} are plotted showing good agreement between each other. In addition the output I-V characteristic is also shown in Fig.3 to further confirm the consistency of the capacitance model with the drain current model.

An analytical physical model for the C-V characteristics of AlGaN/GaN HEMT devices has been developed by considering the contribution of only the first energy level in triangular quantum well, which allowed to establish a simple relationship between the applied voltage and the charge carrier concentration. This assumption is valid to the AlGaN/GaN material composition where a considerable part of the 2DEG at the heterostructure interface is located at the first energy level and might not be applicable to triangular quantum well approximation of other heterostructures where the 2DEG is fairly distributed between the first and the second energy levels. For instance, in AlGaAs/GaAs heterostructure the contribution of the second energy level to the 2DEG is considerable, especially in the strong inversion regime and neglecting it could incur a considerable amount of error.

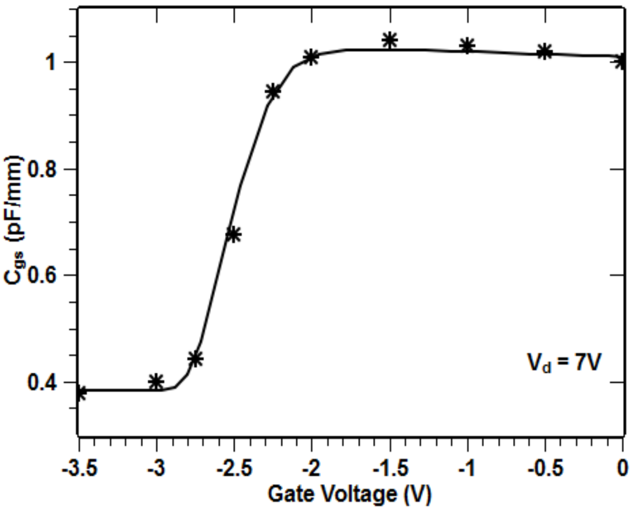

Fig. 1. Measured (symbols) and modeled (solid lines) gate-source capacitance of a device with a gate length of 0.35µm at a drain voltage of 7V data from [3].

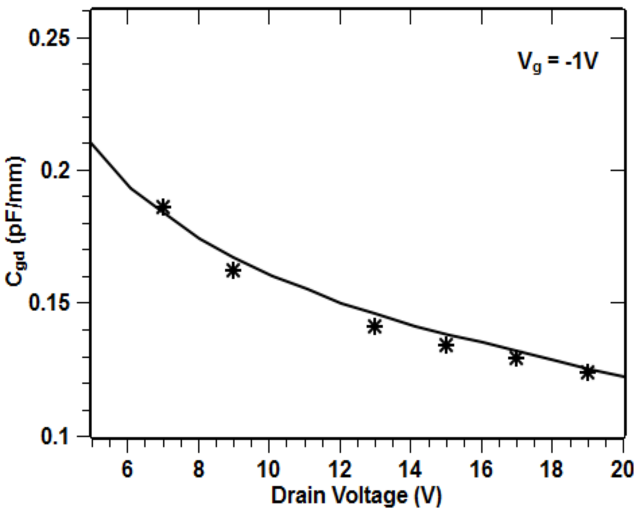

Fig. 2. Measured (symbols) and modeled (solid lines) gate-drain capacitance of a device with a gate length of 0.35µm at a gate voltage of -1V, data from [3].

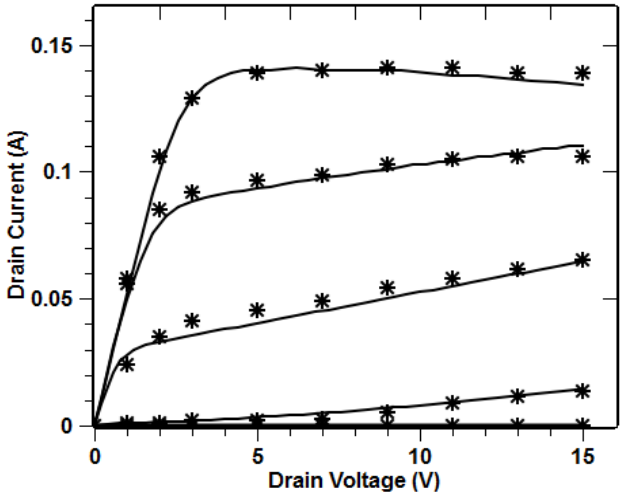

Fig.3. Measured (symbols) and modeled (solid lines) output characteristics of a device with a gate length of 0.35µm when the gate voltage varies from -4V to 0V with a step of 1V, bottom to top, data from [3].

REFERENCES

[1] F.M Yigletu, B. Iñiguez, S. Khandelwal and T.A. Fjeldly, proceedings *of 2013 IEEE Radio and Wireless Week*, pp. 103-105, January 2013, Austin TX, USA.

[2] S. Khandelwal, N. Goyal, T.A. Fjeldly, *IEEE Trans. Elect. Devices*, vol. 58, no. 10, pp. 3622-3625, Oct. 2011.

[3] J.W.Lee and K.J. Webb, *IEEE Trans. Microw. Theory Tech.* vol. 52, no. 1, pp. 2-9, Jan. 2004.

Aerosol Assisted Chemical Vapor Deposition of WO_3 Nanoneedles using Cold Wall Reactor based on Sensor Self-heating

F.E. Annanouch [+], R. Binions [*], E. Llobet [+]

[+]Departament d'Enginyeria Electronica, Universitat Rovira i Virgili, Tarragona, SPAIN,annanouch@gmail.com
[*]School of Engineering and Materials Science, Queen Mary University of London, London, UK

Abstract

This paper reports a new attempt for the deposition of undoped WO3 nanoneedles (NN) on alumina gas sensor using a horizontal AA-CVD cold wall reactor based on self-heating of the sensor deposited. The morphology and the crystalline structure of the film were characterized by using scanning electron microscopy, x-ray diffraction and Raman spectroscopy, and the results proved the synthetize of thicker layer of monoclinic WO3 NN with preferred orientation in the [002] direction. The gas sensor properties of the film were also evaluated; we have exposed our sensors to different analytes: Ethanol, H2, and CO and we have compared their responses to those obtained from WO3 sensors fabricated by hot wall reactor. By using this method based on the self-heating of the sensor deposited, we have greatly improved the stability and the sensitivity of the sensor in comparison to those obtained by using a hot wall reactor.

1. Introduction

Aerosol assisted chemical vapor deposition (AA-CVD), is a suitable method for the deposition of metal oxide nanostructures due to the inexpensive equipment involved, the high growth rate etc. This paper reports the deposition of undoped WO3 NN on alumina gas sensor using a horizontal AA-CVD cold wall reactor based on self-heating of the sensor deposited.

2. Principal of AACVD

Aerosol assisted chemical vapour deposition (AACVD) is a variant of the CVD process involving the use of liquid–gas aerosols to transport soluble precursors to a heated substrate. The principle of this method is illustrated in figure.1. The precursor is dissolved in a solvent, and then an aerosol is generated ultrasonically. By a carrier gas, the aerosol droplets are transported to the substrate where the surface of reaction is located. The solvent needs to have the right physical and chemical properties for aerosol formation; the precursors do not need to be volatile but just soluble in the solvent. This allows for the use of a wider range of non-volatile precursors, which are not usable in conventional CVD.

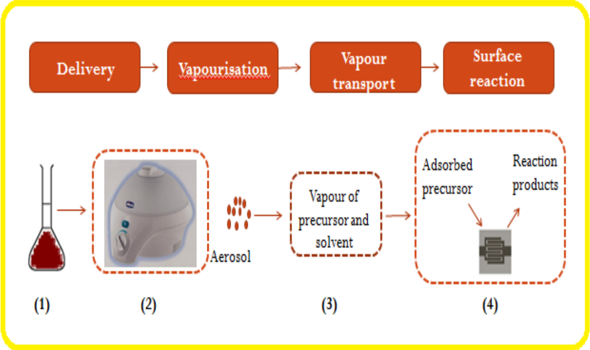

Fig.1. Process of AACVD

3. Experimental section

As a difference to our previous work[1, 2], we have designed a new reactor in Teflon with a holder in which the self-heating sensor substrate is inserted perpendicularly to the direction of the gas flow (see Fig. 2). The sensor substrates consisted of 3×3 mm^2 alumina substrates, with interdigited Au electrodes on the front side and a Pt heating resistor on the back side, that formed one arm of a Wheatstone bridge, allowing its resistance, and so the substrates temperature to be monitored and controlled. The temperature was generated by connecting the sensor heater to an external power supply; furthermore, via a PI controller, the temperature was controlled. To avoid the contact between the heater and the grown WO_3 NN, the heater was coated with a dielectric layer.

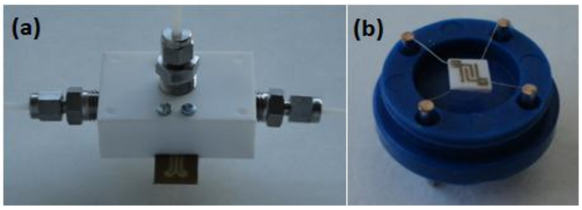

Fig. 2: (a) AACVD cold wall reactor, (b) Alumina gas sensor.

4. Results

Figure 3 shows SEM image of the synthetized WO3 NN deposited at a temperature of 550°C. The obtained NN are similar to the ones obtained in previous works [1, 2] in which a hot wall reactor was employed. XRD pattern of the annealed film indicate the formation of monoclinic WO3 NN and Raman spectroscopy results showed well defined bands at 130, 190, 272, 315,719,803, and 907 cm^{-1} which corresponds to monoclinic phase of WO_3. Moreover we have tested our sensors to different analytes: Ethanol, H_2, and CO. The obtained gas sensor responses are compared to those obtained from WO3 sensors fabricated by hot wall reactor (see Fig. 4 and 5). The optimal operating temperature for WO_3 NN sensing layers deposited using a hot wall reactor is 250 °C and 300 °C for WO_3 NN sensing layer synthetized by a cold wall reactor. Compared to WO_3 NN prepared by hot wall reactor [3], we can see that these new sensors (cold wall reactor) have good responses with nice stability; reproducibility and very fast detection of analytes (see Fig. 6).

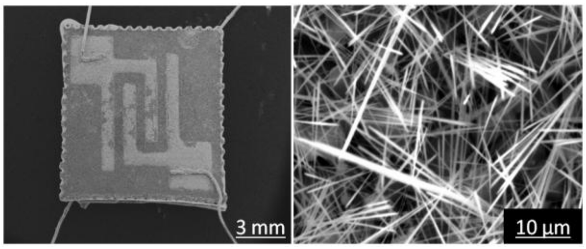

Fig. 3: SEM image of the obtained WO_3 nanoneedles using cold wall reactor.

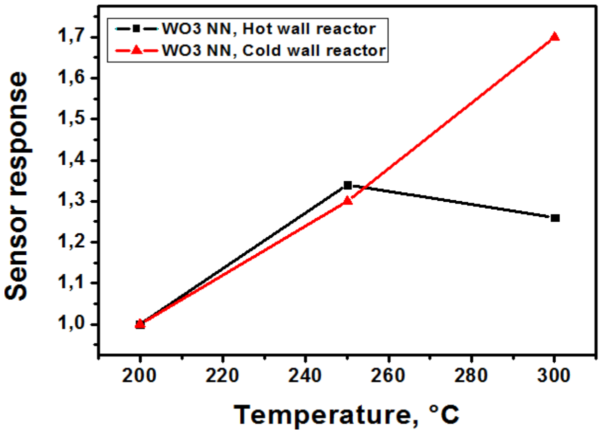

Fig.4: Sensing characteristics of WO_3 NN layers deposited by hot wall and cold wall reactor respectively, towards 10 ppm of ethanol as a function of temperature. X-axis (temperature in ºC) Y-axis (sensor response Rair/Rgas)

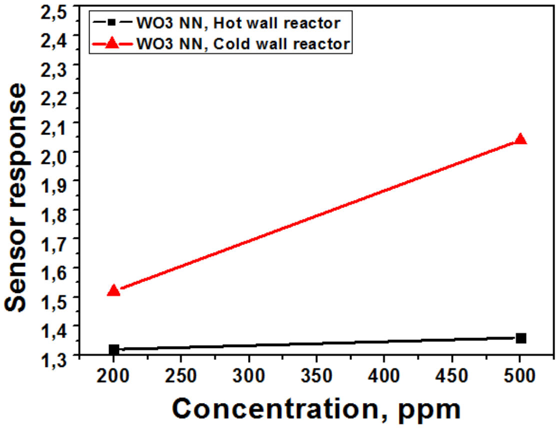

Fig.5: sensors responses to 200 ppm and 500 ppm of H2.

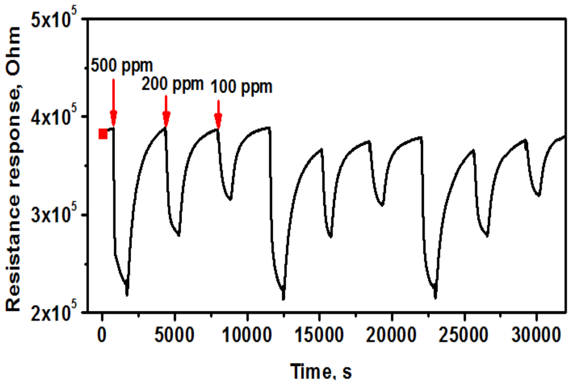

Fig.6: sensor responses of WO_3 NN layer deposited by cold wall reactor toward CO using three consecutives concentrations: 100, 200, and 500 ppm.

References

[1] F. Annanouch, “CO and H_2 Sensing with CVD Grown Tungsten Oxide Nanoneedles Decorate with Au, Pt or Cu Nanoparticles”, Procedia Engineering, vol.47, p. 904-907, 2012.

[2] S. Vallejos, “Single Step Deposition of Au and Pt Nanoparticle Functionalised Tungsten Oxide Nanoneedles Synthesised *via* Aerosol Assisted CVD, and use for Fabrication of Selective Gas Microsensor Arrays”, Adv.Funct.Mater., vol. 23, nr. 10, p. 1313-1322, 2013.

Functionnalization and decoration of MWCNT for resistive gas sensing applications

P. Clément[1], E. Llobet[1], H. Debéda[2]
[1]*MINOS-EMaS, Univeristat Rovira i Virgili, Tarragona, Spain*
[2]*IMS, Université de Bordeaux 1, Bordeaux, France*

Pierrick Clément, Departament d'Enginyeria Electrònica, Elèctrica i Automàtica, Universitat Rovira i Virgili
Avinguda dels Països Catalans, 26 Campus Sescelades, 43007 TARRAGONA (Spain)
Tel. +34 977 256 572, e-mail: pierrick.clement@urv.cat

Abstract

Multiwalled carbon nanotubes were functionalized and decorated with metal nanoparticles by employing an RF sputtering machine. First, CNTs were functionalized in oxygen + argon plasma and then decorated with Au, Pt. The size and density of the metal nanoparticles on the nanotube surface could be controlled by the process parameters such as power, pressure and deposition time. Structure morphology and chemical composition of the different hybrid materials were characterized by means of TEM and EDX. EDX reveals the presence of oxygen species grafted to CNTs functionalized in oxygen + argon plasma and TEM shows that the average diameter of nanoparticles can be as low as 2 nm. The gas sensing properties of these materials have been studied in a new chamber gas sensing whose the geometry has been optimised with a simulation by COMSOL multiphysics software.

1. Introduction

In the present work, we introduce a method based on RF sputtering to achieve a highly stable grafting of metal nanoparticles of small diameter to CNT sidewalls. At first, as-grown CNTs, provided from Nanocyl S.L and produced by CVD, were diluted in dimethylformamide (DMF), and then the solution agitated in ultra-sonic bath at room temperature. After that, the sample was kept several minutes out of the bath to let precipitate the agglomerated CNTs which permit the use of the part of solution that contain the isolated CNTs. This later was airbrushed over alumina substrate. The as deposited MWCNT on alumina substrate were put inside the sputtering chamber (Sputtering ATC Orion 8- HV-AJA International machine) and functionalized in an RF oxygen + argon plasma (figure.2). The objective was to clean CNTs from amorphous carbon and to create reactive sites (i.e. oxygenated vacancies) in which metal nanoparticles can nucleate. Treated CNTs were decorated with Pt, Rh and Pd.

2. Experimental setup

In the present work, we introduce a method based on RF sputtering to achieve a highly stable grafting of metal nanoparticles of small diameter to CNT sidewalls. At first, as-grown CNTs, provided from Nanocyl S.L and produced by CVD, were diluted in dimethylformamide (DMF), and then the solution agitated in ultra-sonic bath at room temperature. After that, the sample was kept several minutes out of the bath to let precipitate the agglomerated CNTs which permit the use of the part of solution that contain the isolated CNTs. This later was airbrushed over alumina substrate (figure.1). The as deposited MWCNT on alumina substrate were put inside the sputtering chamber (Sputtering ATC Orion 8- HV-AJA International machine) and functionalized in an RF oxygen + argon plasma (fig.1). The objective was to clean CNTs from amorphous carbon and to create reactive sites (i.e. oxygenated vacancies) in which metal nanoparticles can nucleate [1].

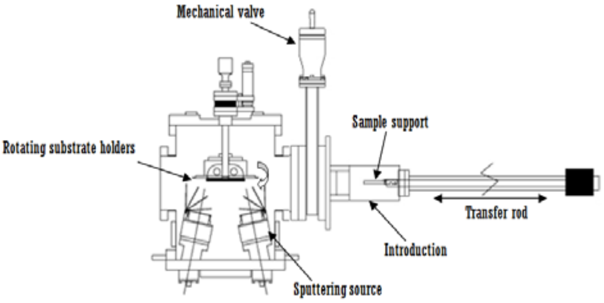

Fig.1. Schema of a sputtering chamber

Treated CNTs were decorated with Au and Pt. Treatment and metal decoration parameters were varied in order to study their effect on the percentage of oxygen grafted to nanotubes and also on the size, distribution and quantity of metal nanoparticles attached to CNT. In order to increase the sensors responsiveness (signal noise and time detection) a new room sensor has been designed doing a simulation using COMSOL multiphysics. Naviers-Stokes equation (Equation 1.) has been used in laminar flow for a description of the velocity of the fluid at a given point in space and time with statement of the conservation of volume (incompressible assumption).

$$\frac{\partial \vec{v}}{\partial t} + \left(\vec{v} \cdot \vec{\nabla}\right) \vec{v} = -\frac{1}{\rho}\vec{\nabla} p + \nu \nabla^2 \vec{v} + \vec{f}$$

Equation.1. Naviers-Stokes equation in laminar flow

The aim here is to limit turbulence of the gas flow avoiding geometric constraints and everything in a confined space for a faster response.

3. Morphological and compositional studies

Scanning electron microscopy and transmission electron microscopy have been used to investigate the morphology of the different nanostructures of decorated MWCNT. Fig.2 shows the SEM image of spray coated carbon nanotubes. It is shown that the density of MWCNT is high meaning that there is a very important active surface but with an irregular uniformity.

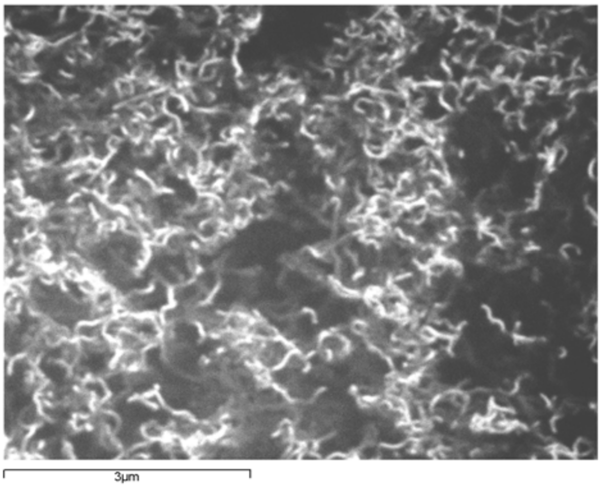

Fig.2. SEM image of spray coated MWCNT.

The deposition of thin layer allows a good and homogeneous fictionalization and metal decoration. From Fig.3, we can see well dispersed metal nanoparticles with a very small diameter in the range of 1 to 2 nm. The presence of oxygen species was confirmed by EDX analysis

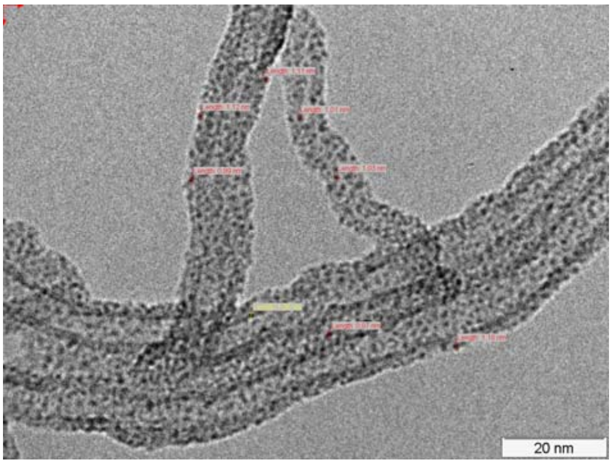

Fig.3. TEM image of Rh decorated oxygen plasma functionalized MWCNT

To identify and confirm the different elements associated to the morphology, we have used EDX-analysis. Table.1 show that EDX confirming the presence of oxygen species grafted to the CNTs.

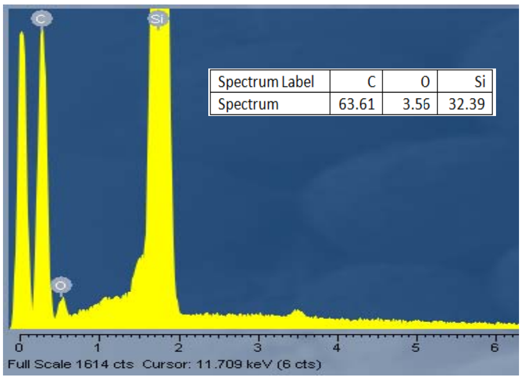

Spectrum Label	C	O	Si
Spectrum	63.61	3.56	32.39

Table.1. EDX analysis and the atomic percentage of oxygen functionalized MWCNT

4. Gas sensing analysis

Herein, we have studied the sensing property of different nanomaterials for benzene. Here is presented in Fig.4. the detection with Pt, Rh, Pd and O-MWNCT active layer which give a good sensitivity at room temperature without heating for the desorption step.

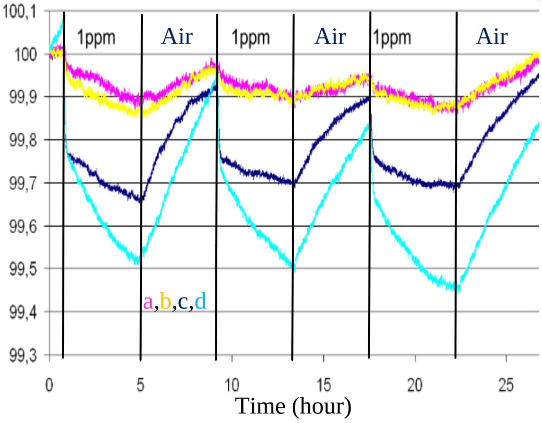

Fig.2. Response towards benzene at room temperature of gas sensors based on a) Pt-O-MWCNT, b) Rh-O-MWCNT, c) Pd-MWCNT, d) O-MWCNT.

5. Conclusion

Using RF sputtering deposition method, very small and stable metal nanoclusters were deposited onto MWCNTs. The test of these hybrid materials with benzene at room temperature reveals that O-MWCNTs based sensor show a higher sensitivity than decorated with metal nanoparticles. These results are very promising for getting more sensitive and selective gas sensors.

References

[1] R. Ionescu, E. H. E., E. Sotter, E. llobet, X. Vilanova, X. Correig, A Felten, C. Bittencourt, G. Van Lier, J.-C. Charlier, J.J. Pireaux "Oxygen functionalisation of MWCNT and their use as gaz sensitive thick-film layers2, *Sensors and Actuators B 113*, pp. 36-46, 2006

Determination of Optimized Fabrication Conditions for Optical Waveguides on Silicon and Glass Substrates

Pinkie Jacob Eravuchira, Josep Ferré-Borrull. Eduard Llobet and Francesc Díaz

Engineering of Materials and Micro/NanoSystems, University Rovira i Virgili,
Avinguda Paisos Catalans26, 43007, Tarragona, Spain
Tel. +34977256571, pinkie.jacob@urv.cat

Abstract

Optical biosensors are one of the powerful tools for the analysis of biological, and biochemical materials. The advantages such as high sensitivity, label-free technique, and fast response time, possibility of in-situ measurement make optical sensors a prominent tool for the analysis of biological-related molecules. Using photo lithography we have fabricated SU-8 optical waveguides on silicon wafers, and glass slides. The fabricated SU-8 waveguides will be used as a tool for the detection and analysis of biological molecules, and biochemical solutions.

1. Introduction

The growing demand for rapid, compact and selective bio detection techniques increases the interest in study of biosensors. Surface Plasmon resonance interferometer, reflectometric interference spectroscopy, optical ring resonators, planar waveguides, and Mach-Zehnder interferometer are some of the widely used label-free optical sensor [1, 2]. The advantages such as high sensitive, low detection limit, specificity, and miniaturized size makes evanescent based bio sensors a promising tool for the detection of biochemical, biological and gaseous samples [3, 4]. In an optical waveguide, due to the refractive index contrast between the core and the cladding, the light incident above critical angle undergoes a total internal reflection, and the interaction between the evanescent field of the propagating light and the analyte on the sensing arm produces a phase shift in the output light.

In this study, we use photolithography to fabricate SU-8 waveguides on oxidized silicon wafers and on glass slides. Detailed study to find the optimum parameters for the fabrication of SU-8 waveguides are explained below.

2. Materials Used

We have used silicon wafers, and microscopic glass slides as the substrates for the waveguides. A cladding layer with lower refractive index than the core will help to propagate light through the waveguide core by total internal reflection. In our studies, oxidized Silicon (n = 1.46) wafers, and glass (n = 1.52) act as a lower cladding material. SU-8 acts as a core, and it can be deposited on the substrates using spin coating. SU-8 is an epoxy based negative photoresist, which is thermally, and chemically stable, and has a refractive index of 1.58 at 633nm.

3. Sample Fabrication

We use photolithographic technique to transfer waveguide designs from a chromium mask to the substrate coated with a negative photoresist, SU-8. Prior to the photolithography which was done using mask aligner (MG 1410 from Karl Suss), the photoresist was spun coated on the glass and silicon substrates. Both the soft bake and post exposure bake were done on a hotplate. Besides, using laser lithography (DWL 66FS from Heidelberg) a chromium mask with desired patterns was fabricated in the URV clean room.

Initially the silicon wafers were cleaned and oxidized by thermal oxidation. This was done to obtain a lower cladding layer (SiO_2) with a low refractive index compared to the core (SU-8), and to provide the surface passivation. The oxidation was performed using a tubular furnace at a temperature of 1100 degree Celsius for 10 hours with a homogeneous flow of synthetic air. The dry thermal oxidation resulted in the formation of an oxide layer of few micrometers (approximately < 0.3μm) on the Si wafers

4. Determination of Optimal Fabrication Conditions

The steps involved in the fabrication of waveguides on substrates are, i) spin coating, ii) soft bake, iii) exposure, iv) post-exposure bake, and v) developing.

The first step was to find the relation between spin coating speed and the thickness of SU-8 on both glass and SiO_2 substrates. In order to obtain waveguides of various thicknesses, commercially purchased SU-8 was spun coated with various rounds per minute (rpm). The

SEM results show that the thickness of SU-8 can vary from 7 µm to 3.40 µm by controlling the spin speed (rpm = 1000-8000). Graph below represents the relation between the spin speed and the thickness (µm) of SU-8.

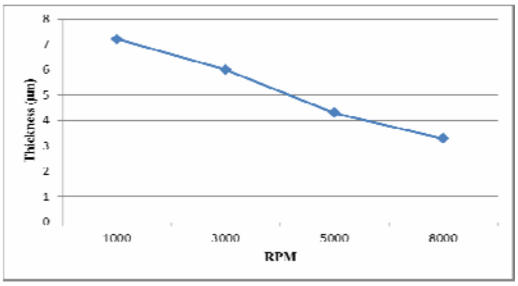

Next step was to find the optimum exposure time. Exposure time is a critical parameter to be considered in order to obtain the desired dimensions for the waveguide structure. The exposure was done using a mask aligner (MG 1410 from Karl Suss) which has an Hg lamp with a wavelength ranging 365-400nm, and a power of 350W. Chromium masks with desired designs were used to transfer the pattern on the substrates using photolithography. Initially a set of tests were performed using various exposure time, ranging from 2 -30secs. The exposed samples were developed, and the results show that the optimum exposure time for SiO_2 substrate is 5secs, and that for glass is 20secs. The exposure time depends on the type and thickness of photoresist, and the wattage of the UV lamb we use.

Other parameters that have to be considered are the temperature and time of soft bake and post exposure bake. In order to find the conditions for the soft bake, post exposure bake, a couple of tests with various temperatures ranging from 65-95 degree C for 2-8 min. were performed. The results show that the best temperature and time for the soft bake and post exposure bake for Silicon wafer is 95^oC degree C for 4 min., and for glass it is 95^oC for 8 min. Below these time and temperature, SU-8 has a very poor adhesion to the corresponding substrates.

5. Observations

The optical waveguides that was produced in the clean room were observed under ESEM and SEM. Figure 1 depicts a waveguides (width=11µm) that we have fabricated using the optimized exposure time, and temperature and time of soft bake and post exposure bake, as explained above. The results show that during photolithography, the magnitude of the structures increases by 2-3µm, than that of the pattern on chromium mask. However, this increase in dimension was observed to be repeating in all the structures.

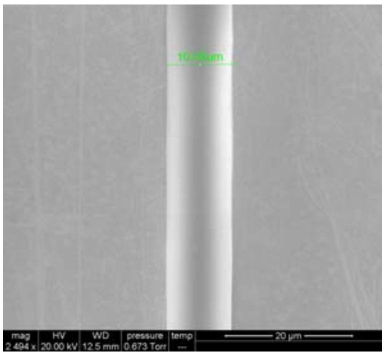

Figure 1: waveguides with a width of 11µm

Besides measuring the width, we have examined a diced piece of wafer in order to check the cross section of the waveguides; the SEM image is shown below (fig 2).

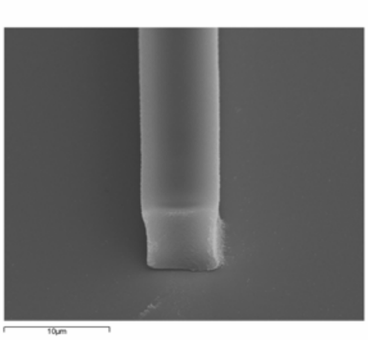

Figure 2: Cross section of a waveguide

6. Conclusion and Future work

We have obtained the optimized parameters for the fabrication of SU-8 waveguides on silicon wafer and microscopic glass slides.

As a further work, the obtained waveguides will be optically characterized and will be used for the detection of various biological samples and biochemical solutions.

References

[1] M. N. Velasco- Garcia, Optical biosensors for probing at the cellular level: A review of recent progress and future prospects, Cell and Development Biology, 20, 27-33,2009.

[2] X. Fan, I. M. White, S. I. Shopova, H. Zhu, J. D. Suter, and Y. Sun, Sensitive optical biosensors for unlabeled targets: A review, Analytica Chimica Acta, 620, 8-26, 2008.

[3] D.H. Luo, R.A. Levy, Y.F. Hor, J.F. federici, and R.M. Pafchek, An integrated photonic sensor for in situ monitoring of hazardous organics, Sensors and Actuators B, 92, 121-126, 2003.

[4] J. Hong, J. S. Choi, G. Han, J. K. Kang, C. Kim, T. S. Kim, and D. S. Yoon, A Mach-Zehnder interferometer based on silicon oxides for biosensor applications, Analytica Chimica Acta, 573, 97-103, 2006.

Synthesis of different nanostructured metal-oxide materials for gas sensing and photocatalytic applications

S. Roso[a, b], A. Urakawa[b], E. Llobet[a]

[a] Minos-Emas. University Rovira I virgili. Avda. Països Catalans 26, 43007 Tarragona, Spain
[b] Institute of Chemical Research of Catalonia (ICIQ), Avda. Països Catalans 16, 43007 Tarragona, Spain

Abstract

In the present work we are currently building two reactors in which we are going to produce a wide range of nanostructured metal oxide materials such as WO_3, TiO_2, ZnO and so on. These nanostructures will be grown using the aerosol-assisted chemical vapor deposition method (AA-CVD), which has some key advantadges compared to other conventional CVD processes. Then, the nanostructures will be used for different applications, for instance gas sensing properties and photocatalytic applications.

1. Introduction

The reduced size of nanostructures like (1D) nanowires (NWs), gives us new mechanical, chemical, electrical and optical properties due to its large surface to volume ratio. The key goal of nanostructure research is to control structure, which opens the door to new structure-function relationships. The fundamental advantage of nanostructures is that they offer something different to the bulk material in terms of size and functionality.

Metal oxides have applications in a wide variety of fields, for example, heterogeneous catalysis, and gas sensing. The presence of oxygen vacancies plays an important role in the sensing mechanism of metal oxides.[1] Additionally, low-dimensional metal oxides are often single crystal nanostructures with well defined catalytic properties, which help in gaining insight into the gas sensing mechanisms of these nanomaterials. [2]

In this work, we intend to present the tools with which we are going to develop our work

2. Fundamental theory

The lack of proper volatile precursors and the difficulty in controlling the stochiometry of the deposits are major drawbacks for further applications of conventional CVD techniques. For that reason, as a variant of usual CVD, the aerosol-assisted (AA-CVD) method uses aerosol droplets to transport the precursor with the aid of a reactive or an inert carrier gas. In AA-CVD, chemical precursors must not be necessarily volatile, but merely soluble in any solvent from which the aerosol is generated. AA-CVD based processes have major advantages compared to other CVD techniques such as wider choice of precursors, simplification of the delivery and vaporization of precursors, high deposition rate, more flexible reaction environment and simplification of the synthesis of multicomponent products with precise stochiometric control.[3]

As a result of the aerosol transport and the associated CVD, AA-CVD can combine the benefits of both CVD method and spay-pyrolysis processes.

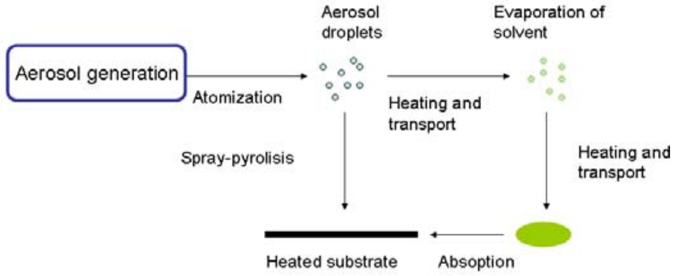

Fig 1. Scheme of the AA-CVD technique.for deposition of nanostructures.

As we can see from Fig.1, AA_CVD involves the atomization of the liquid precursor solution into fine sub-micrometer sized aerosol droplets. These droplets are then driven into a heated reaction zone where the solvent undergoes rapid evaporation forming the desired precursor at the increased temperature. This procedure can be performes under atmospherc pressure or low pressure.

The liquid chemical precursor is atomized to aerosol droplets prior to being delivered to the heated substrate where it undergoes the reaction. There are three major aerosol generation methods used for AA-CVD, the ultrasonic aerosol generation, pneumatic aerosol generation and the electrostatic aerosol atomization. The ultrasonic aerosol generation is the most common method and the one that we will use. When a hihg frequency electric field is applied to a piezoelectric transducer, it vibrates and instigates the formation of the droplets. The diameter of the droplets is:

$$d = k\left(\frac{2\pi\gamma}{\rho f^2}\right)^{\frac{1}{3}}$$

Ultrasonic generation offers advantages in terms of providing a suitable droplet size for AA-CVD process. The atomized droplet sizes are mainly in the range 1-10µm.

Then, the atomized precursor is transported ito a heated reaction zone where the evaporation of solvent and the vaporization of precursor occur.

Finally, the vaporized precursor is absorbed in the desired heated substrate.

3. Experimental

As mentioned previously, we are currently building two reactors in order to produce the desired nanostructures. On the one hand, we have the reactor shown in Fig 2.

Fig 2. Homemade reactor in which we will produce nanostructures.

This reactor consists of a spiral microheater that can go up to 1000ºC. On top of that heater it will be placed the substrate in which the nanostructures will grow. The input and the output are placed in the cover of the reactor and we will be able to control the flow that is passing through the reactor. The temperature will be measure with a K-type thermocouple and it could be controlled from the outside. This reactor is tought to be used for producing nanostructures for gas sensing applications. The deposited material should have an exceptionally high sensitivity and fast response and recovery upon exposure to different gases.
On the other hand we have the reactor shown on Fig 3.

Fig 3. Commercial furnace in which we will produce nanostructures.

This is a commercial furnace that we turned into an AA-CVD reactor. This furnace can go up to 1200ºC and we placed a quartz tube inside in which we are going to make a mass-production NWs. We intend to have enough material to make photocatalysis experiments. The deposited nanomaterial films should will have a very good catalytic activity and an enhancement of catalytic efficiency can be achieved by doping our material.

4. Conclusions

In this work we have presented the tools with which we are going to produce different kind of nanostructures and we have explained the use that we intend to give them.

References
[1] C. Navío et al. "Gold clusters on WO_3 nanoneedles Brown via AACVD: XPS and TEM Studies" Materials Chemistry and Physics **2012**, 1-5
[2] F. E. Annanouch, et al. "Aerosol Assisted vapour deposition of gas-sensitive nanomaterials". Thin Solid Films **2013**
[3] X. Hou and K. L Choy. "Processing and applications of Aerosol-Assisted Chemical Vapor Deposition" Chem. Vap. Deposition **2006**, 12, 583-596

R2D2: An R package for Comprehensive Chromatrography GCxGC-TOF Compound Detection, Identification and Quantification in Metabolomics

Xavi Domingo and Jesus Brezmes
SIPOMICS. Metabolomics Platform.
DEEEA. Universitat Rovira i Virgili.
Tarragona, Catalonia
Email: xavier.domingo@urv.cat

Alexadre Perera
Centre Recerca en Enginyeria
Biomèdica. Universitat Politècnica de Catalunya.
Barcelona, Catalonia

Metabolomics is the science discipline that studies low molecular weight compounds in biological systems. This novelty approach is in continuous expansion due to its potential contribution to the so-called personalized medicine of the XXI century. While other ”-omics” disciplines such as genomics, transcriptomics or proteomics tell you what may happen on a living organism, metabolomics tells you what actually is happening since it takes account genetic predisposition, differentiaton, external factors such as diet, sport practice and life habits [1]. Registering and the understand of the entire metabolome of a living organism is an ambition task not exempt of difficulties which have to be overcame.

One of metabolomics aims is to compare healthy organisms with metabolomic disease so to find predictive biomarkers, but also to analyze subjects and samples to find out which compounds change their presence or concentration. To study and find compounds in living organisms, or more concretely, human samples, techniques such liquid and gas chromatography are employed. Liquid chromatography and gas chromatography separate the sample compounds while passing through a chromatographic column, but in some cases the compounds do not separate completely and this is when co-elution appears. An instrumental approach to improve the technique is to add a second chromatographic column, and that is how comprehensive double gas chromatography appears (GCxGC-MS). Moreover, a software capable of interpreting this information is also needed. This is why double column gas chromatography is still an uncommon method of analysis in metabolomics. Although it is a very mature technology, there is a lack of GCxGC processing software to analyze complex samples in non-targeted experiments in a very automatic way. Currently, there are three tools for GCxGC-MS data processing: Guineu [2], ChromaA4D [3] and ChromaTOF [4]. They can provide good results, but the results they give cannot be trusted, i.e., identification is not always correct and fails in many cases. Hence, the desired software not only havs to provide a table of suggestions of which compound it has detected, but automatic results that do not need a human chemist to make the final decision of which compound corresponds to each detection.

Moreover, all the existing software is programmed with $C++$ or $Java$. The newest bioinformatics or metabolomics algorithms and software are now being developed in R [5]. This open-source platform has become the de-facto standard in all biological fields, hence, its vital for the new softwares to adapt to such situation. In this work we have developed an R package capable of processing GCxGC-MS data in metabolomics and detecting, quantifying and identifying compounds.

The workflow of the software is shown in 1. The software starts reading the standard format netCDF or XML from the comprehensive machine used. GCxGC-MS can be understood as multiple GC-MS measurements, then, each GCxGC-MS sample is divided in its multiple GC-MS measurements and treated individually, grouping and interpreting the results once all the slices have been processed.

First, a pre-processing step will be carried out, where the data will be filtered with a Gaussian smoothing filter, which acts as a low-pass filter, using a σ in seconds as a parameter instead of a cut-off frequency. The data is also subjected to baseline subtraction and featured according to a certain noise threshold obtained automatically. The software is oriented to non-targeted analysis, i.e., there is no prior information of what compounds can be found and it does not require other samples to compare the data. Hence, a Principal Component Analysis [6] will be used as factor analysis. In this step, we will determine how many different compounds exist in the sample, by assuming that compounds have different spectra. Nevertheless, the noise present in samples interfere with obtaining perfect results. After the PCA analysis has been applied, Multivariate Curve Resolution (MCR-ALS) [7,8,9] is used to deconvolve peaks that contain multiple compounds. To initialize the method, we will provide MCR-ALS with the number of factors or components and their position in retention time, together with an initial estimation of their spectra also provided by the PCA. We can observe the results in 2. Finally, comparison of the resulting spectra obtained

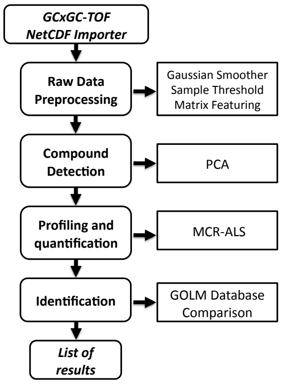

Fig. 1. Main workflow of R2D2 GCxGC processing software.

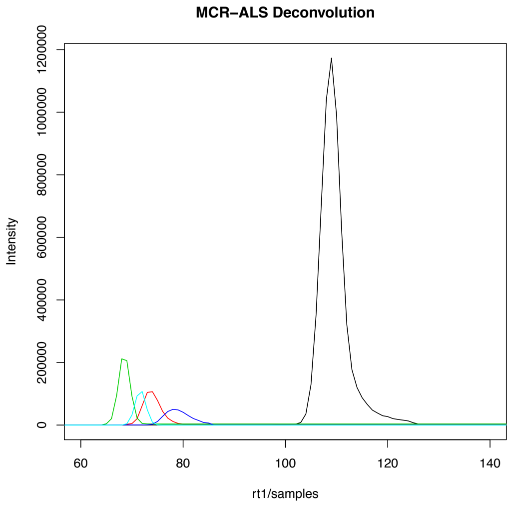

Fig. 2. MCR-ALS deconvolution result. We can appreciate how MCR-ALS succeds in deconvolving two peaks around tr2 = 110.

against the GOLM database [10] is carried out.

To validate our method, we performed a full analysis of three samples: a blank sample, a sample containing 50 known standards, and serum pool sample. All three samples were analyzed with both ChromaTOF and R2D2, and we compared the detection of thirteen fatty acid methyl esters (FAMEs) present in all of them. Results can be seen in table 1 and 2. R2D2 performs a better identification, which was our main goal. Nevertheless, a dedicated version of MCR-ALS for gas chromatography or better noise reduction techniques would be desirable to improve the results of R2D2.

FAME	**Blank**	**Standard**	**Serum**
$C1 - Octanoate$	✓	✓	✓
$C2 - Nonanoate$	✓	✓	✓
$C3 - Decanoate$	✓	✓	✓
$C4 - Dodecanoate$	✓	×	×
$C5 - Tetradecanoate$	✓	×	×
$C6 - Hexadecanoate$	✓	✓	N.I
$C7 - Octadecanoate$	×	×	×
$C8 - Eicosanoate$	×	×	×
$C9 - Docosanoate$	✓	✓	✓
$C10 - Tetracosanoate$	×	×	×
$C11 - Hexacosanoate$	×	×	×
$C12 - Octacosanoate$	×	×	×
$C13 - Triacontanoate$	N.I	N.I	N.I

TABLE I. RESULTS SHOWING IDENTIFICATION OF R2D2 IN THE THREE SAMPLES. THE STICK INDICATES THE COMPOUNDS CORRECTLY IDENTIFIED. THE CROSS INDICATES THE DETECTED COMPOUNDS THAT WERE CONFUSED WITH ANOTHER SIMILAR FATTY ACID. N.I STANDS FOR $not\ identified$, AND INDICATES WHICH COMPOUNDS WERE DETECTED BUT WERE NOT IDENTIFIED AS ANY FATTY ACID.

Software	**C1**	**C2**	**C3**	**C4**	**C5**	**C6**
$R2D2$	✓	✓	✓	✓	✓	✓
$ChromaTOF$	✓	✓	✓	×	×	×
Software	**C7**	**C8**	**C9**	**C10**	**C11**	**C12**
$R2D2$	×	×	✓	×	×	×
$ChromaTOF$	×	×	×	×	×	×

TABLE II. TABLE COMPARING THE IDENTIFICATION OF R2D2 AGAINTS CHROMATOF. THE STICK INDICATE A CORRECT IDENTIFICATION, IN OTHER WORDS, THE NAME OF THE COMPOUND FOUND IS CORRECT. C-13 IS NOT CONSIDERED AS IS NOT CORRECTLY IDENTIFIYED BY R2D2

REFERENCES

[1] Schmidt., C.W. (2004) Metabolomics: What is Happening Downstream of DNA, *Environmental Health Perspectives*, **Vol. 112 - No. 7**, 410-415.

[2] Castillo S., Mattila I., Miettinen J., Oresic M., Hyotylainen (2011) Data Analysis Tool for comprehensive two-dimensional gas chromatography/time-of-flight mass spectrometry, *Analytical Chemistry*, **83**, 3058-3067.

[3] Hoffman N., Stoye J. (2009) ChromA: signal-based retention time alignment for chromatography - mass spectrometry data, *Bioinformatics*, **Vol. 25 no.16**, 2080-2081.

[4] LECO, ChromaTOF ®, *St. Joseph, MI (USA)*. http://www.leco.com.

[5] R Core Team (2012) R: A language and environment for statistical computing, *R Foundation for Statistical Computing, Vienna, Austria*, **ISBN 3-900051-07-0**, URL http://www.R-project.org/.

[6] Wold S. (1987) Principal component analysis, *Chemometrics and Intelligent Laboratory Systems*, **2**, 37-52.

[7] Tauler, R. (1995) Multivariate curve resolution applied to second order data, *Chemometrics and Intelligent Laboratory Systems*, **30**, 133-146.

[8] Tauler, R., Smilde, A., Kowalski, B. (1995) Selectivity, local rank, three-way data analysis and ambiguity in multivariate curve resolution *Journal of Chemometrics*, **9**, 31-58.

[9] Garrido M., Rius F.X., Larrechi M.S. (2008) Multivariate curve resolution - alternating least squares (MCR-ALS) applied to spectroscopic data from monitoring chemical reactions processes, *Analytical and Bioanalytical Chemistry*, **390**, 2059-2066.

[10] Kopka, J., Schauer, N., Krueger, S., Birkemeyer, C., Usadel, B., Bergmuller, E., Dormann, P., Weckwerth, W., Gibon, Y., Stitt, M., Willmitzer, L., Fernie, A.R. and Steinhauser, D. (2005) GMD@CSB.DB: the Golm Metabolome Database, *Bioinformatics*, **21**, 1635-1638.

Enhanced DC Bus Energy Management Strategies for Electric Vehicle Drives

L. Albiol-Tendillo, E.Vidal-Idiarte, J. Maixé-Altés

Departament d'Enginyeria Electrònica, Elèctrica i Automàtica.
Universitat Rovira i Virgili.
Tarragona, España.

Abstract

This article compares three different energy management strategies for the electric vehicle drive. These strategies are described and simulated for a specific design of a DC/DC converter and an inverter.

1. Introduction

The typical architecture of an electric vehicle traction system generally consists of a battery, a DC/DC bidirectional converter, an inverter and a motor [1]. The traction motor power may be comprised between 60 and 100 kW. Consequently, the DC/DC converter is comprised, in fact, of several converters with lower power rating, working in parallel.

The cascade connection of power conversion structures, such as the converter plus inverter set, has enabled the application of specific techniques to obtain more efficient power conversion [2]. In this article, three different energy management strategies are analysed –time-sharing, the standard strategy and a two-level DC bus strategy– for electric vehicle drives.

2. Standard Energy Management

The standard traction system of an electric vehicle has a high-power DC/DC converter that boosts battery voltage to a fixed DC bus voltage. The converter has to be bidirectional in order to allow regenerative braking, and in this article a bidirectional boost converter with output filter has been considered. The DC bus supplies a three phase converter, which is connected to the motor.

The waveforms obtained with this standard energy management are shown in Fig.1. It can be observed that the DC bus voltage is constant, and the inverter generates the AC voltage waveform required by the motor.

3. Two-Level DC bus Energy Management

The two-level DC bus energy management strategy proposed in this paper is based on the fact that the high-power DC/DC converter will be currently implemented by several DC/DC converters with lower power rating in parallel. Designing the traction system in order to have a number of DC/DC converters multiple of the number of phases of the motor, it is possible to supply each inverter leg with a different voltage, as depicted in Fig. 2.

The converter has to be bidirectional, since it has to be capable of charging the battery during regenerative braking. The two-level DC bus energy management strategy consists on having two different possible DC bus voltages: the rated DC bus voltage, and the battery voltage. The desired DC bus voltage value will be the battery voltage in case the inverter needs less than this value, and the rated DC bus voltage otherwise.

When the motor required voltage exceeds the battery voltage the extra diode D3 will not be conducting, and the converter will boost battery voltage to the rated DC bus voltage, since vC0 will be set to the DC bus rated voltage. If the motor required voltage is lower than the battery voltage, the D3 diode will be conducting, and

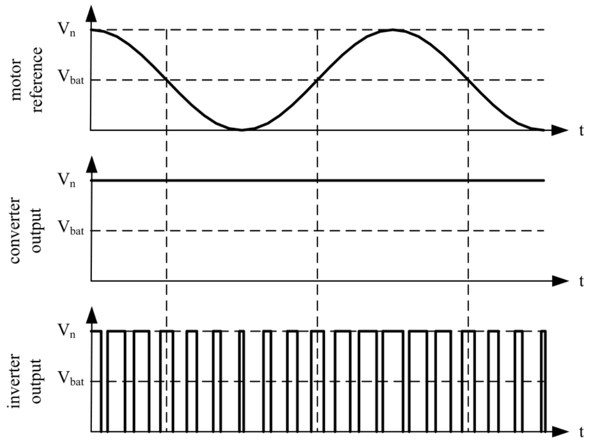

Fig. 1. Motor reference, converter output and inverter output waveforms for the standard energy management strategy.

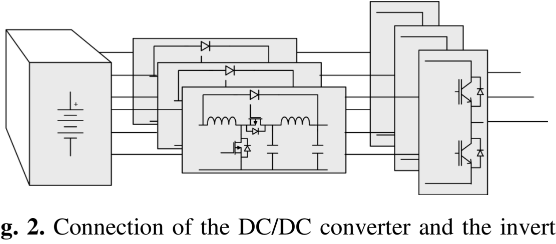

Fig. 2. Connection of the DC/DC converter and the inverter for an electric vehicle traction system in the two-level DC bus and time-sharing energy management strategies.

vC0 will be set to the battery voltage. Consequently, this strategy allows the disconnection of the converter when its use is not necessary, reducing the switching losses, but increasing the conduction losses. Fig. 3 shows the waveforms obtained by applying the two-level DC bus energy management strategy.

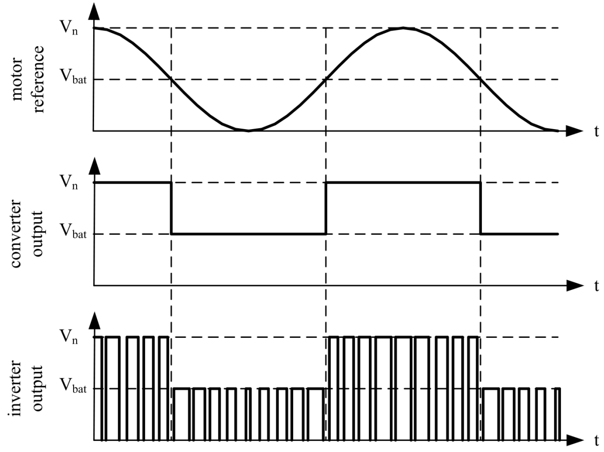

Fig. 3. Motor reference, converter output and inverter output waveforms for the two-level DC bus energy management strategy.

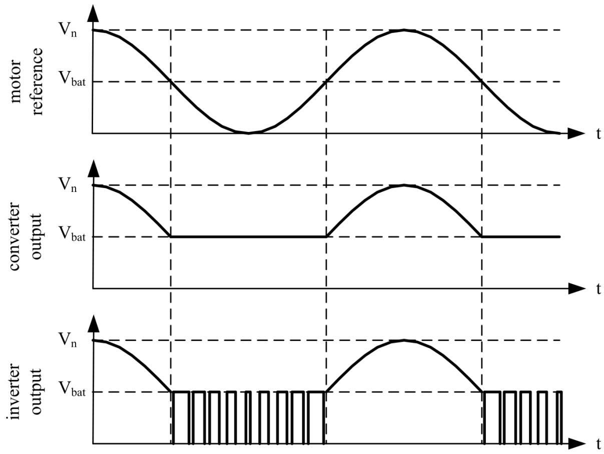

Fig. 4. Motor reference, converter output and inverter output waveforms for the time-sharing energy management strategy.

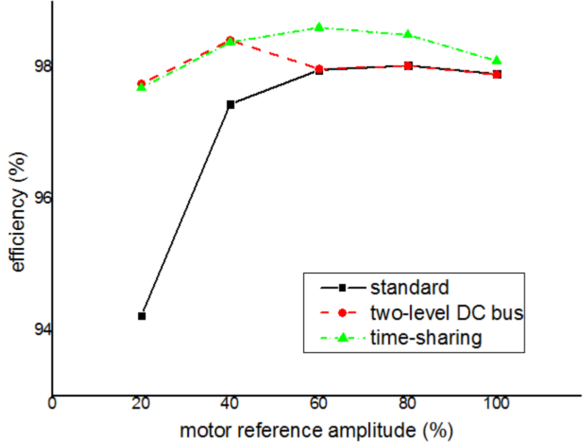

Fig. 5. Efficiency comparison of the energy management strategies for different amplitudes of the motor reference voltage during traction mode operation.

4. Time-Sharing Energy Management

The time-sharing energy management is the adaptation of the time sharing strategy for photovoltaic applications. The time-sharing strategy is based on operating either the DC/DC converter or the inverter, depending on the voltage level demanded by the motor. If the motor requires a voltage level below the battery voltage, the converter is not commutating, and the current flows through the extra diode D3, the same way that in the two-level strategy. Therefore, the DC bus voltage level will be equal to the battery voltage, and the inverter will modulate this voltage in order to provide the waveform requested by the motor. Otherwise, if the motor requires a voltage that exceeds the battery voltage, the inverter does not operate, and the DC/DC converter boosts the battery voltage to the exact demanded voltage level, as it can be appreciated in Fig. 4. Therefore, the DC bus voltage reference vC0 is set to the battery voltage when the converter is not operating, and to the desired motor voltage when it is operating but the inverter is not.

5. Simulation Results

The best efficiency over the whole range of operation is obtained by the standard energy management strategy, as shown in Fig. 5. The other two strategies have almost the same efficiency, but the two-level DC bus efficiency is the worst considering the whole range of operation. However, as the amount of time that the motor is regenerative braking is much reduced in comparison to the traction operation, this efficiency loss is not significant.

6. Conclusions

The efficiency of the three energy management strategies considered in this article has been evaluated. The time-sharing strategy offers the best efficiency, with a substantial improvement of 3.47% over the standard strategy in the most favourable conditions. Moreover, the modularity of the hardware configuration associated with the time-sharing energy management provides the possibility to reconfigure the system after a fault and to reach high power ratings.

References

[1] A. Emadi, L. Young Joo, and K. Rajashekara, "Power Electronics and Motor Drives in Electric, Hybrid Electric, and Plug-In Hybrid Electric Vehicles," Industrial Electronics, IEEE Transactions on, vol. 55, pp. 2237-2245, 2008.

[2] K. Ogura, T. Nishida, E. Hiraki, M. Nakaoka, and S. Nagai, "Time-sharing boost chopper cascaded dual mode single-phase sinewave inverter for solar photovoltaic power generation system," in Power Electronics Specialists Conference, 2004. PESC 04. 2004 IEEE 35th Annual, 2004, pp. 4763-4767 Vol.6.

Hysteresis Modulation in Sliding Mode Control for HBLEDs

M. Bodetto, A. El Aroudi, A. Cid-Pastor, and Luis Martínez-Salamero.
Department of Electronics, Electrical Engineering and Automatic Control
Universidad Rovira i Virgili. Tarragona, Tarragona , SPAIN
E-mails: {mirko.bodetto, angel.cid, abdelali. elaroudi, luis.martinez}@urv.cat

Abstract- **Despite their high cost, High-Brightness LEDs (HBLEDs) have high competitiveness in the market, due to the high efficiency that can be achieved. This paper proposes the design and implementation of a power supply based on a Power Factor Correction (PFC). It consists in a Cuk converter controlled by means of a sliding-mode regulation loop that imposes a resistive characteristic at its input port. A variable hysteresis window is used to avoiding the distortion near the zero crossing of the input current. The proposed approach has been validated by means of PSIM simulations.**

1. Introduction

Thanks to the progress of solid-state lighting devices, LEDs, and HBLEDs have already surpassed the levels of light intensity and lifetime of conventional light sources. The main obstacles that arise in this new technology mainly concern two main drawbacks: the adaptation power stage, and the relationship between temperature, luminous flux, and current. In [1, 2] details of the problems caused by the temperature and the consequent effect on performance and service life of the LEDs are presented. In most of the research works such as [3, 4], it is aimed to improve the power conversion stage. In [5], the SEPIC converter has been proposed to work as a high efficiency adaptation stage for an HBLED load. This was done by making this converter to work as a Power Factor Correction (PFC) circuit. This behaviour was imposed by using a Sliding Mode Control (SMC) [6, 7] by which the the system is imposed to behave as a Loss Free Resistor (LFR). The problem with using a SMC in switching converters is that in an implementation-aware design, a hysteresis comparator must be used to limit the switching frequency to an acceptable range. However, with a fixed hysteresis width, the switching frequency is variable and reaches very low values near the zero crossing of the input voltage. This decrease in the switching frequency provoke that the system works in the Discontinuous Conduction Mode (DCM) which results in a loss of the sliding regime and, as a consequence of this, a harmful harmonic distortion takes place as it is depicted in Fig. 1.

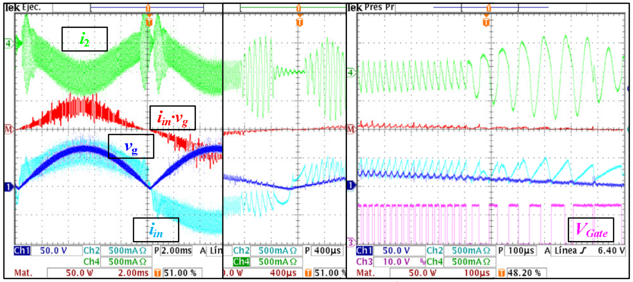

Fig. 1 Loss of sliding mode regime of the Ćuk converter near the zero crossing of the inductor current.

To mitigate this problem, has been proposed a time varying hysteresis width which is made enough small as the input voltage approaches zero.

The rest of the study is organized as follows: a system description and stability analysis are presented in Section II. Simulations results are reported in Section III. Finally the conclusions and future research lines are summarized in Section IV.

2. System Description And Stability Analysis.

Figure 2 shows a circuit diagram of the system under study. It consists of a Ćuk converter under a SMC and supplying a group of HBLEDs. The sliding surface is selected such that the input current i_1 is proportional to the input voltage v_g. Thus the switching surface is described (1) where g=1/r.

$$s(x) := i_1 - g \cdot v_g = 0 \qquad (1)$$

To simplify the design process, let us consider that the outer current loop is open, i.e. the conductance G, which is a reference that is provided by the output current loop, is considered constant. However, numerical simulations, presented later, this feedback loop will be taken into account.

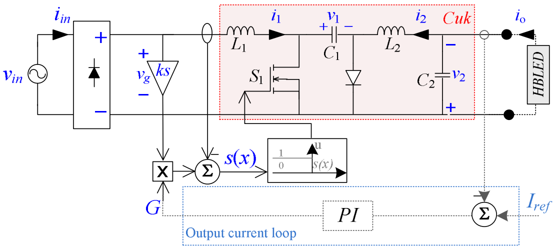

Fig. 2 Block diagram of a sliding mode control applied to a Ćuk converter to work as an LFR.

The system works in Continuous Conduction Mode (CCM). In this operation mode, the system switches between two different topologies that can be described by a system of differential equations corresponding to the two states of the MOSFET S$_1$ ON ($u(t)$=1) or OFF ($u(t)$=0). The system state equations are expressed as follows

$$\dot{x} = A_1 x + B_1 \quad \text{for} \quad u = 1 \qquad (2)$$

$$\dot{x} = A_2 x + B_2 \quad \text{for } u = 0 \qquad (3)$$

where $x = (i_1, i_2, v_1, v_2)^T$ is the vector of state variables. The HBLED is modelled as follows: $V_{LED} = (V_F + Io\ rd)$; where rd is the dynamic resistance and V_F is the forward voltage drop.

The matrices A_i, and vectors B_i are state matrices and input vectors of the Ćuk converter. Mathematical analysis is performed in the same way as in [5]. The equilibrium point results from the intersection of ideal dynamics sliding curve, and are detailed below:

$$Xss = \left[v_g \cdot ks \cdot G, \frac{v_g^2 \cdot ks \cdot G}{V_2}, (V_2 + v_g), V_2 \right] \qquad (4)$$

where $V_2 = \frac{1}{2}\left(V_F + \sqrt{V_F^2 + 4 v_g^2 rd \cdot ks \cdot G} \right)$

Applying the Routh-Hurwitz criterion, one can determine that the system is locally stable for all values of v_g>0 and therefore the harmonic distortion observed above is not attributed to instability but rather to a loss of sliding mode regime due to DCM caused of a decrease in the switching frequency.

3. Numerical Simulations

Numerical simulations have been performed using PSIM Package. To create the equivalent control, a hysteretic comparator has been used with an analogue multiplier as shown in Fig. 3.

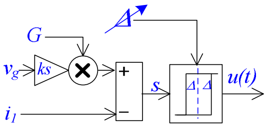

Fig. 3 Block diagram of the varying hysteresis width control.

To alleviate the problem of distortion near the zero crossing, has been modulating the hysteresis width: when v_g approaches zero also Δ tends to zero. This implies an increase of the switching frequency rather than its decrease as is the case in Fig. 1. the corresponding simulation results obtained are shown in Fig. 4.

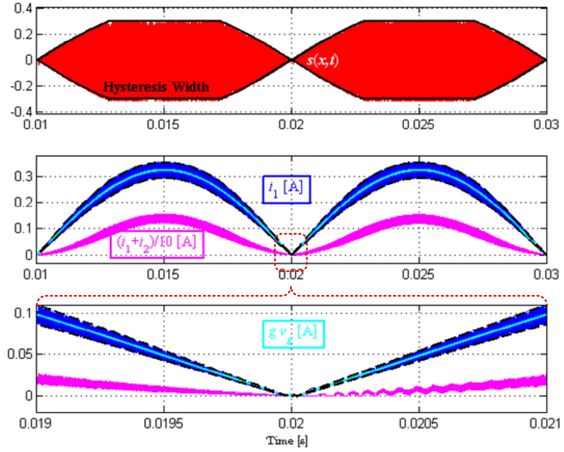

Fig. 4 Effects of the SMC with varying the hysteresis width Δ.

If the system is controlled with a variable hysteresis window as shown in Fig. 3, one can observe that the input current ripple is decreased near the zero crossings. This is due to the increased value of the switching frequency caused by a decrease of the hysteresis width in this region. In this way obtaining an improvement in the PF and thus the system behaves as a perfect LFR.

This increased frequency at critical points, where this current tends to zero, not only enables better PF, but also allows a larger range of control over the current flowing through the HBLEDs. Additionally, these features are also observed when a feedback is used to control this current, so as to be able to control the brightness of the HBLEDs. The results with a closed output current loop are shown in Fig. 5 where it can be observed that the load current tracks the reference current (I_{ref}) while the input variables maintain the proportionality between the input variables imposed by the SMC. Fig. 5a,b (magenta graphic) corresponds to the small-signal model with continuous input voltage (V_g) and input line voltage ($v_g(t)$) respectively.

4. Conclusions

The harmonic distortion near zero crossing can cause harmful effects in PFC converters. In this study, we have proposed a method to reduce this distortion for a SMC Ćuk converter operating in CCM for lighting applications. Have been considered a time varying hysteresis width which is made enough small as the input voltage approaches zero. With this methods, the proportionality of the input variables is satisfied with a simple design resulting in a very low distortion control of the input current. Numerical simulations confirm the correct operation of the proposed techniques and verify the robustness of the system for HBLEDs applications.

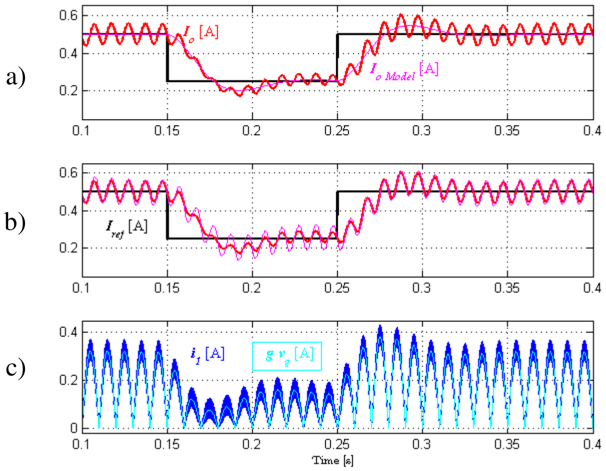

Fig. 5 Waveforms of the input and the output currents with a closed output current loop.

References

[1] S. Y. Hui and Y. X. Qin, "A General Photo-Electro-Thermal Theory for Light Emitting Diode (LED) Systems," *Power Electronics, IEEE Transactions on,* vol. 24, pp. 1967-1976, 2009.

[2] G. Sauerlander, D. Hente, H. Radermacher, E. Waffenschmidt, and J. Jacobs, "Driver Electronics for LEDs," in *Industry Applications Conference, 2006. 41st IAS Annual Meeting. Conference Record of the 2006 IEEE*, 2006, pp. 2621-2626.

[3] Z. Kening, Z. Jian Guo, S. Yuvarajan, and W. Da Feng, "Quasi-Active Power Factor Correction Circuit for HB LED Driver," *Power Electronics, IEEE Transactions on,* vol. 23, pp. 1410-1415, 2008.

[4] L. Chi Kwan, L. Sinan, and S. Y. Hui, "A Design Methodology for Smart LED Lighting Systems Powered By Weakly Regulated Renewable Power Grids," *Smart Grid, IEEE Transactions on,* vol. 2, pp. 548-554, 2011.

[5] M. Bodetto, A. Cid-Pastor, L. Martinez-Salamero, and A. El Aroudi, "Design of an LFR based on a SEPIC converter under sliding mode control for HBLEDs applications," in *Circuits and Systems (ISCAS), 2011 IEEE International Symposium on*, 2011, pp. 2901-2904.

[6] H. Sira-Ramirez, "Sliding motions in bilinear switched networks," *Circuits and Systems, IEEE Transactions on,* vol. 34, pp. 919-933, 1987.

[7] L. Martinez-Salamero, J. Calvente, R. Giral, A. Poveda, and E. Fossas, "Analysis of a bidirectional coupled-inductor Ćuk converter operating in sliding mode," *Circuits and Systems I: Fundamental Theory and Applications, IEEE Transactions on,* vol. 45, pp. 355-363, 1998.

Laboratory Testing Guidelines for Ferroresonance Studies

J. A. Corea-Araujo*, F. González-Molina*, J. A. Martínez-Velasco**, J. A. Barrado-Rodrigo*, and L. Guasch-Pesquer*

*Departament d'Enginyeria Electrònica, Elèctrica i Automàtica, Universitat Rovira i Virgili, Spain.

** Departament d'Enginyeria Elèctrica, Universitat Politècnica de Catalunya, Spain.

Abstract

Ferroresonance is one of the most destructive transient phenomena on power systems; ferroresonant overvoltages can cause failures in transformers, cables, and arresters. This complex effect, which involves the association of nonlinear magnetizing inductances and capacitances, may be initiated in many different ways, hindering its representation. This work tries to illustrate a proper guideline for transformer model configuration starting from real data acquisition through routing tests, special tests and finally describing the manner for performing a ferroresonance essay under a controlled environment.

1. Introduction

Ferroresonance is a firmly established term in power systems analysis that has been used to denote oscillating overvoltages that usually appear in scenarios involving a non-linear inductance associated with any capacitance source. In most cases involving ferroresonance, a power system will be driven to a destructive stage causing equipment lost and energy service suspension. During recent years, the study of the ferroresonance phenomenon has been significantly increased within the international researchers. The study has been divided into four clear lines defined as [1]: (1) practical system case studies, (2) identification methods, (3) development of mitigation approaches, and (4) improvement of analytical techniques and modeling of electromagnetic transients in transformers. This work presents a guideline to venture in the improvement of transformer modeling, showing the conventional and special tests required to configure a transformer model for ferroresonance case studies.

2. Routine tests

Modeling electromechanical components and real events representation involving ferroresonance normally implies having real data from linear and non-linear elements that compose the system under study. Figure 1 shows a typical representation of a three-phase transformer based in the duality theory [2].

The most known set of tests are those called routine test as defined in [3][4]. For liquid-immerse transformers there is up to five tests to perform: (1) Isolation test, (2) Resistance measurement, (3) Ratio test, (4) No-load losses and excitation current (5) Load losses and impedance voltage. For models working under steady state, the routine tests supply sufficient information, however transient analysis is often highly dependent on those non-linear parameters and internal capacitance effects.

3. Special Tests

Whenever a transient phenomenon is intended to be reproduced or analyzed, the model of the transformer should at least have the non linear representation of every leg containing a winding. In ferroresonance cases not only this is needed but also the non linear behavior of every leg and yoke in the core, besides the zero sequence behavior and the internal capacitance values that could be presented between phases and between coils. The amount of tests required in transformers, for a correct representation in computational analysis, is listed as follows: (1) Internal capacitance measurement, (2) Zero sequence impedance, (3) Magnetization curve.
In the field, these tests are considered as special due to its complexity and usually are not required for a transformer installation [3]. In research, are often needed because of the amount of information obtained for optimal computational representation. Figure 2 shows the equivalent circuit for the capacitance measurement test.

4. Ferroresonance Test

Although an actual test for ferroresonance measurement does not exist or is not yet considered by international test routine standards, such IEEE or IEC, it is possible to find within the literature some authors who describe precisely the ferroresonance path and the prone conditions for ferroresonance ignition [5][6]. In these sense, it has been possible to prepare a sort of routines to measure and capture ferroresonance signals in a controlled environment, being these: Energization and de-energization routine, grounded and ungrounded wye connection of external capacitance routine and magnetization routine. Under these conditions it was possible to inquire the effect of the most influential parameters on the global behaviour of ferroresonance phenomenon such capacitance or shifting angle [7]. Figure 3 shows one of the paths used to induce ferroresonance.

5. Case Study

Conceivably, capacitance is one of the two most influential parameters in the occurrence of ferroresonance. In Figure 3, the capacitance value will vary in controlled steps while ferroresonance is induced through the low voltage side of the transformer by the proper commutation of the breakers. Figure 4 shows a quisi-periodic ferroresonance signal measured in the open phase of the low voltage side of a 13.2/0.214 kV, 112.5 kVA, 60 Hz three phase transformer, while performing a de-energization routine and having 30 µF in an external grounded wye capacitance bank. Some internal parameters of the transformer are shown below:

TAP	*High Voltage (Ω)*			*Low Voltage (mΩ)*		
	A	*B*	*C*	*a*	*b*	*c*
2	13.15	12.84	12.75	2.94	2.95	2.95

Table 1. Resistance measurement test

	nF
High- Low	2.4
High - Ground	1.4
Low - Ground	0.4

Table 2. Internal Capacitance Test

6. Conclusions

This work proves that ferroresonance can be evaluated in laboratory cases under controlled environments. In addition, it has been possible to determine the sort of tests that should be performed for an accurate representation of the transformer model. For future work an extensive benchmarking will be developed, comparing ferroresonance signals from simulation to experimental results.

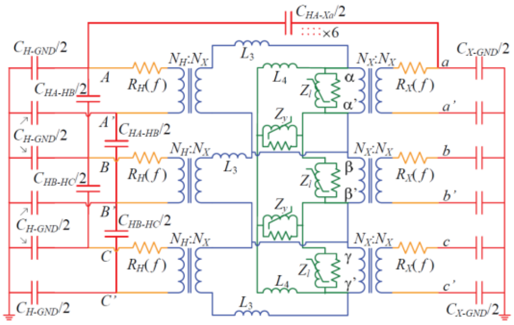

Fig.1. Duality derived equivalent circuit of a three phase transformer.

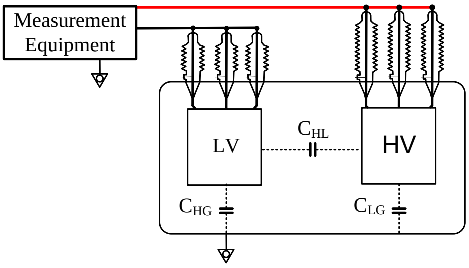

Fig.2. Internal capacitance test set up.

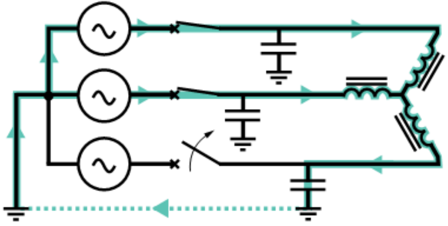

Fig.3. Ferroresonance test circuit.

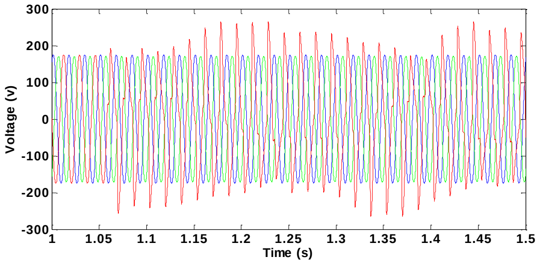

Fig.4. Ferroresonance signal for a 112. kVA transformer.

Acknowledgement

This work is being supported by the Spanish “Ministerio de Educación y Ciencia” under the Grant DPI2009-14713-C03-02.

References

[1] P. Moses and M. Masoum: "Impacts of Hysteresis and Magnetic Couplings on the Stability Domain of Ferroresonance in Asymmetric Three-phase Three-legged Transformers", *IEEE Trans. on Energy Conversion*, vol. 26, no. 2, (2011), pp. 581-592.

[2] B.A. Mork, F. Gonzalez, D. Ishchenko, D.L. Stuehm, and J. Mitra, “Hybrid transformer model for transient simulation-Part I: Development and parameters,” *IEEE Trans. on Power Delivery*, vol. 22, no. 1, pp. 248-255, January 2007.

[3] IEEE Standard "Test Code for Liquid-Immersed Distribution, Power, and Regulating Transformers," IEEE Std C57.12.90-2010 (Revision of IEEE Std C57.12.90-2006) , vol., no., pp.1,100, Oct. 15 2010.

[4] IEC International Standard "Power transformers - Part 1: General". IEC 60079-1. Ed. 3. 2011.

[5] F. de León, P. Gómez, J.A. Martinez-Velasco, and M. Rioual, “Transformers,” Chapter 4 of *Power System Transients. Parameter Determination*, J.A. Martinez-Velasco (ed.), CRC Press, 2009.

[6] P. Ferracci: Ferroresonance, *Cahier Technique no. 190*, Groupe Schneider, 1998.

[7] J.A. Corea-Araujo, F. Gonzalez-Molina, J.A. Martinez-Velasco, J.A. Barrado-Rodrigo, and L. Guasch-Pesquer, “An EMTP-based analysis of the switching shift angle effect during energization/de-energization in the final ferroresonance state,” *International Conference on Power Systems Transients (IPST)*, Vancouver, July 2013.

Efficiency Optimization of Cascaded Boost Converters Under Sliding Mode Control

R. Haroun, C. Olalla , A. El Aroudi, A. Cid-Pastor, R. Leyva and L. Martínez-Salamero
Departament d'Enginyeria Electrònica, Elèctrica i Automàtica,
Escola Tècnica Superior d'Enginyeria,
Universitat Rovira i Virgili

***Abstract*—The cascade connection of two boost-based loss free resistors (LFRs) can be a good candidate for impedance matching in PV systems with a low voltage DC (LVDC) bus of 380 V at the output. In this paper, it will be first shown that the efficiency of this cascaded boost system depends on the intermediate capacitor voltage level. This gives an extra degree of freedom to perform an online optimization of the losses in terms of this voltage level and to improve the efficiency of the two cascaded system. The theoretical results are verified by means of numerical simulations and experimental measurements.**

I. INTRODUCTION

As a main motivation, the typical problem in electrical power generation using PV systems is the relatively high required conversion ratio to obtain a bus-side output voltage of 380 V from a lower voltage that can be generated by a PV panel with its Maximum Power Point Tracking (MPPT). Usually, this PV panel can only provide a voltage between 22 V- 44 V. Cascaded step-up converters can be a good alternative in terms of efficiency, in order to obtain the desired output voltage. This paper presents the interconnection of two cascaded boost converters that are working as Loss-Free Resistor (LFR) in the sense that the current and the voltage at their input port are proportional [1]. The LFR behavior will be obtained by employing a sliding-mode control (SMC) [2] approach and presents several advantages: i) it greatly simplifies the dynamics of this nonlinear system ii) it guarantees robust stability for all the operation points of interest and iii) in addition, it provides an extra degree of freedom in the intermediate capacitor voltage that can be used for online efficiency optimization. These advantages will be described analytically and verified by means of numerical simulations and experimental results.

II. CASCADE CONNECTION OF TWO BOOST CONVERTERS BASED ON LOSS-FREE RESISTOR

Fig. 1 depicts a possible practical implementation of a relatively high conversion ratio cascaded step-up converter by means of two dc-dc boost switching regulators. This system has been studied in [3] and has been described with the ideal sliding dynamic model. The DC equilibrium point of the equivalent model are given by

$$x^* = [V_{c1}, V_{c2}]^\top = V_g[\sqrt{\frac{g_1}{g_2}}, \sqrt{Rg_1}]^\top. \tag{1}$$

The expression of this equilibrium point shows interesting properties. For this case, V_{c2} is considered constant. Therefore V_{c1} can be controlled using g_2 as a degree of freedom that can be used to regulate the intermediate voltage V_{c1} which can be used for online efficiency optimization of cascaded boost converters.

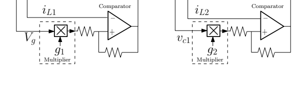

Fig. 1. Circuit diagram of the two cascaded boost converter with the proposed SMC.

TABLE I
EXPERIMENTAL REALIZATION OF THE PROPOSED CASCADED BOOST CONVERTER

Notation	Parameter	Value i=1	Value i=2
L_i	Inductance	300 μH	2 mH
C_i	Capacitance	100 μF	100 μF
R_{L_i}	DC Resistance of L_i	120 mΩ	40 mΩ
R_{on_i}	ON Resistance of Q_i	See Table II	180 mΩ
Tr_{on}	Q_i Turn-on Rise Time	20 ns	20 ns
Tr_{off}	Q_i Turn-off Fall Time	20 ns	20 ns
C_{ds_i}	Q_i Drain-Source Cap.	See Table II	60 pF
V_{D_i}	Q_{D_i} Diode Forward Voltage	0.85 V	2.3 V
$\frac{1}{T_{sw}}$	Switching Frequency	50 kHz	100 kHz

TABLE II
FET TRANSISTORS FOR DIFFERENT V_{ds} VOLTAGES

Parameter FET	FET #1	FET #2
V_{ds}	100 V	200 V
Name	TPH4R50ANH	IXFH50N20
R_{on_1}	3.7 mΩ	60 m Ω
C_{ds_1}	400 pF	200 pF

III. OPTIMAL EFFICIENCY OPERATION OF CASCADED BOOST CONVERTERS

The simplicity and control robustness of the proposed converter provides an interesting architecture for versatile high gain conversion. This section introduces the range of operation of the converter, presents an approximated power loss analysis using standard approaches [4] and discusses its optimal operation regarding efficiency.

The Intermediate voltage V_{c_1} is considered to be in the set $[50, 150]$ V, and its value will be discussed in the upcoming subsections. Power rating of the converter is assumed to be 180 W.

A. Power Loss Analysis

The power loss in the different components of the converter can be estimated by the following expressions:

$$\begin{aligned}
&\text{Inductor } L_i \text{ Losses:} && P_{L_i} = R_{L_i} I_{L_i}^2 \\
&\text{FET } Q_i \text{ Conduction Losses:} && P_{Q_{icd}} = R_{on_i} I_{L_i}^2 D_i \\
&\text{Diode } Q_{D_i} \text{ Conduction Losses:} && P_{D_{icd}} = V_{D_i} I_{L_i} (1 - D_i) \\
&\text{FET } Q_i \text{ Switching Losses:} && P_{Q_{isw}} = \tfrac{1}{2T_{sw}} (T_{on} + \dots \\
& && T_{off}) I_{L_i} V_{c_i} + \tfrac{1}{2T_{sw}} C_{ds_i} V_{c_i}^2 \\
&\text{Diode } D_i \text{ Switching Losses:} && P_{D_{isw}} = \tfrac{1}{T_{sw}} V_{c_i} Q_{rr_i}
\end{aligned} \tag{2}$$

where D_i are the steady-state duty-cycles and T_{sw} is the switching period, which can be considered constant during steady-state operation [5]. The diode switching losses can be defined as in [6], where $Q_{rr_i} = 1.30 \cdot 10^{-11} \cdot V_{ci}$ is the reverse recovery charge. The remaining parameters, such as R_{L_i}, R_{on_i}, V_{D_i}, $T_{r_{on}}$, $T_{r_{off}}$ and C_{ds_i} are defined in Table I and can be obtained from datasheets.

The analysis of each loss function reveals that all terms in (2) are semiconvex functions depending on the steady-state intermediate capacitor voltage value V_{c_1}, the input voltage V_g and the input power $P_{in} = V_g I_{L_1}$, with the exception of the term corresponding to the conduction losses of the first FET S_1, which presents a concave function.

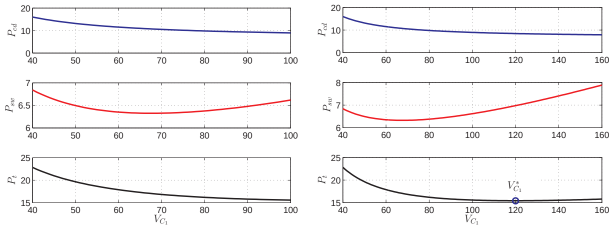

(a) FET 1 (b) FET 2

Fig. 2. Conduction losses P_{cd}, switching losses P_{sw} and total power losses P_t of the proposed architecture as function of the intermediate voltage V_{c1} for $P_{in} = 180$ W, $V_{bus} = 380$ V, $V_g = 12$ V and FET # 1 of Table II.

Convexity of the loss function results in the existence of an unique minimum point which is the global optimal that yields the highest efficiency. A sufficient condition for the convexity of the losses despite the concavity of $P_{Q_{1cd}}$ can be obtained by analysis of the second derivative of the following functions:

$$\begin{aligned} \frac{d^2 P_{Q_{1cd}}}{dV_{c_1}^2} &= -\frac{2R_{on_1} I_{L_1}^2 V_g}{V_{c_1}^3} \\ \frac{d^2 P_{Q_{2cd}}}{dV_{c_1}^2} &= \frac{6R_{on_2} I_{L_1}^2 V_g^2}{V_{c_1}^4} - \frac{2R_{on_2} I_{L_1}^2 V_g^2}{V_{c_2} V_{c_1}^3} \end{aligned} \tag{3}$$

The convexity of the loss function will be verified if $\frac{d^2 P_{Q_{1cd}}}{dV_{c_1}^2} + \frac{d^2 P_{Q_{2cd}}}{dV_{c_1}^2} > 0$. Note that this is a conservative condition because all other losses in the system are semiconvex functions but are not taken into account. Nevertheless, this condition results in the following inequality:

$$R_{on_2} > \frac{R_{on_1}}{V_g\left(\frac{3}{V_{c_1}} - \frac{1}{V_{c_2}}\right)}. \tag{4}$$

Given that the amount of current through Q_2 will be smaller than the current through Q_1 and that the difference in the drain-to-source voltages ($V_{c_1} \ll V_{c_2}$) requires switches with higher breakdown voltages in Q_2, the condition imposed in (4) can be easily satisfied in a practical design. As a consequence, the relationship between the losses and the intermediate voltage V_{c_1} can be guaranteed to have a convex characteristic. Fig. 2(a) depicts a plot of the power loss from the theoretical expressions in (2) for an input power of $P_{in} = 180$ W and an input voltage of $V_g = 12$ V. Since efficiency changes with V_{c_1}, P_o and V_g, the extra degree of freedom achieved with the sliding-mode control of the cascaded converter, g_2, can be used to achieve the optimal value of V_{c_1} that yields the best power efficiency. This possibility is discussed in the following subsections.

B. *Intermediate Voltage Influence in Efficiency*

One of the points that need discussion concerns the feasible range of operation of the intermediate voltage V_{c_1}. It can be observed in Fig. 2(a) that the optimal value of intermediate voltage $V_{c_1}^*$, which would yield the optimal efficiency, seems to have a value larger than 80 V. A zoomed out version of Fig. 2(a) is shown in Fig. 2(b), and illustrates that the optimal $V_{c_1}^*$ for that case is about 110 V. However, note that going beyond 80 V in the intermediate voltage requires a FET transistor S_1 allowing higher drain-to-source voltages, which would in turn change the properties of the semiconductor. Table II introduces two representative examples of FET transistors. The first one bears drain-to-source voltages up to 100 V, which with a 20 % safety margin results in an effective intermediate voltage of 80 V. The second FET in Table II has a higher V_{ds} voltage of 200 V which gives a maximum intermediate voltage of 160 V with the 20 % safety margin.

Figure 3(b) depicts the power efficiency for an input power of $P_{in} = 180$ W for the minimum and maximum input voltage with FET #2. As it can be observed, this device allows to achieve the optimal efficiency voltage $V_{c_1}^*$, which results in a peak efficiency of 95.5 % for V_g= 48 V. However, note that efficiency for low input voltage has a much lower value of approximately 85 %. Efficiency for the first considered device FET #1 has been plotted in Fig. 3(a). In this case, the optimal intermediate voltage can not be achieved due to the physical limits of the device, but the overall efficiency is better in this case, yielding 89.5 % and 95.5 % for the minimum and maximum input voltages, respectively.

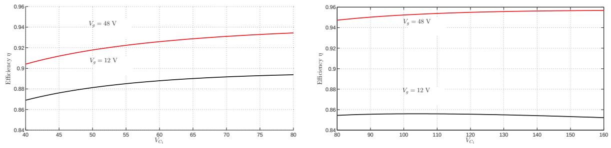

(a) FET 1 (b) FET 2

Fig. 3. Power efficiency $\eta = (P_{in} - P_t)/P_{in}$ for $P_{in} = 180$ W and $V_{bus} = 380$ V with 100 V breakdown voltage device FET #1.

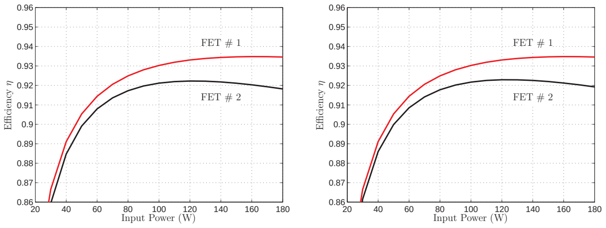

(a) Constant V_{c1} (b) Optimal V_{c1}

Fig. 4. Weighted Power efficiency for $V_{bus} = 380$ V with FET # 1 and FET # 2 and a constant intermediate voltage of $V_{c_1} = 80$ V and $V_{c_1} = 140$ V respectively.

Obviously, for similar dynamic characteristics, switches with higher breakdown voltages present higher conduction resistances. The effect of a high drain-to-source resistance increases with inductor current and duty-cycle, and results in much lower efficiency at low input voltages. It is obvious to conclude that, a versatile dc-dc converter requiring these large conversion ratios should consider the minimum input voltage operation as a possible worst case.

In order to compare both cases, a weighted efficiency plot is shown in Fig. 4. This weighted efficiency is a well-known way of evaluating the performance of power converters *bower* : 04 and, in this case, is the equally weighted sum of efficiencies at different operating conditions $V_{g_{min}}$=12 V, $V_{g_{nom}}$=30 V and $V_{g_{max}}$=48 V. In the figure, the intermediate voltage V_{c_1} is set to a constant value: the best admissible voltage of 80 V in FET #1 and the optimal value for nominal input voltage (140 V) for FET #2. It can be seen that the first FET achieves better overall efficiency, even if it can't reach the optimum intermediate voltage. The constant voltage in V_{c_1} can be achieved by regulation of the LFR surface, thanks to the degree of freedom available through g_2.

It is worth to remark that, given the convex characteristic of the surface, one could consider the use of a extremum seeking control strategy to achieve the optimal point. This makes sense in case FET # 2 is used, since the optimal voltage ranges between 100 and 160 V. However, the improvement that could be achieved is relatively small. Fig. 4(b) shows the best achievable weighted efficiency in case the intermediate voltage is adjusted to the optimal value. It can be observed that the achievable efficiency gain is very minor.

IV. CONCLUSION

This paper addresses the cascade connection of two dc-dc boost converters operating as loss-free resistors. Besides of simple realization, the proposed approach results in simple stable dynamics with the intermediate voltage being a free parameter. A loss analysis revealed that the efficiency is a concave function of this intermediate voltage and a simple strategy for online efficiency optimization has been proposed. Simulations have been used to verify the analysis. Although, the loss analysis proved that the efficacy is depending on the intermediate voltage, however we found that fixing the intermediate voltage using MOSFET with better performance will achieve the same improvement.

REFERENCES

[1] S. Singer, "Realization of loss-free resistive elements," *IEEE Transactions on Circuits and Systems*, vol. 37, no. 1, pp. 54–60, Jan. 1990. [Online]. Available: http://ieeexplore.ieee.org/lpdocs/epic03/wrapper.htm?arnumber=45691

[2] V. I. Utkin, *Sliding modes and their application in variable structure systems*. MIR Publishers, 1978.

[3] R. Haroun, A. Cid, A. El Aroudi, and L. Martinez-Salamero, "Synthesis of canonical elements for power processing in dc distribution systems using cascaded converters and sliding-mode control," *IEEE Transactions on Power Electronics,*, Early acsess 2013.

[4] R. Erickson and D. Maksimovic, *Fundamentals of power electronics*. Springer Science and Business Media Inc, 2001.

[5] A. Abrishamifar, A. Ahmad, and S. Elahian, "Fixed frequency sliding mode controller for the buck converter," in *2nd Power Electronics, Drive Systems and Technologies Conference (PEDSTC)*, Feb. 2011, pp. 557 – 561.

[6] S. Vighetti, J. P. Ferrieux, and Y. Lembeye, "Optimization and design of a cascaded DC/DC converter devoted to grid-connected photovoltaic systems," *IEEE Transactions on Power Electronics*, vol. 27, pp. 2018 – 2027, April 2012.

A Transformer-Less Dual-Stage Topology for Grid-Connected Microinverters

O. Lopez-Santos[1,2,4], L. Martinez-Salamero[3], G. Garcia[1,2], H. Valderrama-Blavi[3]
[1]CNRS, LAAS, F-31400 Touluse, France; [2]Univ de Toulouse, INSA, LAAS, F-31400 Toulouse, France
[3]Universitat Rovira i Virgili, 43007 Tarragona, Spain; [4]Univ de Ibagué, 7652000 Ibagué, Colombia
e-mail: olopez@laas.fr

Abstract

A transformer-less topology for a grid-connected photovoltaic micro-inverter is described in this paper. The proposed structure is a dual-stage topology with a quadratic boost converter in the DC-DC stage and a full-bridge inverter in the DC-AC stage. The quadratic boost uses a sliding-mode current controller without regulation of the output voltage whose reference in generated by a maximum power point tracker (MPPT). The full-bridge inverter injects real power to the grid by means of a sinusoidal reference sliding-mode tracking-loop whose amplitude is defined with the output power of the DC-DC stage.

1. Introduction

A great interest in the grid-connected inverters has arisen in recent years. These converters have prompted the development of dispersed-generation units based on photovoltaic (PV) modules among other renewable resources [1]-[2]. On the other hand, although there is some intermittency in the availability for the solar energy, the PV generators offer the possibility of covering an important part of the energy consumption in an interconnected system with dispersed installations of low, medium and high power levels. The grid-connected PV generators can operate without an energy storage unit reducing the complexity and periodicity of the maintenance procedures. As a consequence, these applications are gaining visibility focusing many research efforts in the development of the power conversion units.

The inverter technologies applied in grid-connected PV generation can be classified into three important main groups: a) centralized inverters; b) string and multi-string inverters; and, c) module-oriented inverters. The present trends are specially focused on the multi-string technology and the module oriented technology in medium and low power applications [3]-[4]. The aim of the PV module oriented technology is to install the system with a simple mechanical assembly and an easy connection to the grid, so that, this solution can replace to some extent the large photovoltaic installations through the concept of dispersed generation. The module oriented inverters can be classified into single-stage, dual-stage and multi-stage, considering the number of the power processing stages connected in cascade within the inverter.

A recent comparison identifies the dual-stage topologies with a DC-DC stage and a DC-AC stage as the most competitive solutions in module oriented converters [4]. However, a discussion is still open to determine the need of a transformer in the converter structure. This fact intensifies the work in the transformer-less topologies which lead to less complexity, higher efficiency and lower size, weight and cost [5]. Further, due to the fact that the power level can be achieved with no more than one or two solar modules, a higher gain in one of the two stages is required. Thus, to cover the gain requirement, our proposal involves a quadratic boost converter which proved to be a competitive DC-DC structure for module oriented application [6], allowing the use of the known full-bridge inverter in the DC-AC stage. To ensure stability, reliability with a simple implementation, a sliding mode approach is tacked to solve the control problems [7].

This extended abstract starts with a description of the overall system in section II followed by the description of the DC-DC and DC-AC stages in sections III and IV, respectively. Preliminary conclusions and future work is tackled.

2. Overall system description

As depicted in figure 1, the proposed micro-inverter is represented with a power block and a control block. The power block has a DC-DC converter and a DC-AC converter connected in cascade. The control block has a controller for each power stage and a MPPT. The control of the DC-DC stage must guarantee the extraction of the maximum power of the solar panel boosting the output voltage to a value between 15 and 30 times higher than the one of input voltage. The control of the DC-AC stage shapes a sinusoidal current waveform to inject real power to the grid. The MPPT must define the instantaneous input conductance for the DC-DC converter. The amplitude of the sinusoidal output current for the DC-AC stage is computed using the output power of the DC-DC stage.

The proposed micro-inverter has a quadratic boost converter in the DC-DC stage and a full-bridge inverter in the DC-AC stage. Both converters use the sliding-mode in order to follow time-varying references which are functions of grid parameters and available power.

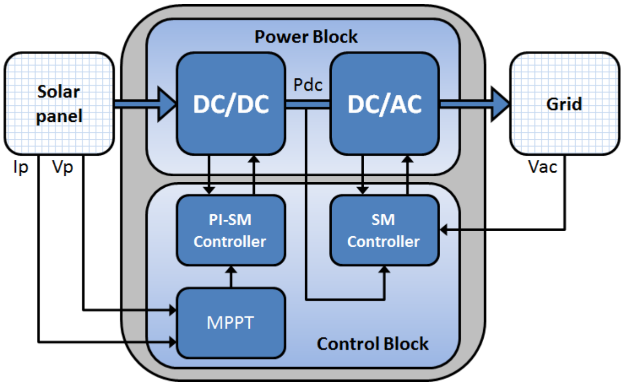

Fig. 1. Block diagram of a two-stage photovoltaic microinverter

3. DC-DC stage: Quadratic boost converter

The quadratic boost converter shown in figure 2 results of the generalized cascaded boost topologies with a single switch introduced in [8]. This converter allows to cover gain ranges not available with the single boost converter or the cubic boost converter essentially because of efficiency reasons [6].

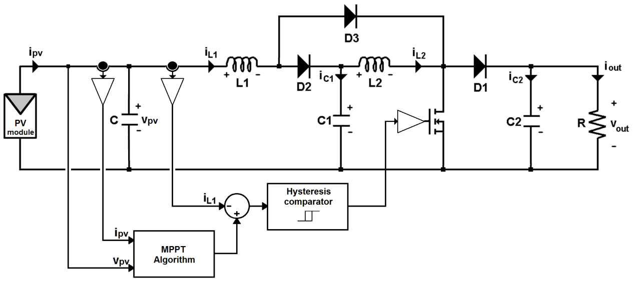

Fig. 2. Quadratic boost converter and control scheme

To control the DC-DC converter, a sliding surface based on the time-varying current reference $i_E(t)$ is proposed as follows:

$$S(x) = i_E(t) - i_{L_1} \tag{1}$$

where the value of $i_E(t)$ is given by the MPPT. The control law is implemented by using a hysteresis comparator.

4. DC-AC Stage: Full-bridge inverter

The full-bridge topology is proposed for the DC-AC stage. Converter is used as a voltage source inverter which is fed by the DC-DC stage. Although the unipolar technique is preferred in some stand-alone single-phase applications, the bipolar technique is proposed in order to avoid the common mode noise which is accentuated when the use of the unipolar technique. The sinusoidal shape in the current waveform is accomplished through a sliding-mode based control scheme which is implemented using a hysteresis comparator. The circuit diagram and its control scheme of the inverter are depicted in figure 3.

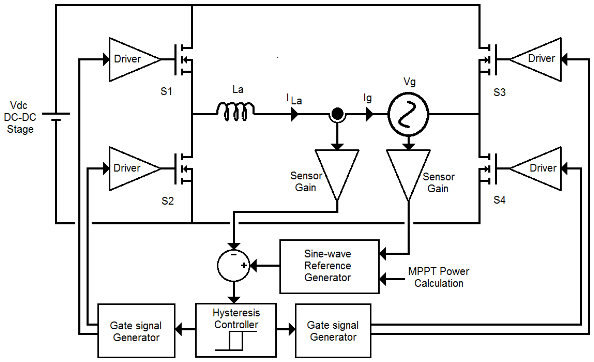

Fig. 3. Full-bridge inverter and control scheme

The sliding surface is defined forcing the inductor current to follow a current reference with the same frequency and phase of the grid voltage, obtaining the injection of real power. The following sliding surface is proposed:

$$S_1(x) = \frac{2P_{ref}V_g}{V_{g_{pk}}^2} - i_{La} \tag{2}$$

5. Preliminary conclusions and future work

A transformer-less dual-stage topology for a grid-connected micro-inverter has been proposed. The key aspect of this research work is to use a quadratic boost converter in the DC-DC stage ensuring stability and robustness of the overall system. The problem is tacked from a sliding-mode approach.

References

[1] F. Blaabjerg, Z. Chen, S.B. Kjaer, “Power electronics as efficient interface in dispersed power generation systems”. *IEEE Trans. on Power Electron.*, vol.19, no. 5. pp. 1184-1194, 2004.

[2] Y. Xue, L. Chang, S.B. Kjaer, J. Bordonau, T. Shimizu, “Topologies of single-phase inverters for small distributed power generators: an overview”, *IEEE Trans. on Power Electron.*, vol. 19, no. 5, pp. 1305-1314, 2004.

[3] Q. Li and P. Wolfs, “A Review of the Single Phase Photovoltaic Module Integrated Converter Topologies with Three Diferent DC Link Configurations”, *IEEE Trans. on Power Electron.*, vol. 3, no. 3, pp. 1320-1333, 2008.

[4] S. Baekhoej, J.K. Pedersen, F. Blaabjerg, “A Review of Single-Phase Grid-Connected Inverters for Photovoltaic Modules” *IEEE Trans. on Ind. Appl.*, vol. 41, no. 5, pp. 1292-1306, 2005.

[5] I. Patrao, E. Figueres, F. Gonzlez-Espín, G. Garcerá. “Transformerless topologies for grid-connected single-phase photovoltaic inverters”. *Energy for Sustainable Development*, vol. 16, pp. 3423-3431, 2011.

[6] O. Lopez-Santos, L. Martinez-Salamero, G. Garcia, H. Valderrama-Blavi, D. Mercury. “Efficiency analysis of a Sliding-mode Controlled Quadratic Boost Converter”. *IET Power Electron.*, 2013.

[7] V.I. Utkin, J. Guldner, J. Shi. Sliding Mode Control in Electro-Mechanical System, Ed. CRC Press, Tylor and Francis Group, 2nd Edition, 2009.

[8] M.G. Ortiz-Lopez, J. Leyva-Ramos, E.E. Carbajal-Gutierrez, J.A. Morales-Saldaña. “Modelling and analysis of switch-mode cascade converters with a single active switch”. *IET Power Electron.*, vol. 1, no. 4, pp.478-487, 2008.

Synthesis of a Sliding Loss-Free Resistor based on a Semi-bridgeless Boost Rectifier for Power Factor Correction Applications

A. Marcos-Pastor, A. Cid-Pastor, E. Vidal-Idiarte, L. Martínez-Salamero.

Departament d'Enginyeria Electrònica, Elèctrica i Automàtica. ETSE, Universitat Rovira i Virgili.
E-mail: { adria.marcos@urv.cat , enric.vidal@urv.cat, angel.cid@urv.cat, javier.calvente@urv.cat, luis.martinez@urv.cat}

Abstract

In this work a Loss-Free Resistor (LFR) based on a semi-bridgeless boost rectifier is synthesized using sliding mode control. Although different bridgeless topologies have been developed, the semi-bridgeless topology presents less common-mode noise and its practical implementation is more suitable. Sliding mode control is proposed to achieve LFR behaviour and, therefore, its application in power factor correction is possible.

1. Introduction

For the last twenty years many power DC-DC converters have been proposed and compared [1] for power factor correction applications. The most popular PFC today's used is the boost converter connected to the grid by a diode bridge rectifier, because of its main advantages: grounded transistor, simplicity and high efficiency. However, its main drawback is that the diode bridge is the responsible of the largest share of losses. The need for higher efficiencies from the PFC stage has led the circuit designers to develop possible lower loss alternatives which have been called bridgeless PFC topologies. In [2] a performance evaluation of bridgeless boost based PFC rectifiers is presented. Fig. 1. illustrates a modification of the basic bridgeless PFC boost rectifier by means of the addition of two slow recovery diodes (D_A, D_B) and a second inductor (L_2), resulting in two DC-DC boost circuits, one for each half-line cycle [3]. This topology has been named semi-bridgeless boost rectifier and it is a more suitable solution for practical implementation than the basic bridgeless topology in terms of sensing the input voltage and current variables. The aim of this work is to propose the sliding mode control [4] as an alternative to the PWM operation for the semi-bridgeless boost rectifier topology.

2. Semi-Bridgeless Boost Rectifier Analysis

The semi-bridgeless rectifier has less conduction losses because of the eliminated diode in the current path flow in comparison to the boost with a diode bridge.

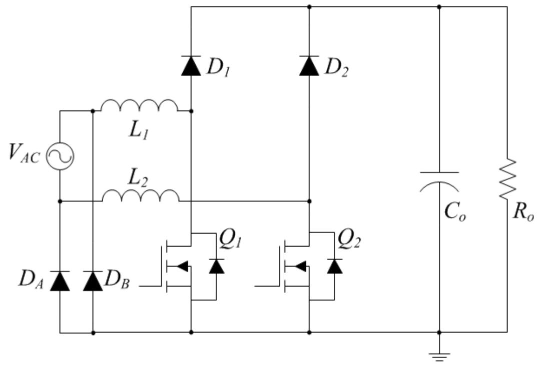

Fig.1. Semi-bridgeless PFC boost converter.

The semi-bridgeless rectifier is configured by two different boost converters that are meant to operate during each half-line cycle and, for that reason, the boost converters are controlled independently by the two control signals u_1 and u_2 respectively. Although the converter has got 3 elements to storage energy: L_1, L_2 and C_o, it has been considered that only 2 of them will do it during each half-line cycle: the output capacitor C_o and one of the inductors. So that, the state vector is

$$x(t) = \left[i_{Ln}(t) \quad v_{Co}(t) \right]^T$$

where n defines which of both inductors is operating each half-line cycle. Matrices A_{ON}, A_{OFF}, B_{ON} and B_{OFF} are the following if considering the operation of an ideal semi-bridgeless boost converter.

$$A_{ON} = \begin{bmatrix} 0 & 0 \\ 0 & -1/R_oC_o \end{bmatrix} \quad B_{ON} = \begin{bmatrix} 1/L_n \\ 0 \end{bmatrix} v_{in}$$

$$A_{OFF} = \begin{bmatrix} 0 & -1/L_n \\ 1/C_o & -1/R_oC_o \end{bmatrix} \quad B_{OFF} = \begin{bmatrix} 1/L_n \\ 0 \end{bmatrix} v_{in}$$

where v_{in} is the absolute value of the input voltage v_{AC}.

3. Synthesis of the Sliding Loss-Free Resistor

A LFR is a two-port switching structure whose input current is proportional to the input voltage and the input consumed power is transmitted to the output. Therefore the steady-state equations of a loss-free resistor can be presented as follows

$$V_1 = rI_1$$

$$V_1 I_1 = V_2 I_2$$

where V_1, I_1, V_2 and I_2 are the steady-state averaged value of input and output variables respectively. The parameter r is the resistive impedance that the circuit exhibits in steady-state. In the case of a DC-DC switching converter, the LFR is synthesized by applying the sliding mode control technique over the input current of the system. On the other hand, the sliding surface is the core of the sliding mode control and it will determine the behaviour of the controlled variable. Since our objective is to synthesize a LFR, the sliding surface $s(x)$ has to be chosen as depicted in Fig. 2.

$$s(x) = |i_{AC}| - g|v_{AC}|$$

That can be rewritten as follows in order to describe it in terms of the state vector $x(t)$

$$s(x) = i_{Ln} - gv_{in}$$

where $g = {}^{1}/_{r}$. The previous switching law results in a discontinuous control action that is the responsible of inducing a sliding regime on the switching surface theoretically at an infinite frequency.

The equivalent control can be obtained from the sliding surface and the equations that describe the dynamics of the system. As it could be expected, it is the same as the equivalent control traditional boost converter.

$$u_{eq} = 1 - \frac{v_{in}}{v_{Co}}$$

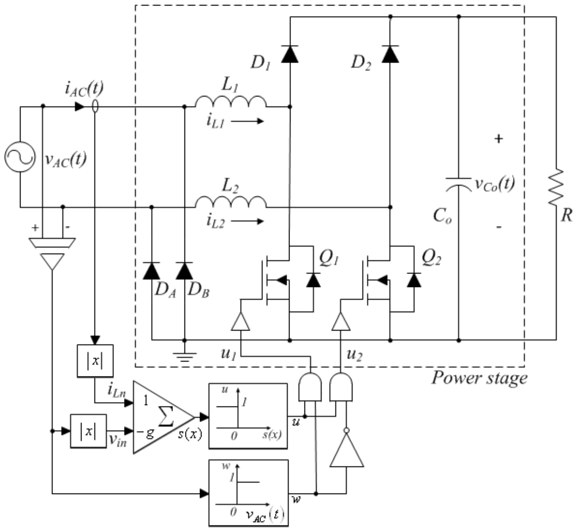

Fig.2. Block diagram of the sliding LFR based on a semi-bridgeless rectifier.

4. Application to Power Factor Correction

The synthesized SLFR is thought to operate as a preregulator for power factor correction connecting it to an AC voltage source. The preregulator has been simulated using PSIM with the following circuit parameters: $V_{AC} = 230\,Vrms$ and 50 Hz, $R_o = 176.4\,\Omega$, $L_1 = L_2 = 620\,\mu H$, $C_o = 300\,\mu F$ and $r = 52.9\,\Omega$. The steady state response of the variables in the equilibrium point is illustrated in Fig. 3.

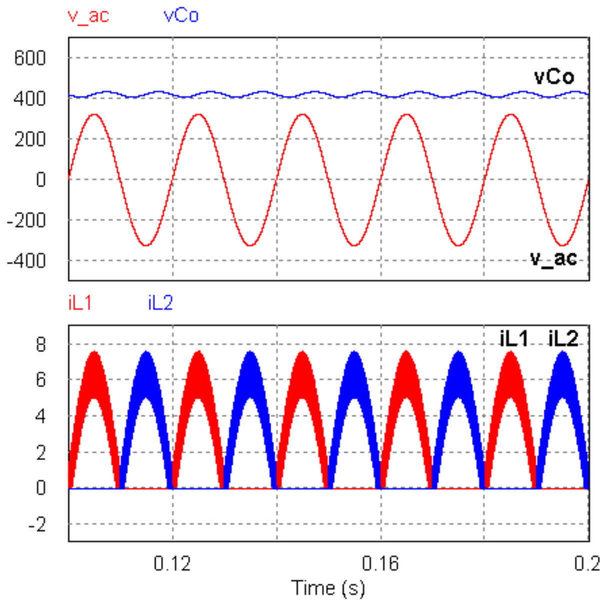

Fig. 3. Steady-state response of: a) line voltage $v_{AC}(t)$ and output capacitor voltage $v_{Co}(t)$, b) current through each inductor $i_{L1}(t)$ and $i_{L2}(t)$ of the SLFR-based preregulator.

5. Conclusions

In this work, a LFR based on a semi-bridgeless boost converter has been synthesized using sliding mode control. It has been proposed a unique sliding surface for both boost converters that configures the semi-bridgeless rectifier, achieving a correct LFR behaviour. The resulting SLFR has been applied to operate as a preregulator for power factor correction. Simulation results are in good agreement with the expected theoretical predictions. We are currently working towards experimental results from a real implementation.

References

[1] M. Matsuo, K. Matsui, L. Yamamoto, and F. Ueda, "A comparison of various DC-DC converters and their application to power factor correction," in Industrial Electronics Society, 2000. IECON 2000. 26th Annual Conference of the IEEE, 2000, pp. 1007-1013 vol.2.

[2] L. Huber, J. Yungtaek, and M. M. Jovanovic, "Performance Evaluation of Bridgeless PFC Boost Rectifiers," Power Electronics, IEEE Transactions on, vol. 23, pp. 1381-1390, 2008.

[3] A. F. de Souza and I. Barbi, "High power factor rectifier with reduced conduction and commutation losses," in Telecommunication Energy Conference, 1999. INTELEC '99. The 21st International, 1999, p. 5 pp.

[4] V. Utkin, Sliding modes and their application in variable structure systems: Mir Publishers, 1978.

Energy Management DC System Based on Current-Controlled Buck-Boost Modules

Harrynson Ramírez-Murillo*, Carlos Restrepo,Javier Calvente,Alfonso Romero,and Roberto Giral.

***Abstract*—The guidelines of a series hybrid fuel cell system that includes the control and protection loops are presented. The hybrid system is formed by a Fuel Cell, an Auxiliary Storage Device (ASD), and current-controlled dc-dc converters to make an energy management between FC and ASD in a series topology. The main advantages of the selected converter is its voltage step up and step down properties, high efficiency, and its low input as well as output current ripple that allows it to be positioned in the different fuel cell hybrid system localizations with a suitable design of its control. Therefore, to have the same module for all the system converters simplifies the design and construction tasks. The theoretical analyses have been validated by means of simulations and experimentally on 48 V, 1500 W purpose-built dc bus.**

I. INTRODUCTION

Nowadays, centralized generation coexists with a new tendency, which is given by environmental considerations and topological flexibility. This new model is known as distributed generation (DG) and it is characterized by a small generation size. The generating equipment is usually renewable or, at least, it presents similar characteristics and are efficient and environmentally friendly systems [1], [2]. For these reasons, Fuel Cell (FC) systems are good candidates to supply electrical power in DG systems [3], residential environments [4], electric vehicles [5] and dc bus applications [6].

It is well-known that the FC dynamics is considered slow due to its fully integrated mechanical devices, mainly the compressor, that ensure its safe, reliable and efficient operation under different operating conditions. As a consequence of this limitations a load transient could cause a high voltage drop after a short time, which is a symptom of the oxygen starvation phenomena and it is harmful for the FC [7]. The prevention of this undesired phenomenon requires the limitation of the slew-rate of the FC current. In addition, to ensure a fast response to any load power transient, batteries, ultracapacitors or other auxiliary power sources in conjunction with current-controlled dc-dc converters are needed to support the operation of the fuel cell, which is know as a FC hybrid system. In this paper a series hybrid topology is presented whose key element is an innovative non-inverting buck-boost dc-dc switching converter introduced in [8], with the current control proposed in [9], [10] to be a modular converter in the implemented hybrid system. The modular advantages such as voltage step up and step down properties, high efficiency, wide bandwidth, low input as well as output current ripple. Due to all the above mentioned features, this converter can be positioned in different localizations in the fuel cell hybrid system with a suitable design of its control.

II. FUEL CELL SYSTEM

The control loops and protection specifications of the FC series hybrid topology shown in Fig. 1 are listed in Table I. As mentioned above, this configuration uses the same converter module with input and output current regulations in the different places of Fig. 1. The high side current sensors in this module allows the connection in parallel of more modules (see converters 2 and 3 of Fig. 1). The digital master control sends the current references to the analogic current loops to regulate the different voltage values of the system. The master control goals are: FC slew-rate current limitation, FC and capacitor range voltage protection, output voltage v_o regulation at 48 V, maximum current limitation in each converter, safe startup and shutdown of the system, among others.

Two different converter models were developed to study the FC series hybrid topology. The first one is a static model to make long-time simulations of the system while the second one is a dynamic model to study the short-time transitions.

TABLE I
FC SERIES HYBRID SYSTEM SPECIFICATIONS.

Parameter	Value	Units	Description
V_{FCmin}	25	V	FC minimum voltage
V_{FCmax}	48	V	FC maximum voltage
V_{oref}	48	V	Output voltage reference
V_{ASDref}	50	V	ASD voltage reference
V_{ASDmin}	25	V	ASD minimum voltage
V_{ASDmax}	57	V	ASD maximum voltage
SR_{FCd}	32	A/S	FC slew-rate down current
SR_{FCu}	8	A/S	FC slew-rate up current
$P_{o\max}$	1500	W	Output maximum peak power
$P_{FC\max}$	500	W	FC maximum power
C_o	2350	μF	Dc bus capacitor
C_{ASD}	600	mF	ASD capacitor
$I_{\max}$	16	A	Converters maximum current value

A high frequency pole in the v_o control loop was implemented with an analog circuit to reduce the computational

---

This work was supported by the Spanish Ministerio de Ciencia e Inovación under the projects CSD2009-00046 and TEC2009-13172.

H. Ramírez-Murillo, C. Restrepo, J. Calvente, A. Romero and R. Giral are with the Departament d'Enginyeria Electrònica, Elèctrica i Automàtica, Escola Tècnica Superior d'Enginyeria, Universitat Rovira i Virgili, 43007 Tarragona, Spain.

*Corresponding author. Email: harrynson.ramirez@urv.cat. Postal Address: Avda. Països Catalans 26, Campus Sescelades, 43007, Tarragona, Spain. Fax: (+34)977559605. Telephone number: (+34)977297051.

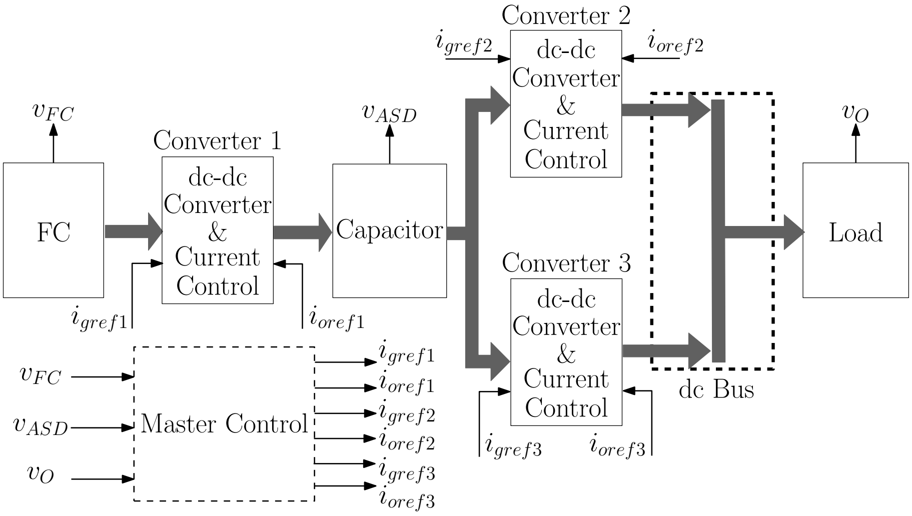

Fig. 1. FC series hybrid topology block diagram. The master control regulates the input/output port voltages from each converter by means of the current reference values

costs and the time-delays of the digital master control. This pole works as an anti-aliasing low-pass filter because the converter modules are not synchronized switching frequencies.

III. EXPERIMENTAL RESULTS

Fig.2 shows a resistance load variation from 22.6 Ω to 7.2 Ω, with a frequency of 100 Hz, while V_{ASD} is equal to 50 V. The dc bus impedance has been designed to be less than 30 mΩ and the output voltage error was 0.32 % respect to 48 V dc bus reference. Therefore, the dc output voltage is well regulated and the transient deviations are within the desired boundaries.

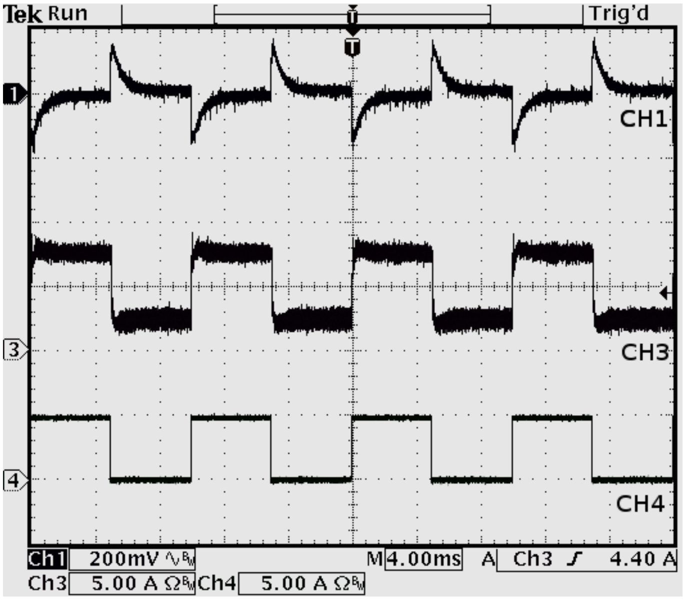

Fig. 2. Experimental measurement of the dc bus voltage during a pulsating load power profile with a V_{ASD} = 50 V. CH1: dynamic response of the DC bus voltage v_o (200 mV/div, AC coupling), CH3: input current of the converters 2 and 3 (5 A/div), CH4: load current variations (5 A/div) and time base of 4 ms.

IV. FUTURE WORKS

A complete mathematical description in conjunction with experimental and simulation results will be carried out to test the FC series hybrid system. Next experiments will be: startup and shutdown of the FC series hybrid system, load variations between 10 to 90 % for different battery levels, large and small signal transients, and capacitor charge and discharge.

REFERENCES

[1] H. Liang, B. J. Choi, W. Zhuang, and X. Shen, “Stability enhancement of decentralized inverter control through wireless communications in microgrids,” *Smart Grid, IEEE Transactions on*, vol. 4, no. 1, pp. 321–331, 2013.

[2] K. Rajashekara, “Hybrid fuel-cell strategies for clean power generation,” *Industry Applications, IEEE Transactions on*, vol. 41, no. 3, pp. 682–689, 2005.

[3] A. Ghazanfari, M. Hamzeh, H. Mokhtari, and H. Karimi, “Active power management of multihybrid fuel cell/supercapacitor power conversion system in a medium voltage microgrid,” *Smart Grid, IEEE Transactions on*, vol. 3, no. 4, pp. 1903–1910, 2012.

[4] Y. Taniguchi, Y. Fujimoto, and Y. Hayashi, “Determination of optimal operation plans of fuel cell system in residential house with pv system,” in *Power and Energy (PECon), 2012 IEEE International Conference on*, 2012, pp. 110–115.

[5] M. Zandi, A. Payman, J.-P. Martin, S. Pierfederici, B. Davat, and F. Meibody-Tabar, “Energy management of a fuel cell/supercapacitor/battery power source for electric vehicular applications,” *Vehicular Technology, IEEE Transactions on*, vol. 60, no. 2, pp. 433–443, 2011.

[6] X. Li, W. Zhang, H. Li, R. Xie, and D. Xu, “Design and control of bi-directional dc/dc converter for 30kw fuel cell power system,” in *Power Electronics and ECCE Asia (ICPE ECCE), 2011 IEEE 8th International Conference on*, 2011, pp. 1024–1030.

[7] J. Pukrushpan, A. Stefanopoulou, and H. Peng, “Control of fuel cell breathing,” *IEEE Control Syst. Mag.*, vol. 24, no. 2, pp. 30 – 46, apr 2004.

[8] C. Restrepo, J. Calvente, A. Cid-Pastor, A. Aroudi, and R. Giral, “A noninverting buck-boost dc-dc switching converter with high efficiency and wide bandwidth,” *Power Electronics, IEEE Transactions on*, vol. 26, no. 9, pp. 2490–2503, Sept. 2011.

[9] C. Restrepo, J. Calvente, A. Romero, E. Vidal-Idiarte, and R. Giral, “Current-mode control of a coupled-inductor buck-boost dc-dc switching converter,” *Power Electronics, IEEE Transactions on*, vol. 27, no. 5, pp. 2536–2549, May 2012.

[10] C. Restrepo, T. Konjedic, J. Calvente, M. Milanovic, and R. Giral, “Fast transitions between current control loops of the coupled-inductor buck-boost dc-dc switching converter,” *Power Electronics, IEEE Transactions on*, vol. 28, no. 8, pp. 3648–3652, 2013.

Using the Characteristic Hessian in Extremum Seeking Control for PV Generator

Hector Zazo and Ramon Leyva

Department of Electronic, Electrical and Automatic Control Engineering
University Rovira i Virgili
Av. Paisos Catalans, 43007 Tarragona (Spain)
Phone/Fax number:+0034 977557049/9605, e-mail: hector.zazo@urv.cat

Abstract

The paper analyzes the use of the second derivative or hessian of the panel characteristic in order to improve MPPT performances. Extremum Seeking Control (ESC) methods add a dithering signal to drive the system to its maximum. We estimate the hessian term using the square of the dithering signal and use it to improve the gain ranges and transient behavior against irradiance and temperature changes. Finally, we compare the performances of a proposed Hessian ESC algorithm with a typical ESC by means of PSIM simulations and corroborates that the Hessian one performs better.

1. Introduction

Maximum Power Point Tracking (MPPT) algorithms are typical used in PV panels to increase the extracted power. There are several approach to design the MPPT circuit, for instance: el Perturb & Observe, Fuzzy Control techniques, Neural Networks, Extremum Seeking Control (ESC); among others. MPPT based on ESC have good performances and are easy to analyze dynamically [1]. We show the block diagram of a typical ESC in figure 1.

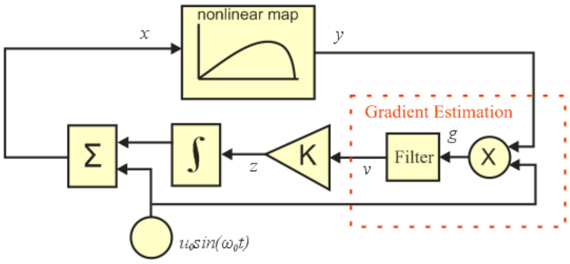

Fig. 1. ESC schema

Typical ESC allows us to find the maximum of a function with the only assumption that it is concave. Given that the PV panel characteristic is concave, we can use this technique for MPPT purposes. Loop gain in ESC method depends on curvature [2]; that is, the Hessian value at each operating point. We propose to use the Hessian information to make the loop gain independent of the curvature and, in this way, choose a proper value of the gain loop. This is of maximal interested at the right-side of the maximum when the curvature takes values in a broad range. On the contrary, curvature is very small at the left-side of the maximum in a PV panel characteristic.

We use approach proposed by Moase et al. [3] called Newton-Like Extremum Seeking Control (NL-ESC) so that the approximation rate does not depend on the characteristic curvature, thus overcoming drawbacks caused by the fact of having a loop gain with a too big range whose value depends on the operating point during transients.

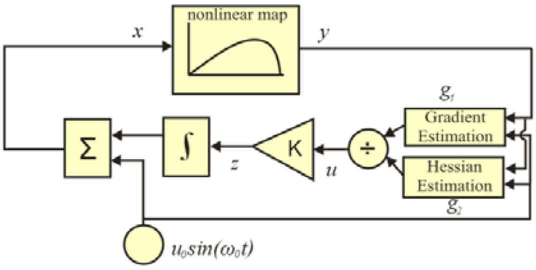

Fig. 2. NL-ESC schema

Block diagram of NL-ESC algorithm is shown in figure 2. The block includes the Hessian estimation as well as the gradient estimation. In the paper, we propose a Hessian estimation that differs from the one proposed in [3] and use the square of the dithering signal. The Hessian estimation is explained in section 2. Section 3 compares approaches of diagram block of figures 1 and 2 by means of PSIM simulation. Last section summarizes and concludes the paper.

2. Hessian Estimation Principle

Given a non-linear panel characteristic,

$$y = f(x) \tag{1}$$

where y is the output power and x represents the generator input. Considering that the input x consists of a slow signal u and a sinusoidal dithering of small amplitude u_0 and angular frequency ω_0; that is,

$$x = u + u_0 \sin(\omega_0 t) \tag{2}$$

then the output power expression corresponds to,

$$y = f(u + u_0 \sin(\omega_0 t)) \tag{3}$$

The power expression can be approximated by the first terms of Taylor series,

$$y \approx f(u) + \frac{df(u)}{du} u_0 \sin(\omega_0 t) + \frac{1}{2}\frac{d^2 f(u)}{du^2} u_0^{\,2} \sin^2(\omega_0 t) \tag{4}$$

That, in turn, it can be rewritten as,

$$y \approx f(u) + \frac{df(u)}{du} u_0 \sin(\omega_0 t) + \frac{1}{4}\frac{d^2 f(u)}{du^2} u_0^{\,2} - \frac{1}{4}\frac{d^2 f(u)}{du^2} u_0^{\,2} \cos(2\omega_0 t) \tag{5}$$

The information about the curvature or Hessian of the panel characteristic is associated to the second harmonic from expression (5). Then, in order to extract that information, we apply a high-pass filter to output power y; that is,

$$y_f \approx \frac{df(u)}{du} u_0 \sin(\omega_0 t) - \frac{1}{4}\frac{d^2 f(u)}{du^2} u_0^{\,2} \cos(2\omega_0 t) \tag{6}$$

and multiplying the filtered output y_f by $u_0^{\,2} \cos^2(\omega_0 t)$, we obtain,

$$\begin{aligned} g_2 \approx{}& \frac{1}{2}\frac{df(u)}{du} u_0^{\,3} \sin(\omega_0 t) + \frac{1}{4}\frac{df(u)}{du} u_0^{\,3} \sin(3\omega_0 t) \\ &- \frac{1}{4}\frac{df(u)}{du} u_0^{\,3} \sin(\omega_0 t) - \frac{1}{8}\frac{df^2(u)}{du^2} u_0^{\,4} \cos(2\omega_0 t) \\ &- \frac{1}{16}\frac{df^2(u)}{du^2} u_0^{\,4} - \frac{1}{16}\frac{df^2(u)}{du^2} u_0^{\,4} \cos(4\omega_0 t) \end{aligned} \tag{7}$$

It can be observed from expression (7) that the Hessian information in signal g_2 is associated to continuous component. Consequently, we apply a low-pass filter and obtain the estimation of the Hessian

$$p \approx -\frac{1}{16}\frac{df^2(u)}{du^2} u_0^{\,4} \tag{8}$$

Figure 4 shows the Hessian estimation schema that is used to implement the MPPT based on NL-ESC method, where the high-pass filter, low-pass filter, multiplier element and the implementation of the term $u_0^{\,2} \cos^2(\omega_0 t)$ can be observed.

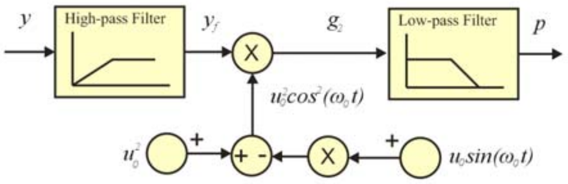

Fig. 3. Hessian estimation schema

3. Simulation results

Diagram blocks of figure 1 and the one of figure 2 beside the detail of figure 3 have been implemented in PSIM We compare booth approaches against small irradiances changes. Waveforms of the comparison are shown in figure 4, where NL-ESC behavior is depicted in the bottom and typical ESC one in the top plot. It can be appreciated that the transient behavior is better in the NL-ESC since it is faster and exhibits a lower overshoot.

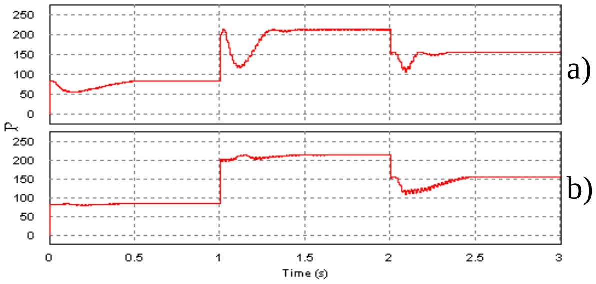

Fig. 4. Transient of panel power in front a slow irradiance change. a) ESC case. b) NL-ESC case.

Also, we have simulated the transient behavior against an large and abrupt changes of irradiances. These waveforms are depicted in figure 5. It can be appreciated that the NL-ESC behaves as expected. On the contrary, typical ESC MPPT destabilizes due to a large gain transient drives the operating point beyond the open circuit voltage (v_{oc}).

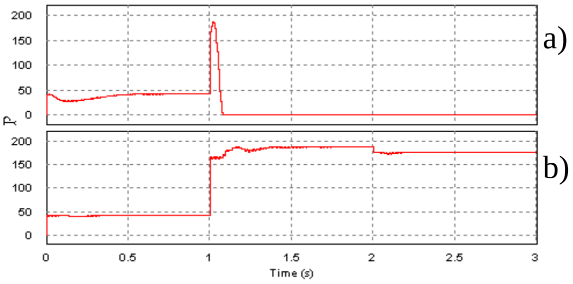

Fig. 5. Transient of panel power in front an abrupt irradiance change. a) ESC case. b) NL-ESC case.

4. Conclusions

The paper reviews the technique named Newton-like Extremum Seeking Control and adapts it as MPPT circuit for photovoltaic systems. NL-ESC performs better since loop gain do not depends on the curvature. We have corroborated the expected of NL-ESC and typical ESC behaviors by means of PSIM simulations.

References

[1] Leyva, R.; Alonso, C.; Queinnec, I.; Cid-Pastor, A.; Lagrange, D.; Martinez-Salamero, L.; "MPPT of photovoltaic systems using extremum - seeking control" Aerospace and Electronic Systems, vol.42, no.1, pp. 249- 258, Jan. 2006

[2] Leyva, R.; Artillan, P.; Cabal, C.; Estibals, B.; Alonso, C.; "Dynamic performance of maximum power point tracking circuits using sinusoidal extremum seeking control for photovoltaic generation" International Journal of Electronics, vol.98,nº 4, pp. 529- 542, 2011

[3] Moase, W.H.; Manzie, C.; Brear, M.J.; "Newton-Like Extremum-Seeking for the Control of Thermoacoustic Instability", Automatic Control, vol. 55, pp.2094-2105, Sept. 2010

INFORMATION CONTACT

Administrative contact:

Dr. Josep Ferré Borrull:
Email: josep.ferre@urv.cat
Phone: 34+ 977 559 632 , **Fax:** 34+ 977 559 605

Programme chairman:

Dr. Roberto Giral Castillón
Email: roberto.giral@urv.cat
Phone: 34+ 977 559 620 , **Fax:** 34+ 977 559 605

Informatic support:

Jordi Maré Viles
Email: jordi.mare@urv.cat
Phone: 34+977 559 712 , **Fax:** 34+977 558 501

Administrative support:

Angels Hernando Casado
Email: angels.hernando@urv.cat
Phone: 34+ 977 559 610 , **Fax:** 34+ 977 559 605

Dolores Córdoba Sánchez
Email: dolores.cordoba@urv.cat
Phone: 34+ 977 559 728 , **Fax**: 34+ 977 559 605

Franzina Borràs Martorell
Email: francina.borras@urv.cat
Phone: 34+ 977 559 726 , **Fax**: 34+ 977 559 605